ME 33 – NO. 1 JANUARY 1993 BIMONTHLY ISSN: 0304 – 3894

OURNAL OF AZARDOUS MATERIALS

SEVIER

JOURNAL OF HAZARDOUS MATERIALS

Management — Handling — Disposal — Risk Assessment

Review papers, normal papers, project reports and short communications are published dealing with all aspects of hazardous materials arising from their inherent chemical or physical properties. The scope of the journal is wide, ranging from basic aspects of preparation and handling to risk assessment and the presentation of case histories of incidents involving real hazards to employees or the public.

The following list, though not exhaustive, gives a general outline of the scope:

Properties: toxicity, corrosiveness, flammability, explosiveness, radioactivity, information data banks, dose–response relationships

Safety and health hazards: manufacturing, processing, transport, storage, disposal, major hazards and hazardous installations

Legislation: international, national and local codes of practice, threshold values, standards

Incidents: prevention, control, clean-up, communication, labelling, sources of information and assistance, case histories

Assessment: economic and general risk assessment, insurance, test methods, technical aspects of risk assessment of industrial hazards, reliability and consequence modelling, decision-making in risk management

11th Annual Presentation **93**

International™

America's premiere trade fair presenting the latest in worldwide environmental technology. Over 650 companies exhibiting more than 120 product categories.

15,000 attendees expected– including delegations from over 17 countries.

The only environmental trade fair participant in the U.S. Department of Commerce's 1993 Foreign Buyer Program.

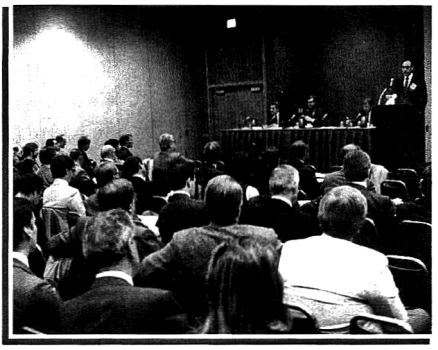

On-site International Business Center provides market data base and match-up services, market information, export/import assistance, interpreters, meeting arrangements and business services.

HAZMAT WORLD magazine

CONTROL AMBIENTAL magazine

Foreign Buyer Program

Tower Conference Management Company
800 Roosevelt Rd., Bldg. E-408, Glen Ellyn, IL 60137-5835 USA

☐ Please send complete details on ATTENDING HazMat/International '93

Name _____

Title _____

Company _____

Address _____

City _____

State/Country _____ Postal Code _____

Phone _____ FAX _____

A D

Tower Conference Management Co.
800 Roosevelt Road
Bldg. E - Suite 408
Glen Ellyn, IL 60137-5835
(708) 469-3373
FAX: (708) 469-7477

Announcement from the Publisher

Journal of Hazardous Materials prefers the submission of electronic manuscripts on computer disk.

The preferred storage medium is a 5¼ or 3½ inch disk in MS-DOS format, although other systems are welcome, e.g. Macintosh.

After **final acceptance**, your disk plus one final, printed and exactly matching version (as a printout) should be submitted together to the editor. **It is important that the file on disk and the printout are identical**. Both will then be forwarded by the editor to Elsevier.

Illustrations should be provided in the usual manner.

Please follow the general instructions on style/arrangement and, in particular, the reference style of this journal as given in 'Instructions to Authors'.

Please label the disk with your name, the software & hardware used and the name of the file to be processed.

Contact the Publisher for further information:

Desk Editorial Office
Journal of Hazardous Materials
P.O. Box 330
1000 AH Amsterdam, The Netherlands
Phone: (+31-20) 5862 758 Fax: (+31-20) 5862 459

ELSEVIER SCIENCE PUBLISHERS

JOURNAL OF HAZARDOUS MATERIALS

VOL. 33 (1993)

JOURNAL OF HAZARDOUS MATERIALS

VOL. 33 (1993)

ELSEVIER, AMSTERDAM – LONDON – NEW YORK – TOKYO

Abstracted/indexed in:
Applied Science and Technology Abstracts
ASM International/The Institute of Metals — Materials Information
Cambridge Scientific Abstracts
Centre de Documentation Scientifique et Technique — PASCAL database
Chemical Abstracts
CIS Documentation
Coal Abstracts
Current Awareness in Biological Sciences (CABS)
Current Contents (Engineering, Technology & Applied Sciences)
Engineering Index Abstracts
Environmental Periodicals Bibliography
Laboratory Hazards Bulletin/Chemical Hazards in Industry
NIOSHTIC
Système de Documentation et Information Métallurgique

 0304-3894/93/$06.00

This issue is printed on acid-free paper.

PRINTED IN THE NETHERLANDS

Publisher's Note

Compuscripts

Most authors of scientific articles nowadays use word processors to prepare their manuscripts. This implies that they are able to submit their articles on floppy disk, thereby allowing the text of the article to be fed directly into the typesetting computer. The advantages of this are clear: no typographical errors will be introduced into the text during the typesetting phase, and publication of the article can be faster than is normally the case. Elsevier is therefore providing authors with the opportunity to submit their papers to the *Journal of Hazardous Materials* on floppy disk. In order to distinguish between the traditional manuscript form and papers submitted on floppy disk, the latter hereafter be referred to as "compuscripts".

Announcement from the Publisher

Journal of Hazardous Materials prefers the submission of electronic manuscripts on computer disk.

The preferred storage medium is a 5¼ or 3½ inch disk in MS-DOS format, although other systems are welcome, e.g. Macintosh.

After **final acceptance**, your disk plus one final, printed and exactly matching version (as a printout) should be submitted together to the editor. **It is important that the file on disk and the printout are identical**. Both will then be forwarded by the editor to Elsevier.

Illustrations should be provided in the usual manner.

Please follow the general instructions on style/arrangement and, in particular, the reference style of this journal as given in 'Instructions to Authors'.

Please label the disk with your name, the software & hardware used and the name of the file to be processed.

Contact the Publisher for further information:

Desk Editorial Office
Journal of Hazardous Materials
P.O. Box 330
1000 AH Amsterdam, The Netherlands
Phone: (+31-20) 5862 758 Fax: (+31-20) 5862 459

ELSEVIER SCIENCE PUBLISHERS

Journal of Hazardous Materials, 33 (1993) 1–33
Elsevier Science Publishers B.V., Amsterdam

A guide to the evaluation of condensed phase explosions

P.A. Davies

Four Elements Ltd., Greencoat House, Francis Street, London SW1P 1DH (UK)

(Received March 9, 1992; accepted June 5, 1992)

Abstract

Condensed phase explosives present a hazard to both property and people. This hazard, which primarily manifests as overpressure, fragment generation and/or thermal radiation, can be realised through accidental initiation during manufacture, storage, handling and transport. Much work has been conducted to understand and quantify the effects of hazard realisation on property and people. This paper reviews available literature, describes a number of models, details damage criteria and provides an overview of condensed phase explosion effects on property and people.

1. Introduction

Damage caused to both property and people, as a result of explosion, often requires detailed evaluation so that action can be taken to reduce consequences, measures can be enacted to limit the likelihood of explosion and credible risk assessments can be performed. The following chapters describe explosion consequences and illustrate how certain effects can be quantified.

Since the beginning of the 1950's the majority of work in condensed phase (CP) explosion theory and effects has concentrated on nuclear explosions. However, the damage caused by nuclear explosions is not easily extrapolated to the damage associated with CP explosions. This is because explosions are essentially yield related. Consequently, thermal and pressure impulses differ between nuclear and CP explosions, and hence each type of explosion produces different degrees of damage. As a consequence of this it is difficult to compare nuclear explosions, having typical yields of 100,000 tonnes or more, with low yield CP explosions of interest in the manufacture, transport and storage of condensed phase explosives. In addition, data from nuclear explosions include the effects of ionising radiation together with other nuclear peculiarities, such as, thermo-nuclear pulse. As an example of their differences consider the case

Correspondence to: Dr. P.A. Davies, Four Elements Ltd., Greencoat House, Francis Street, London SW1P 1DH (UK). Current address: Europa House, 310 Europa Blvd., Westbrook, Warrington, WA5 5YQ (UK).

0304-3894/93/$06.00

of nuclear and conventional fireballs. The black body temperatures of nuclear initiated fireballs are orders of magnitude greater than their CP counterparts. Radiation temperatures for nuclear explosions approximate to 10^7 K, which is over 2000 times that of many high explosive and propellant explosions [1]. Similarly, nuclear weapons emit energy in the range 0.01 nm to 10 nm compared with 200 nm to 500 nm for conventional explosives.

In conclusion, there are no simple scaling laws which can be used to relate CP and nuclear explosions, or simple means of isolating ionising effects etc., so that data can be readily extrapolated. Consequently, the following chapters, where possible, only refer to CP explosions. This is because the inclusion of nuclear data may lead to erroneous assumptions and conclusions being made on the effects of relatively low yield chemical explosions.

2. Blast damage and injury

The term blast wave is used here to mean the shock wave caused by an explosion and should not be confused with the detonation wave. Upon detonation a detonation shock front travels away from the charge causing the temperature of the surrounding air to rise [1]. This initial shock front is known as the detonation wave. After a short distance of travel the detonation wave is overtaken by a new shock front which leaves a zone of rarefied air immediately behind it. This new shock front is known as the blast wave and although its peak pressure and initial velocity is lower than that of the detonation wave it decays much more gradually and therefore exerts its force over a greater distance [1]. The blast wave from all chemical explosions has a definite and measurable pattern. Upon detonation a sudden and violent release of energy causes the surrounding air pressure to rise rapidly creating a region of positive pressure known as "overpressure". As the blast wave moves away from its source at high velocity (supersonic) the overpressure increases sharply to a peak value, known as the peak overpressure, and then gradually recedes. The overpressure phase is followed by a region of negative pressure or "underpressure". This pressure is generally insignificant compared with the overpressure phase, although such negative pressure can cause moderate damage especially at close distances from the charge.

The characteristics of blast waves are discussed by Lees [2] and detailed accounts are given by Kinney [3] and Baker et al. [1]. It is sufficient here to simply identify a means by which blast wave characteristics, in particular overpressure, can be estimated so that their effects on buildings and people can be quantified.

Damage and injury as a result of explosion is largely a consequence of two loading effects, known as diffraction and drag. Diffraction loading is related to the peak overpressure of a blast wave as it passes over and around an object or structure. Peak overpressure refers to the pressure above ambient at a given location (often termed side-on overpressure). In this instance overpressure

refers to the pressure above ambient upon blast wave interaction with an object or structure. Diffraction loading refers to the force exerted on an object or structure during blast wave envelopment. The loading consists of two components; firstly, that resulting from the pressure differential that exists between the front and back of an object/structure prior to envelopment and secondly, static loading ("crushing" forces) due to the pressure differential between internal and external environments. The process of envelopment is described in detail by Glasstone and Dolan [4]. Essentially, upon striking an object or structure blast wave reflection occurs. This not only changes blast wave direction but also its momentum as it collides with the "winds" following its passage. Such collision results in a rapid rise in pressure termed the reflected overpressure. As the pressure drops the blast wave bends or "diffracts" over and around the structure loading other faces. In comparison, drag loading is related to dynamic pressure. This is the air pressure behind a shock front and unlike overpressure has no reference to ambient pressure. Forces exerted by drag loading are the result of transient winds which accompany the passage of a blast wave.

For very large explosions (peak overpressure greater than about 4.8 bar) dynamic pressure is greater than peak overpressure. As a consequence of this drag loading tends to be the main cause of damage in large explosions. This can also be the case where objects and structures present little resistance to blast waves. For example, buildings whose walls, windows and doors rapidly fail during blast wave interaction cause prompt equalisation of interior and exterior environments. This in turn can reduce the duration and magnitude of diffraction loading to a negligible level [4]. (This is one means by which the effects of diffraction loading can be minimised.) For the types of explosions considered here peak overpressure is greater than dynamic pressure and therefore damage is largely the result of diffraction loading. However, this is not always true. It should be noted that all objects and structures simultaneously suffer both diffraction and drag loading. This is because overpressure and dynamic pressure both exist during blast and cannot be separated. The relative importance of each load type is largely dependent on size, shape, weight and resistance of objects and structures. Closed or semi-closed structures, such as buildings with small openings or large tanks, etc. are vulnerable to diffraction loading, whereas, tall thin objects and buildings with large openings are vulnerable to drag loading. The discussion given here, together with Table 1, provides a rough guide in judging the type of load most important to particular objects and structures. A detailed appraisal of the behaviour of objects and structures to diffraction and drag loading is given by Glasstone and Dolan [4].

Blast wave damage is most commonly related to overpressure. This is probably due to its ease of measurement and estimation compared with other damage-relation criteria. However, blast wave damage is also a function of rate of pressure rise and wave duration. As a consequence of this, impulse is also used as a measure of blast damage. Impulse is a function of both overpressure

TABLE 1

Principal loading vulnerability of structures and objects (after Glasstone and Dolan [4])

Structures susceptible to diffraction loading	Structures and objects susceptible to drag loading
Multi-storey reinforced concrete buildings with concrete walls, small window areas, 3–8 storeys	Light steel frame industrial buildings, low strength walls which quickly fail, single storey
Multi-storey wall-bearing buildings, brick apartment houses, up to 3 storeys	Heavy steel frame industrial buildings, lightweight low strength walls which quickly fail, single storey
Multi-storey wall-bearing buildings, monumental types, up to 4 storeys	Multi-storey steel frame office-type building, lightweight low strength walls which quickly fail, both earthquake and non-earthquake resistant, 3–10 storeys
Wood frame buildings, house types, 1 or 2 storeys	Multi-storey reinforced concrete frame office-type building, lightweight low strength walls which quickly fail, both earthquake and non-earthquake resistant, 3–10 storeys.
Highway and railroad bridges	Telegraph poles, electricity pylons
	Transport equipment and vehicles
	Trees and vegetation

and wave duration and therefore is often considered a better measure of blast wave damage. However, using impulse as a damage-relation criterion can cause confusion. For example, based solely on impulse, blast waves may be assumed to have certain damage potential but in fact be unable to deliver this due to insufficient overpressure [1, 5]. Overpressure itself is not an entirely satisfactory measure of blast damage. This fact has been acknowledged and has led to the development of pressure–impulse correlations commonly known as P–I diagrams or curves. Similarly, distance–charge relationships have been derived (R–W correlations) relating distance and yield to structural response. Unfortunately, both of these techniques suffer from lack of usable data. This is not to say that the techniques are ineffective or unusable, current opinion suggests that P–I and R–W correlations provide improved means of assessing blast damage compared with the traditional overpressure–damage relation [1, 5].

It is apparent that blast damage is not adequately defined by a single parameter, but P–I and R–W correlations, have as yet, limited use due to lack of data. Attempting to relate a number of criteria to the assessment of blast damage is not new. Limits of damage with respect to peak overpressure were suggested by Robinson [6] as long ago as 1944, and more recently by the Explosives Storage and Transport Commmittee [7] (ESTC). The empirical

relationship devised by the ESTC and described by Jarrett [7] is the foundation of the British Safety Distances for military and commercial explosives [5]. Basically blast damage is split into various categories and each category related to yield, distance and housing damage. These relationships and damage categories are illustrated here in Table 2. Using the work described by Jarrett and that of Assheton [8], Scilly and High [5] illustrate not only damage with respect to overpressure and damage category (described by Jarrett [7]) but also with respect to the mass of explosive consumed. The data given by Scilly and High are reproduced here in Table 3. For further detail on damage categories reference should be made to the original work of Jarrett [7].

From the discussion given above, and the fact that much work relating overpressure and blast damage has been performed and recorded, for most practical purposes overpressure provides a good estimation of blast wave damage. An additional reason for the adoption of overpressure as the primary measure of blast damage is possibly due to the fact that in addition to diffraction loading, drag loading can also be related to peak overpressure. This is because the dynamic pressure associated with drag loading is a function of wind speed and air density (behind the shock front) and both of these can be related to peak overpressure [4].

TABLE 2

Housing damage categories in relation to the distance from condensed explosions (after Jarrett [7])

Damage category (constant K)[a]	Description
A (3.8)	Almost complete demolition
B (5.6)	50–75% external brickwork destroyed or rendered unsafe, requiring demolition
Cb (9.6)	Houses uninhabitable — partial or total collapse of roof, partial demolition of one or two external walls, severe damage to load-bearing partitions requiring replacement
Ca (28)	Not exceeding minor structural damage, and partitions and joinery wrenched from fixings
D (56)	Remaining inhabitable after rapair — some damage to ceilings and tiling, more than 10% window glass broken

[a] $R = \frac{KW^{1/3}}{[1 + (3175/W^2)]^{1/6}}$, where R is the distance from condensed explosion (m), W the mass of explosive (kg) and K a constant. Note that "R" defines the average radii for idealised circles within which dwellings suffer the damage associated with a chosen category. Those dwellings that suffer damage for a given category outside the circle are balanced by those within the circle which do not suffer such damage. (The formula and constants are given in imperial units by Jarrett.)

TABLE 3

Explosion damage with respect to overpressure, degree of damage and mass of explosive consumed (after Scilly and High [5])

Structure or object	Damage	Approximate peak overpressure (bar)[a]		
		1 tonne	10 tonne	100 tonne
Window panes	5% broken	0.010	0.007	0.007
	50% broken	0.025	0.017	0.014
	90% broken	0.062	0.041	0.037
Houses	Tiles displaced	0.044	0.029	0.026
	Doors and window frames may be blown in	0.090	0.059	0.053
	Category D damage	0.045	0.030	0.029
	Category Ca damage	0.124	0.079	0.076
	Category Cb damage	0.276	0.165	0.159
	Category B damage	0.793	0.359	0.345
	Category A damage	1.827	0.793	0.758
Telegraph poles	Snapped	3.585	1.793	1.655
Large trees	Destroyed	3.930	1.793	1.655
Primary missiles	Limit of travel	0.014	0.010	0.008
Rail wagons	Limit of derailment	1.827	0.793	0.758
	Bodywork crushed	1.379	0.600	0.579
	Damaged but easily repairable	0.793	0.393	0.379
	Superficial damage	0.317	0.179	0.172
Railway Line	Limit of destruction	14.13	6.688	6.412

[a] All distances (overpressures) from the explosion source are measured to the furthest point of the structure or object (overpressures originally estimated in imperial units, psi).

As a consequence of all the factors discussed above overpressure is used henceforth to describe blast damage. For further details on the rate of pressure rise, wave duration, pressure-impulse and distance-charge correlations (in relation to blast damage) reference should be made to either Baker et al. [1], Kinney [3], Scilly and High [5], Baker [9] or Glasstone and Dolan [4].

A multitude of scaling laws has been devised which relates blast overpressure, charge size and distance etc.. A number of these are discussed by Baker [9]. Far the most popular and widely used is based on the "principle of similarity" proposed by Hopkinson in 1915 (see Turnbull and Walter [10]). Provided the scales used to measure blast from any explosive are altered by the same factors as the dimensions of the relative charges then the properties will be similar. Rather than use the dimensions of the charge it is more practical to use charge weight and assume that explosive charges are compact and symmetrical. This method has been used to develop what is commonly known as the

"cube root" law. Based on the fact that overpressure is related to distance, the scaled distance, Z, at which peak overpressure is known can be found.

$$Z = R/W^{1/3} \tag{1}$$

where Z is the scaled distance ($m/kg^{1/3}$), R the distance from charge (m) and W the charge size (kg).

Strictly the scaling law is based on available energy. However, for simplicity it is assumed that the energy released is proportional to the mass of explosive.

Using the scaled distance in conjuction with Fig. 1 the peak overpressure at distance, R, can be estimated. The graph of peak overpressure vs. scaled distance, shown in Fig. 1, is taken from Lees [2] and is based on data given by Baker [9] for the explosion of TNT. Similar graphs are given by Kinney [3], Brasie and Simpson [11] and Stull [12] and more complex ones by Baker [9]. However, the graph presented here is considered to be a good approximation of peak overpressure with respect to scaled distance. This is because the values obtained from it tend to correspond well with other works [3, 11, 12].

Before further discussing the effects of blast it should be noted that the terms "primary", "secondary" and "tertiary" are not well defined in the literature. Workers appear to use the terms differently. So as to avoid confusion, in this chapter primary refers to all effects directly attributable to the blast wave (e.g. lung haemorrhage and eardrum rupture), secondary refers to all indirect effects such as missile impact and tertiary refers to the damage associated with bodily translation.

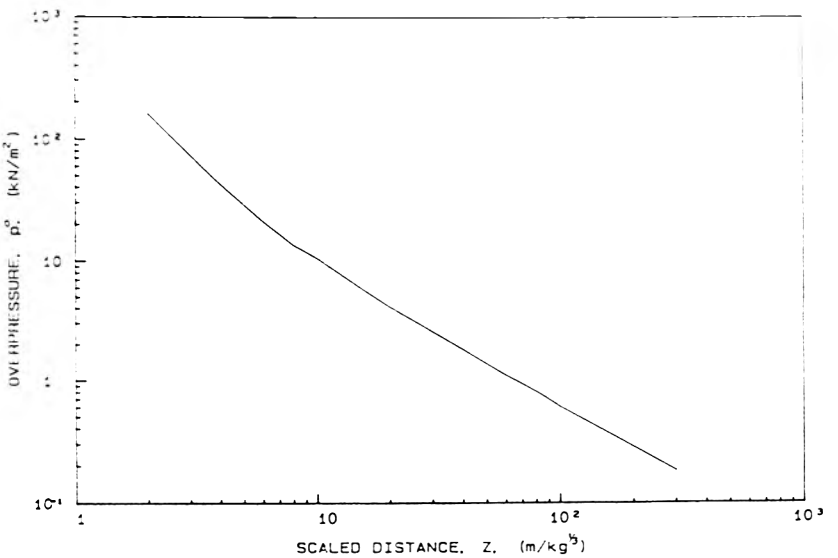

Fig. 1. Peak overpressure vs. scaled distance

Blast damage can effectively be divided into two discrete categories, namely, building damage and human damage. With respect to building damage large amounts of data exist describing and quantifying the effects of overpressure. Robinson [6] provides an extensive analysis of minor and serious damage resulting from blast and Eisenberg et al. [13], using data supplied by Fugelso et al. [14], derive probit equations relating structural damage to peak overpressure. A summary of blast damage with respect to peak overpressure is given by Clancey [15]. This summary is based on work reported by Braise and Simpson [11] and is reproduced here in Table 4. Generally an overpressure of 0.07 bar (1 psi) is considered sufficient to cause partial demolition of typical British brick and concrete constructions, whereas, 0.70 bar (10 psi) is taken as resulting in total demolition. However, these figures are not agreed upon by all. Turnbull and Walter [10] quote 1.5 bar as the onset of considerable building damage. This disagreement may well stem from the omission of certain blast criteria. Unlike human damage, the estimation of building damage tends to be sensitive to the response time of structures and blast reflection. Regardless of these additional criteria it is generally considered that overpressure is adequate in assessing building damage.

Human damage, or as it is more commonly termed injury, is either due to direct blast wave contact or secondary effects, such as, whole body translation and missile impact. The most susceptible parts of the body to blast damage are those organs possessing large density differences amongst neighbouring tissue [16]. As a consequence of this most deaths from blast overpressure (i.e. primary effects) are a result of lung haemorrhage and heart failure. In comparison, minor injury is often based on eardrum rupture, since the ear, although not a vital organ is exceptionally sensitive to pressure. An increase in pressure of only 2×10^{-5} N/m^2 (2.9×10^{-9} psi) will cause the eardrum to move less than the diameter of a single hydrogen molecule [17]. Eisenberg et al. [13] have derived probit equations relating peak overpressure to the likelihood of death. The probit is based on lung haemorrhage and is given by

$$Pr = -77.1 + 6.91 \ln P^{o} \tag{2}$$

where Pr denotes the probit (originally given as Y), and P^{o} is the peak overpressure (N/m^2).

Similarly, they derive a probit equation for minor injury based on eardrum rupture.

$$Pr = -15.6 + 1.93 \ln P^{o} \tag{3}$$

A sample of the results gained using these equations is given in Tables 5 and 6. The equations were developed for early risk assessments and still remain popular although their accuracy has been questioned.

Predicting lung haemorrhage and eardrum rupture is an extremely difficult task and many researchers present differing results. In comparison to the results given by Eisenberg et al. [13] shown in Tables 5 and 6, Turnbull and

TABLE 4

Damage produced by blast (after Clancey [15])

Pressure (bar)	Damage
0.0014	Annoying noise (137 dB), if of low frequency (10–15 Hz)
0.0021	Occasional breaking of large glass windows already under strain
0.0028	Loud noise (143 dB). Sonic boom glass failure
0.0069	Breakage of windows, small, under strain
0.010	Typical pressure for glass failure
0.020	"safe distance" (probability 0.95 no serious damage beyond this value). Missile limit (some damage to house ceilings; 10% window glass broken)
0.028	Limited minor structural damage
0.034–0.069	Large and small windows usually shattered; occasional damage to window frames
0.048	Minor damage to house structures
0.069	Partial demolition of houses, made uninhabitable
0.069–0.138	Corrugated asbestos shattered. Corrugated steel or aluminium panels, fastenings fail, followed by buckling. Wood panels (std. housing) fastenings fail, panels blown in
0.090	Steel frame of clad building slightly distorted
0.138	Partial collapse of walls and roofs of houses
0.138–0.207	Concrete or cinder block walls, not reinforced, shattered
0.159	Lower limit of serious structural damage
0.172	50% destruction of brick work of house
0.207	Heavy machines (3000 lb) in industrial building suffered little damage. Steel frame building distorted and pulled away from foundations
0.207–0.276	Frameless, self-framing steel panel building demolished. Rupture of oil storage tanks
0.276	Cladding of light industrial buildings ruptured
0.345	Wooden utilities poles snapped (telegraph poles, etc.) Tall hydraulic press (40,000 lb) in building slightly damaged
0.345–0.483	Nearly complete destruction of houses
0.483	Loaded train wagons overturned
0.483–0.552	Brick panels, 8–12 in. thick, not reinforced, fail by shearing or flexure
0.621	Loaded train box-cars completely demolished
0.689	Probable total destruction of buildings. Heavy machine tools (7000 lb) moved and badly damaged. Very heavy machine tools (12,000 lb) survived
20.68	Limit of crater lip

TABLE 5

Probability of fatality from lung haemorrhage for a given overpressure (after Eisenberg et al. [13])

Probability of fatality (%)	Peak overpressure	
	(bar)	(psi)
1	1.00	14.5
10	1.20	17.5
50	1.40	20.5
90	1.75	25.5
99	2.00	29.0

TABLE 6

Probability of eardrum rupture for a given overpressure (after Eisenberg et al. [13])

Probability of eardrum rupture (%)	Peak overpressure	
	(bar)	(psi)
1	0.17	2.4
10	0.19	2.8
50	0.44	6.3
90	0.84	12.2

Walter [10] quote a figure of 3 bar rather than 1.4 bar as the pressure needed to cause 50% fatalities from lung haemorrhage. Similarly, Baker et al. [1] using the results of Vadala [18], Henry [19] and Reider [20] have produced a plot of the percentage of eardrum ruptures vs. peak overpressure. From the plot they estimate that the probability of eardrum rupture at 1 bar (14.5 psi) is approximately 50% and not 90% as given by Eisenberg et al. The plot presented by Baker et al. is reproduced here in Fig. 2. More recently Pietersen [21] has described probit relations derived by TNO [22] for the estimation of injury based on lung haemorrhage and eardrum rupture. The probits are derived in part from the abundance of work performed on explosion effects at the Lovelace Foundation [23] in the US during the 1950's and 1960's, in particular the work performed by Bowen et al. [24], Fletcher and Bowen [25], White [16] and Hirsch [26]. The probits based on lung haemorrhage and eardrum rupture illustrated by Pietersen provide similar results (marginally lower) to those given by Eisenberg et al. [13] and are therefore not detailed here.

Death and non-fatal injury from secondary effects, as previously stated, is generally the result of bodily translation or missile contact. The effects of

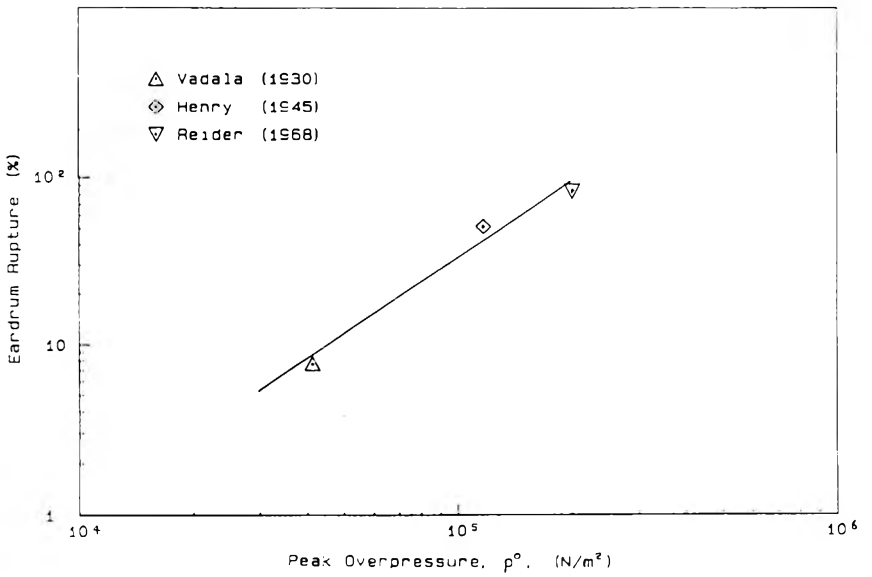

Fig. 2. Eardrum ruptures (%) vs. overpressure (after [18–20]).

missiles on the human body are dealt with in Chapter 3.0 and are not discussed here. Bodily translation consists of displacement and subsequent decelerative impact with the ground, building materials and/or other objects. Damage occurs as a result of the head or other vulnerable body parts colliding with hard surfaces causing fracture, concussion and/or haemorrhage (known as tertiary damage). The degree of injury is related to impact velocity, duration, terrain, distance thrown, impacting surface and orientation. Baker and Oldham [27] have developed a method of quantifying damage caused by bodily translation based on specific impulse and incident overpressure. Using the method together with data gained through White [16] and Clemedson et al. [28] tertiary damage is expressed in terms of impact velocity. Abstracted results from Baker and Oldham [27] are given in Tables 7 and 8. Longinow et al. [29] have also estimated tertiary damage. They derive a relationship between the probability of death and impact velocity. A graphical representation of the relationship is reproduced here in Fig. 3. It can be seen that the values given by Baker and Oldham correspond well with the relationships given by Longinow et al. for skull and whole body impact.

Other characteristics associated with blast waves, such as, toxic gases, ground shock and crater are considered here to be insignificant compared with those effects described above. This is because such phenomena only become a serious hazard in exceptionally large or confined (toxic gases) explosions. Additionally, the likelihood of death or injury from such effects is small compared with death or injury from direct and indirect blast effects. Therefore, the effects of toxic gases, ground shock and crater are not discussed here.

TABLE 7

Criteria for tertiary damage (decelerative impact) to the head (after Baker et al. [1, 27])

Skull fracture tolerance	Related impact velocity (m/s)
Mostly "safe"	3.05
Threshold	3.96
50 percent	5.49
Near 100 percent	7.01

TABLE 8

Criteria for tertiary damage involving total body impact (after Baker et al. [1, 27])

Total body impact tolerance	Related impact velocity (m/s)
Mostly "safe"	3.05
Lethality threshold	6.40
Lethality 50 percent	16.46
Lethality near 100 percent	42.06

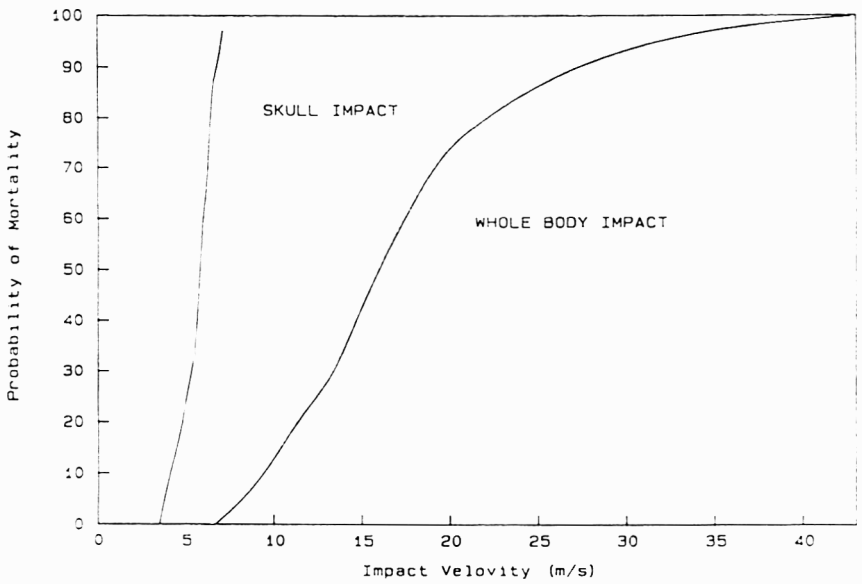

Fig. 3. Fatality criterion: Bodily translation (after [29]).

Further information. with respect to these phenomena can be gained through Lees [2], Robinson [6], Clancey [15] and Pietersen [21].

3. Missile damage and injury

Fragment generation, as a result of explosion, can produce significant damage to receiving medium. Energy delivered to fragments from blast waves cause fragments to become airborne and act as missiles characterised by velocity, range and penetration. Such missiles are often classed as being either primary or secondary [1]. Primary missiles consist of casing and/or container fragments from the explosive item, whereas, secondary missiles consist of fragments from objects located close to the explosion source which have interacted with the blast wave.

Unlike the one or two large fragments which result from typical storage vessel "bursts" [1, 30], the casings and packages of high explosives rupture into large numbers of small primary fragments. Although the fragments are small and irregular, they are generally of a "chunky" appearance (inasmuch that all linear dimensions are of a similar magnitude) and for typical shell casings weigh in the region of one gram [31, 32]. In addition, high explosive primary missiles have velocities over ten times that of typical pressure burst fragments; velocities approaching several thousand metres per second are not uncommon [31].

Secondary missiles, as mentioned above, are the result of blast wave interaction with objects located near to the source of explosion. Such fragments are often termed as being either "constrained" or "unconstrained". The terminology depends upon whether the blast wave tears them from their fixings [1] or simply "up-roots" them from their position. The fragments may take a multitude of forms from building materials through to vegetation. Velocity, range and penetration of secondary missiles are, in the main, much less than those of primary types. However, it is not unknown for blast waves to accelerate secondary fragments to velocities where they become capable of inflicting serve impact damage [1, 32].

It is not the intention of this work to explain in-depth the means of calculating, from accidental explosions, missile projectory, penetration, range or velocity. Much work has already been done on these subjects. A brief description is given by Lees [2] and detailed accounts by Baker et al. [1], Clancey [15] and High [33]; all of these contain references to other works. However, for completeness a brief description of the methods used to calculate missile velocity, range and penetration is included here.

Missile velocity can be estimated through the consideration of explosion energy. For typical fragments from cased [2] charges initial fragment energy varies from between 20% and 60% of the explosion energy. Initial fragment velocity can be calculated from

$$E = \tfrac{1}{2}MV^2 \tag{4}$$

where E is the initial kinetic energy of the fragment (J), M fragment mass (kg), and V the initial fragment velocity (m/s).

Clancey [15] estimates that for the majority of fragments, resulting from TNT explosions, fragment velocities are as follows: Thin case 8000 ft/s (2438 m/s), medium case 6000 ft/s (1829 m/s), and thick case 4000 ft/s (1219 m/s).

The velocities have been estimated from empirical data on the assumption that any size charge will propel fragments the same distance. Although this assumption is untrue, since large explosions propel fragments further than small explosions, the estimates do assist in preliminary analysis. Clancey [15] also details an empirical calculation of missile range. Modifying the formula in order to incorporate SI units, the range is given by

$$X=(W^{1/3}/ka)(\ln U/V) \tag{5}$$

where X denotes the range (m), W fragment mass (kg), U initial fragment velocity (m/s), V fragment velocity (m/s), k is a constant (0.002 velocity supersonic, 0.0014 velocity subsonic) ($kg^{1/3}/m$), and a is the drag coefficient.

Drag coefficients are a function of fragment shape and orientation during flight. Typical drag coefficients range between about 0.8 and 2.0, with regular symmetric shapes tending towards the lower values. A number of drag coefficients for various shapes and flight orientations is given by Hoerner [34].

Missile penetration is examined in-depth by Clancey [15] and Baker et al. [1]. However, the equation given below is from neither of these sources, but is considered suitable for approximating penetration through building materials by fragments of less than 1 kg (this is useful here since casing fragments are generally much less than 1 kg, as indicated previously). The equation is taken from the High Pressure Safety Code [35] which suggests that a safety factor of between 1.5 and 2 should be applied to the results. It should be noted that irregular fragments may have a penetration capability only half of that calculated, whereas, pointed fragments may penetrate even further.

$$t=kM^aV^b \tag{6}$$

where t is the penetration (m), M fragment mass (kg), and V fragment velocity (m/s). The constant "k" and exponents "a" and "b" in eq. (6) vary depending on target material, as follows: Concrete (crushing strength 35 MN/m^2) 18×10^{-6}, 0.40, 1.5; Brickwork 23×10^{-6}, 0.40, 1.5; and Mild steel 6×10^{-5}, 0.33, 1.0.

Damage caused by missiles, needless to say, can vary from superficial to extensive. As a guide the Explosives Storage and Transport Committee [36] (ESTC) estimate that lethal missiles, with regards to humans, are missiles having approximately 80 J of kinetic energy. The ESTC also suggest that one fragment per 56 square metres provides individuals who are out in the open with a 1% chance of being hit. Buildings and other relatively large objects can be crushed or penetrated by missiles leading to minor hazards, such as, falling debris and glass breakage. However, impulsive loading during

impact, especially from large heavy missiles, presents the greatest indirect hazard. This is because impulsive loads may instigate or encourage collapse of structures and/or escalate the amount and rate of falling debris and glass breakage. All of these missile effects may also lead to the initiation of secondary fires adding further injury. Secondary fires are discussed in Chapter 4.

The term "indirect hazard" as used above refers to all damage caused to solid media, such as, building materials and vehicles which may then present a hazard to man. It follows that "direct hazard" refers to direct injury of the human body as a result of actual physical missile contact. The majority of injuries from direct hazards relate to skin laceration and open wounds. If the velocity of the missile is sufficient and contact is made with vital organs then death may result. Experiments on skin penetration have been performed by Sperrazza and Kokinakis [37]. They have found that a relationship exists between missile mass and exposed cross-sectional area. This relationship is based on a limiting velocity (V_{50}) which corresponds to a 50% probability of skin penetration. The tests, performed with steel cubes, spheres and cylinders impacting 3 mm thick human/goat skin, assume that all missile penetration causes severe damage. Sperrazza and Kokinakis conclude that limiting velocity depends linearly on the ratio of fragment area and fragment mass, as shown by eq. (7).

$$V_{50} = k(A/M) + b \tag{7}$$

for $A/M > 0.09$ m^2/kg and $M > 0.015$ kg, where V_{50} is the limiting velocity (m/s), A the CSA of missile along trajectory (m^2), M the mass of fragment (kg), k is a constant (1247.1) and b is a constant (22.03).

From further work Sperrazza and Kokinakis [38] have found that skin *in situ* can be penetrated at lower impact velocities than isolated skin. The results are contrary to that expected when one considers that *in situ* fragments must traverse 10 mm of skin and subcutaneous tissue rather than 3 mm of isolated skin in laboratory tests. A number of results based on isolated skin tests are detailed in Table 9.

Other work has been performed on skin penetration. Unfortunately, direct comparisons with the findings of Sperrazza and Kokinakis are difficult to make as a result of the many differing approaches to the problem. However, Baker et al. [1] using a number of simplifying assumptions, have compared results compiled by other researchers, as shown in Fig. 4. It can be seen from Fig. 4 that the relationship estimated by Sperrazza and Kokinakis compares well with the findings of Glasstone [4], White et al. [39], Custard and Thayer [40] and Kokinakis [41]. More recently Pietersen [21] has described a relationship derived by TNO [22] relating the probability of fatality with regards to skin penetration based on fragment velocity and mass. The relationship is in the form of a probit equation, as shown below, and is applicable to fragments of less than 0.1 kg.

$$Pr = -29.15 + 2.10 \ln S \tag{8}$$

TABLE 9

Comparison of methods estimating probability of fatality from non-penetrating missile impact

Probability of fatality (%)	Fragment impact velocity (m/s)	
	Ahlers[a]	Pietersen[b]
0.5 kg fragment		
10	17	14.9
50	23	16.8
90	30	19.0
10 kg fragment		
10	8	5.0
50	11	5.6
90	13	6.3

[a] Approximate values from Ahlers [42].
[b] Approximate values from Pietersen [21].
For non-penetrating fragments between 0.1 kg and 4.5 kg: $Pr = -17.56 + 5.3 \ln S$, where $S = \frac{1}{2}MV^2$: and for non-penetrating fragments greater than 4.5 kg: $Pr = -13.19 + 10.54 \ln V$.

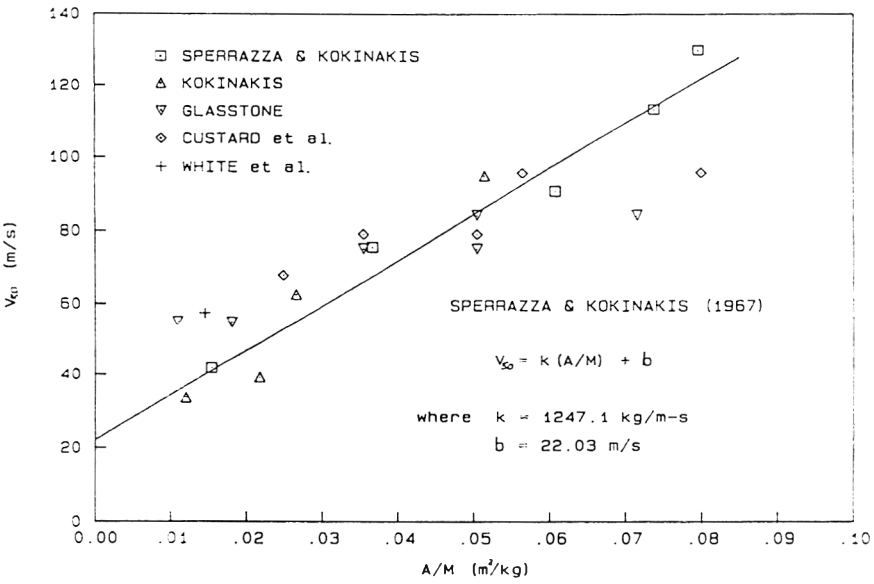

Fig. 4. Ballistic limit (V_{50}) vs. fragment area/mass for isolated human and goat skin (after [1]).

where S equals $MV^{5.115}$, in which M is the fragment mass (kg), and V fragment velocity (m/s).

Not all fragments are penetrating. Non-penetrating fragments may cause injury or death by virtue of their mass and velocity being so great that they inflict bodily translation and/or crushing effects. Such action usually results in cerebral concussion, fracture, haemorrhage and/or serve bruising of the victim. Ahlers [42] has studied the effect of non-penetrating missiles on individuals, the results of which are presented here in Fig. 5. Pietersen [21] illustrates two probit relations derived by TNO [22] for the probability of fatality from such missiles. For fragments between 0.1 kg and 4.5 kg the probit is related to kinetic energy, such that

$$Pr = -17.56 + 5.30 \ln S \tag{9}$$

where

$$S = \tfrac{1}{2}MV^2 \tag{10}$$

and M and V are as given above for skin penetration. For fragments greater than 4.5 kg the probit is related to skull fracture and given by

$$\mathrm{Pr} = -13.19 + 10.54 \ln V \tag{11}$$

where V is the fragment velocity.

Results obtained using the above probits differ from the results presented by Ahlers [42]. Given the same size fragment, compared with Ahlers, the probit

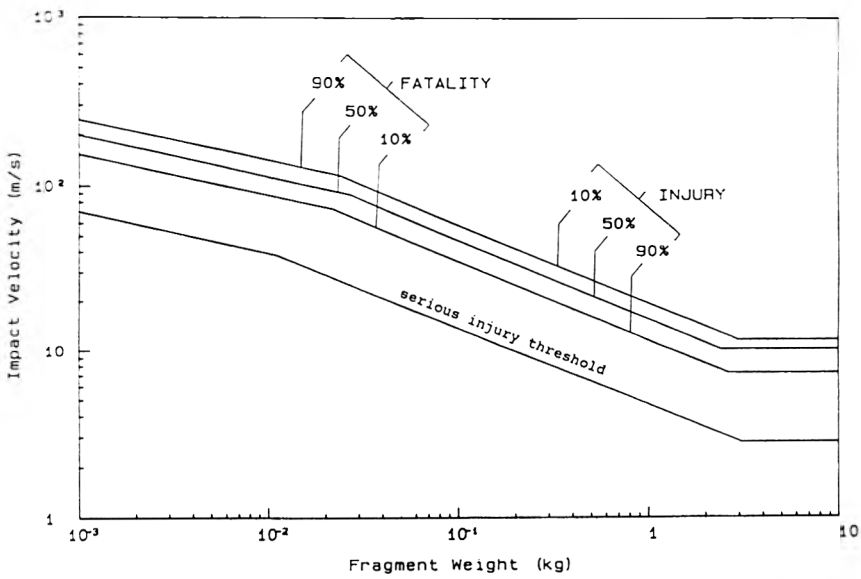

Fig. 5. Fragment impact: Human response to non-penetrating missiles (after [41]).

based on kinetic energy (i.e. fragments 0.1 kg–4.5 kg) implies that a greater impact velocity is needed to attain a specific probability of fatality. In comparison, the probit based on skull fracture (i.e. fragments >4.5 kg) implies a lower impact velocity is needed to attain a specific probability of fatality. However, there are similarities between the study conducted by Ahlers [42] and the probits presented by Pietersen [21] suggesting that they are asymptotic of a more general solution. For example, both suggest that the probability of fatality from large fragments (unlike small fragments) is related simply to impact velocity.

Further information on the effects of missile impact, with respect to humans can be gained through White [16], TNO [22], Clemedson et al. [28], Sperrazza and Kokinakis [37] and Kokinakis [41].

4. Thermal damage and injury

Extensive thermal damage from explosions is usually caused by the phenomenon of fireball growth. Fireballs cause damage as a result of igniting combustible materials and injuring humans by direct immersion and intense radiation. Thermal damage may also occur as a result of secondary fires. These fires are initiated either by instantaneous combustion of materials due to radiation exposure above material threshold levels or by missile and blast interaction with ignition sources. The number of secondary fires caused by explosion is extremely hard to quantify. For propane explosions Geffen et al. [43] have estimated the number of secondary fires as a factor of heat radiation threshold and building density. It is suggested here that a similar analogy could be employed for commercial and military explosives. Compared with fireballs, secondary fires present only a minor thermal hazard and, as such, their specific characteristics are not expanded upon here. Detailed information on secondary fires can be gained through Lees [2], Geffen [43] and Rausch et al. [44].

As previously mentioned, the major hazard from fireballs is the effect of thermal radiation damage. As a result of this most investigations into fireball characteristics have concentrated on radiant rather than conductive and convective heat transfer. However, it has been suggested by Baker et al. [1] that for small fireballs, in which less than 10 kg of substance are consumed, heat transfer by conduction and convection may play a substantial part in the heat transfer process. Regardless of this omission, for the purposes of consequence analysis, the current catalogue of research tends to support historical data collected on fireball incidents. The most authoritative work in this field is given by Rakaczky [45], with regards to munitions explosions, Gayle and Bransford [46], High [47], Bader et al. [48] and Hasegawa and Sato [49] with regards to liquid propellants and fuel explosions, and Roberts [50] with regards to releases of liquefied petroleum gas (LPG). It should be noted that much work in this field relates specifically to nuclear explosions [4]. Unfortunately the results gained on fireballs from nuclear explosions do not correspond well with

data collected on fireballs resulting from chemical explosions. This disparity should be borne in mind when attempting fireball analysis. This work is chiefly concerned with commercial and conventional military explosives, and therefore the following discussion on fireball growth and damage omits any reference to nuclear explosions.

Evaluation of fireball consequences for hazard assessment requires the quantification of fireball temperature, fireball duration and fireball size. Temperature is dependent on the heat capacity of the fuel consumed and means of combustion (i.e. diffusion flame where air diffuses into the fuel or pre-mixed flame where air and fuel exist as a mixture). Fireball temperatures can vary from approximately 1350 K for flammable gases to about 5000 K for chemical explosives. It is important to note this fact when using fireball models so as to avoid erroneous conclusions. For example, High's [47] predictions for fireball size and duration are based on liquid propellants having fireball temperatures of 3600 K, whereas, Rakaczky's [45] estimates are for fuels, such as, propane, pentane and octane which have substantially lower fireball temperatures (i.e. approximately 2500 K). Similarly, Roberts [50] equations relate to propane fireballs. However, variations between fireball models are largely dependent upon the mass of substance consumed, and as such size and duration estimates may vary by as much as 50%.

As stated above, estimation of fireball size and duration varies from model to model. It is suggested by Baker et al. [1] that the results from the various models, used to estimate size and duration, are asymptotic or limiting cases of a more general solution. This claim is supported by the mathematical similarities between the models and the fact that some methods are suitable for use on fireballs consuming small quantities (i.e. less than 10 kg — Hasegawa and Sato [49]), whereas, others are best used on fireballs consuming relatively modest quantities of material (i.e. more than 20 kg — High [47] and Rakaczky [45]). However, from a review of fireball models Roberts [50] suggests that for a large range of releases (1 kg to over 100,000 kg) the following equation provides a reasonable approximation of fireball size.

$$D = 5.8\, M^{1/3} \tag{12}$$

where D is the fireball diameter (m), and M the mass consumed (kg).

Similarly, Roberts suggests that for fireballs consuming less than 5 kg fireball duration is best estimated by

$$T = 1.1\, M^{0.097} \tag{13}$$

and for quantities greater than 5 kg

$$T = 0.83\, M^{0.316} \tag{14}$$

where T denotes the fireball duration (s), and M the mass consumed (kg).

Duration time, T, is referred to here as the period during which fireballs radiate heat. Further time-scales (of minor importance here) are those associated

with duration of combustion with regards to momentum, buoyancy and deflagration and time for fireball "lift-off". These time-scales are discussed in detail by Roberts [50] together with three distinct stages of fireball development, namely:

(a) rapid growth (rapid combustion, dominated by initial momentum of release, very bright flame),
(b) little change in size (dominated by buoyancy and combustion effects, flame cooling from bright yellow to dull orange),
(c) fireball lift (rapid cooling, dominated by buoyancy effects).

The main difficulty in estimating duration stems from the absence of a discrete point as fireballs lose heat. A general consensus has not been reached on the estimation of duration and therefore large deviation is often found between fireball models. In comparison, the estimation of fireball size tends to be more consistent. This is because most hazardous materials generate fireballs which expand rapidly reaching a maximum size which is maintained for a measurable time until collapse. Rakaczky [45], in a literature review of explosions, observed that fireball size and duration can be expressed by

$$D = 3.76\, M^{0.325} \tag{15}$$

and

$$T = 0.258\, M^{0.349} \tag{16}$$

Unfortunately, no limits of applicability are given for the equations above and therefore they should be used with caution. Baker et al. [1], however, contend that Rakaczky's equations are for fireballs with temperatures approximating 2500 K. Other researchers, namely High [47] and Hasegawa and Sato [49], have evaluated similar equations, abstracted results of which are shown in Tables 10 and 11. It is suggested by Baker et al. that High's equations should

TABLE 10

Comparison of methods estimating fireball duration (after Baker et al. [1])

Mass (kg)	Time (s)			
	Rakaczky	High	Hasegawa and Sato	Roberts
1	0.26	0.30	1.07	1.10
10	0.58	0.63	1.62	1.72
10^2	1.29	1.31	2.46	3.56
10^3	2.87	2.74	3.74	7.36
10^4	6.42	5.72	5.67	15.00
10^5	14.00	12.00	8.60	32.00
10^6	32.00	25.00	13.00	65.00
10^7	79.00	52.00	20.00	135.00

TABLE 11

Comparison of methods estimating fireball size (after Baker et al. [1])

Mass (kg)	Diameter (m)			
	Rakaczky	High	Hasegawa and Sato	Roberts
1	3.76	3.86	5.25	5.80
10	7.95	8.06	11.00	13.00
10^2	17.00	17.00	22.00	27.00
10^3	36.00	35.00	46.00	58.00
10^4	75.00	74.00	95.00	125.00
10^5	159.00	154.00	195.00	269.00
10^6	335.00	321.00	402.00	580.00
10^7	708.00	671.00	828.00	1250.00

be used for liquid propellants having fireball temperatures of approximately 3600 K and where more than 20 kg of hazardous material is consumed, and that Hasegawa and Sato's equations be employed on fireballs consuming less than 10 kg.

High [47] $D = 3.86\,M^{0.32}$, $T = 0.299\,M^{0.32}$ (17)

Hasegawa and Sato [49] $D = 5.25\,M^{0.314}$, $T = 1.07\,M^{0.181}$ (18)

The models discussed above have yet to be refined so as to incorporate conductive and convective heat transfer mechanisms, which may greatly affect heat loss in small fireballs, as previously mentioned. In addition, the emissivity of fireballs has not been fully addressed. Most models assume emissivity values of between 0.7 and 1.0. However, some fireballs have extremely low "black-body" capabilities rendering the above equations inappropriate (e.g. hydrogen fireballs).

Fireball size and duration is summarised in Table 12.

Fireball consequence analysis takes the form of estimating thermal radiant heat flux and, subsequently, radiated thermal energy. The treatment and derivation of these parameters are complex and for the purposes of this paper need no full description. A suitable explanation is given by High [33] and Baker et al. [1]. It is sufficient here to note that the analysis is based on fireball size, temperature and duration. On the assumption that fireball size and temperature remain constant High derives the following equations for radiant heat flux, q, and radiated energy per unit area, Q.

$$(q/o^4) = (GD^2/R^2)/(F + D^2/R^2) \tag{19}$$

$$Q/(bGM^{1/3}o^{2/3}) = (D^2/R^2)/(F + D^2/R^2) \tag{20}$$

where q is the heat flux (J/m^{2}s—i.e. W/m^2), Q the radiated energy (J/m^2), D the diameter of fireball (m), o the temperature of fireball (k), R the distance to

TABLE 12

Fireball size, D, and duration, T, parameters from $D = AM^B$ and $T = AM^B$

Model	Diameter (m)		Duration (s)	
	A	B	A	B
High[a]	3.86	0.320	0.299	0.320
Hasegawa and Sato[b]	5.25	0.314	1.070	0.258
Rakaczky[c]	3.76	0.325	0.258	0.349
Roberts[d]	5.8	0.333	0.830	0.316
Roberts[e]	–	–	1.100	0.097

[a] High [47] – liquid propellants and fuel explosions, fireball temperatures approx. 3600 K, greater than 20 kg.
[b] Hasegawa and Sato [49] – liquid propellants and fuel explosions, less than 10 kg.
[c] Rakaczky [45] – munition explosions, fireball temperatures approx. 2500 K.
[d] Roberts [50] – propane, 1 kg to over 100,000 kg.
[e] Roberts [50] propane, less than 5 kg.

fireball (stand-off distance) (m), M the consumed mass (kg), F a transmission coefficient (161.7), G a transmission coefficient (5.26×10^{-5}), and bG the transmission product (2.04×10^4).

Both equations above are based on static fireball diameters. High [33] (employing a time variant analogy) has shown that equations can be derived to allow for fireball growth. However, these are not expanded upon here since they add little to the assessment of fireball damage.

Radiated heat, E, is given by Roberts [50] as

$$E = FMQ/T \tag{21}$$

where E denotes a radiated heat (kW), F a fraction of total heat released (0.2–0.4), M a mass consumed (kg), Q a heat of combustion (kJ/kg), and T a fireball duration (s) (where $T = 0.45 M^{1/3}$).

From the above the intensity of heat radiation on a target perpendicular to the direction of radiation (i.e. heat flux) is given by

$$I = E/4\pi L^2 \tag{22}$$

where I is the intensity of heat radiation (kW/m^2) (note; "I" is referred to as "q" in the equations given by High [33]), E the radiated heat (kW) and L a distance from centre of fireball to target (m).

The effect of fire on buildings can be related directly to the intensity of radiated heat (i.e. heat flux). Most research has concentrated on the ignition of wood [1, 51]. Lawson and Simms [51] estimate spontaneous ignition of wood from the following equation.

$$(q - q_s)t^{4/5} = k \tag{23}$$

where q is the heat flux (W/m^2), q_s the critical heat flux for spontaneous ignition (25,400 W/m^2), t the duration of heat flux (s), and k is a constant (6730).

The equation given above is based on empirical data and is a general relationship for all types of wood. The critical radiation intensity (i.e. heat flux) to cause spontaneous ignition of wood is given as 25.4 kW/m^2. Other relationships for differing materials exist. However, the vast majority refer to nuclear explosions which are not strictly comparable with chemical explosions, as previously explained. For further information reference should be made to Glasstone and Dolan [4] and Baker et al. [1].

Damage to the human body from thermal radiation may result in death or injury from severe burns. Injury caused by radiation can be quantified by temporary or permanent loss of sight. Miller and White [52] have derived relationships linking heat flux and choriorentinal burns with respect to time. However, thermal radiation injury is more commonly based on the burning of bare skin [1, 13, 53]. Buettner [53] estimates human pain with respect to heat flux. Figure 6 illustrates the relationship derived by Buettner with respect to heat flux for non-nuclear fires. The two lines shown provide a split between bearable and unbearable pain (second degree burns). Unbearable pain is said to occur [53] when a temperature of 44.8 °C is exceeded at a skin depth of 0.1 mm. Exceeding such a temperature rapidly increases the victim's pain. The pain then gradually fades indicating that total skin irradiation has occurred. It is stated by Hymes [54] that for each increase of 1 °C above the threshold the rate of injury is trebled. For example, compared with the threshold the damage rate is roughly 100 times greater at 50 °C.

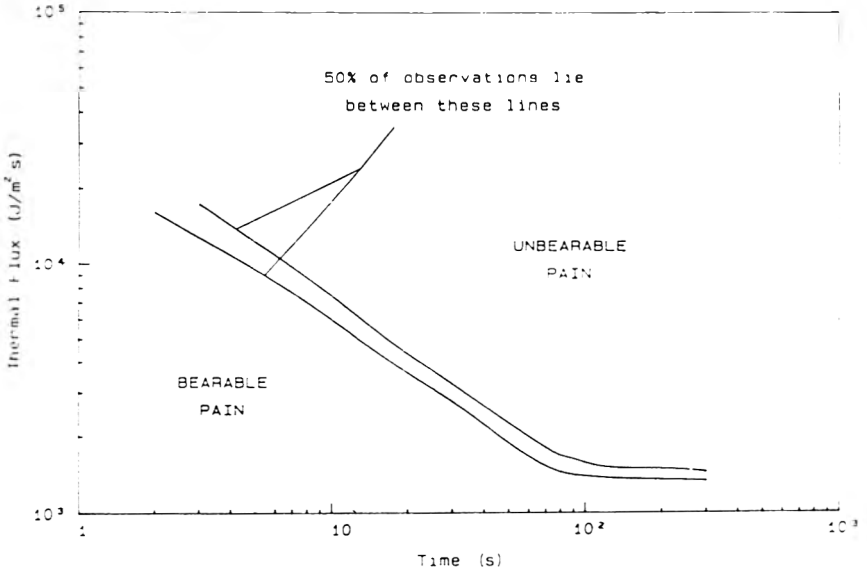

Fig. 6. Threshold of pain from thermal radiation on bare skin (after [58]).

The probability of death from second degree burns has been estimated by the US Department of the Army [55]. They derive a plot of the probability of fatality vs. the percentage of second degree burns, as shown in Fig. 7. Exposed skin varies from season to season but is estimated to average [43] about 27%. This estimate of skin exposure approximates to the exposure of the head and both arms. Thus, from Fig. 7 it can be seen that the probability of fatality from second degree burns for average skin exposure is about 10%.

A detailed review of the physiological and pathological effects of thermal radiation is given by Hymes [54] together with new information. It is broadly concluded that those exposed to heat fluxes capable of inflicting third degree burns within 10 seconds are unlikely to survive. Precise probabilities of injury and survival are difficult to gauge. The effects of radiation burns are related to burnt surface area, depth of burn, age of recipient and clothing characteristics, etc. All of these factors are discussed by Hymes [54].

Probability of death with respect to the proportion of body surface area burnt is given by Pietersen [21] and reproduced here in Table 13. As a "rule of thumb" it is suggested by Hymes [54] that for 15% burnt surface area (adult, head and hands) and injury no worse than second degree-plus all healthy adults under 50 can be expected to survive, whereas, 50% of those over 60 can be expected to die. Compared with adults the proportion of infants surviving is somewhat lower. This is due to the greater surface area exposed (i.e. head and hands approximate 30% of infant area) and the greater medical attention required. The approximate distribution of adult surface area (skin) is given in Table 14.

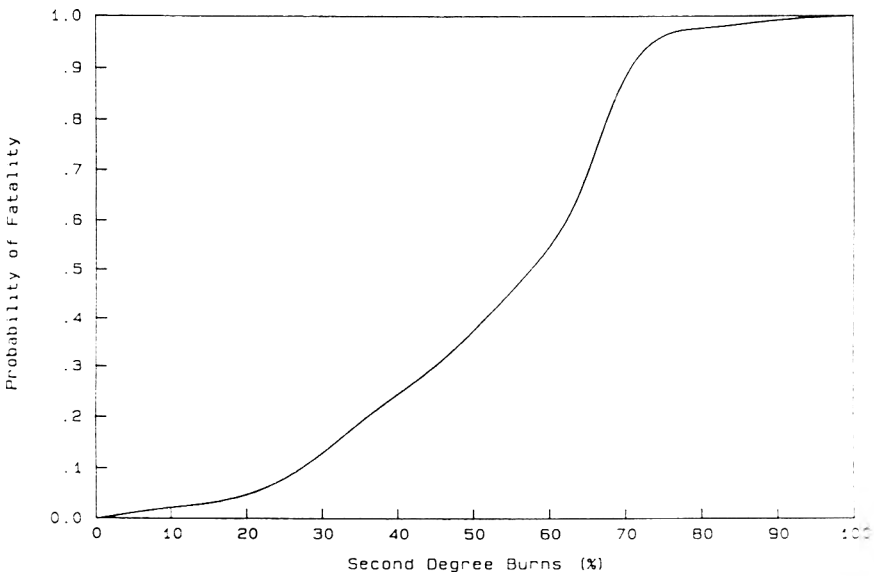

Fig. 7. Fatality criterion: Second degree burns (after [54]).

TABLE 13

Relation between age, proportion of body surface area burnt and mortality rate (after Pietersen [21])

Body area burnt (%)	Age (years)																
	0–4	5–9	10–14	15–19	20–24	25–29	30–34	35–39	40–44	45–49	50–54	55–59	60–64	65–66	70–74	75–79	80+
93+	1	1	1	1	1	1	1	1	1	1	1	1	1	1	1	1	1
88–92	0.9	0.9	0.9	0.9	1	1	1	1	1	1	1	1	1	1	1	1	1
83–87	0.9	0.9	0.9	0.9	0.9	0.9	1	1	1	1	1	1	1	1	1	1	1
78–82	0.8	0.8	0.8	0.8	0.9	0.9	0.9	1	1	1	1	1	1	1	1	1	1
73–77	0.7	0.7	0.8	0.8	0.8	0.8	0.9	0.9	0.9	1	1	1	1	1	1	1	1
68–72	0.6	0.6	0.7	0.7	0.7	0.8	0.8	0.8	0.9	0.9	0.9	1	1	1	1	1	1
63–67	0.5	0.5	0.6	0.6	0.6	0.7	0.7	0.8	0.8	0.9	0.9	1	1	1	1	1	1
58–62	0.4	0.4	0.4	0.5	0.5	0.6	0.6	0.7	0.7	0.8	0.8	0.9	1	1	1	1	1
53–57	0.3	0.3	0.3	0.4	0.4	0.5	0.5	0.6	0.7	0.7	0.8	0.9	1	1	1	1	1
48–52	0.2	0.2	0.3	0.3	0.3	0.3	0.4	0.5	0.6	0.6	0.7	0.8	0.9	1	1	1	1
43–47	0.2	0.1	0.2	0.2	0.2	0.3	0.3	0.4	0.4	0.5	0.6	0.7	0.8	1	1	1	1
38–42	0.1	0.1	0.1	0.1	0.2	0.2	0.2	0.2	0.3	0.4	0.5	0.6	0.8	0.9	1	1	1
33–37	0.1	0	0	0	0.1	0.1	0.2	0.2	0.3	0.3	0.4	0.5	0.7	0.8	0.9	1	1
28–32	0	0	0	0	0.1	0.1	0.1	0.1	0.2	0.2	0.3	0.4	0.6	0.7	0.9	1	1
23–27	0	0	0	0	0	0	0.1	0.1	0.1	0.2	0.2	0.3	0.4	0.6	0.7	0.9	1
18–22	0	0	0	0	0	0	0	0.1	0.1	0.1	0.1	0.2	0.3	0.5	0.6	0.8	0.9
13–17	0	0	0	0	0	0	0	0	0	0.1	0.1	0.1	0.2	0.3	0.5	0.6	0.7
8–12	0	0	0	0	0	0	0	0	0	0	0.1	0.1	0.1	0.2	0.3	0.5	0.5
3–7	0	0	0	0	0	0	0	0	0	0	0	0	0.1	0.1	0.2	0.3	0.4
0–2	0	0	0	0	0	0	0	0	0	0	0	0	0	0.1	0.1	0.2	0.2

TABLE 14

Distribution of skin surface area

Body part	Proportion (%)
Head	7
Trunk	35
Arms	14
Hands	5
Thighs	19
Legs	13
Feet	7

From a number of empirical relations [13,56], and based on an average population, Pietersen [21] derives probits relating burns and death (an average population is not defined). The probits assume approximately 20% exposed surface area. Severity of injury is categorised by the depth of skin to which a temperature difference of 9 K occurs, such that

1st degree burns <0.12 mm skin penetration

2nd degree burns <2 mm skin penetration (24)

3rd degree burns >2 mm skin penetration

The probits given by Pietersen are as follows.

$Pr = -39.83 + 3.0186 \ln (tq^{4/3})$ 1st degree burns

$Pr = -43.14 + 3.0188 \ln (tq^{4/3})$ 2nd degree burns (25)

$Pr = -36.38 + 2.56 \ln (tq^{4/3})$ lethality (death)

where Pr is the probit, t the exposure time (s) and q the heat of radiation (kW/m^2).

For completeness, certain radiation threshold levels and effects are detailed here in Tables 15, 16 and 17.

Finally, it should be noted that transient and steady state fires (for both materials and humans) require differing magnitudes of heat flux for specific levels of damage. For example, first degree burns from secondary fires (steady state fires) are likely from heat fluxes approaching 4.5 kW/m^2 (after 20 s), whereas, similar damage from fireballs (transient fires) can be expected at 125 kJ/m^2. It should be noted that due to the short duration of fireballs total radiated heat is used to estimate damage levels. Tables 15 and 16, which are reproduced in-part from the Rijnmond Public Authority Study [57] into the hazards from a number of chemical installations, serve to illustrate these points.

TABLE 15

Radiation intensity damage: Steady state fires (after Rijnmond Public Authority [57])

Heat flux (kW/m^2)	Effect
37.5	Damage to industrial equipment
25.0	Minimum energy required to ignite wood at infinitely long exposure
4.5	Sufficient to cause pain to personnel if unable to reach cover within 20 s, 1st degree burns likely
1.6	No discomfort to long exposure

TABLE 16

Radiation intensity damage: Transient fires (after Rijnmond Public Authority [57])

Heat flux (kJ/m^2)	Effect
375	3rd Degree burns
250	2nd Degree burns
125	1st Degree burns
65	Threshold of pain, no reddening or blistering of skin

TABLE 17

Pain and blister thresholds with respect to heat radiation intensity and time[a]

Heat flux (kW/m^2)	Time (s)	
	Pain	Blister
3.7*	20.0	–
4.2	13.5	33.8
5.2	10.1	–
6.2*	10.0	–
6.3	7.8	20.8
8.4	5.5	13.4
9.7*	5.0	–
12.6	2.9	7.8
16.8	2.2	5.6
18.0*	2.0	–

[a] Time to threshold of pain, data from Stoll and Greene [58], except time to unbearable pain.
* Data from Buettner [59].

5. Aggregated consequence models

As can be inferred from the information and data presented in this paper, the evaluation of explosion effects is often detailed and prone to inaccuracy. Estimating the number of casualties and extent of building damage is hindered by a multitude of factors, namely

(a) mass of explosive consumed,
(b) distance from source to target,
(c) blast duration,
(d) terrain,
(e) exposure,
(f) fragment generation, velocity, range and projectory,
(g) heat intensity,
(h) structural and material building characteristics.

Furthermore, it is difficult to distinguish between fatalities simply caused by overpressure effects, bodily translation and missile impact. Other causes of death which are hard to distinguish include asphyxia following burial, carbon monoxide poisoning and chronic illness aggravated by shock. In addition to these problems the majority of urban populations will be indoors during an explosion. Only a limited amount of research has been conducted on the effects of explosion with regards to "indoor" populations. The U.S. Department of Transportation [44] have attempted to produce credible methodologies in order to quantify indoor population damage. However, "indoor" and "outdoor" environments are not easily related and no simple scaling laws or means of extrapolating external blast damage to internal blast damage are available. Consequently, the assessment of damage to indoor populations is limited and the accuracy of results poor.

As a consequence of the differences between indoor and outdoor environments, and as a result of the problems outlined above, there are very few simple aggregated consequence models which are useful in estimating damage and casualties from explosion. A number of models have been developed for vapour cloud explosions but very few for those explosions of interest here (i.e. condensed explosions from the accidental initiation of commercial/military explosives). It is apparent from those concerned with explosives safety, that a simple and accurate means of estimating damage and casualties from condensed explosions would be very useful. It is thought here that the best means of achieving this is by the analysis of historical events to produce empirical methods of evaluation. Workers at the University of Technology, Loughborough [60], have adopted this approach and produced a model suitable for the assessment of condensed explosions occurring without warning in built-up areas.

The consequence model developed at Loughborough by Withers and Lees [60] is applicable only to those explosives which have a mass explosion hazard (i.e. UN hazard division 1.1 explosives). Fatalities are estimated from data

collected on historical events and empirical data collected on the effects of blast overpressure. Historical events include World War II bombings, chemical explosions, domestic gas explosions and a number of natural disasters such as earthquakes and tornadoes. Empirical data consist primarily of relationships linking injury and blast overpressure. Due to the difficulties encountered in estimating fatalities cause of death is split into primary and secondary types. Primary deaths are classed as those which occur in the near field and are entirely due to overpressure. The likelihood of death from overpressure is related to impulse and duration. In comparison, secondary deaths are related to housing damage, specifically the number of dwellings made uninhabitable. For every 10 dwellings made uninhabitable one secondary death is assumed. Both primary and secondary deaths are related to distance and mass of explosive consumed and hence are categorised by primary and secondary radii. Individuals who survive within the radii are balanced by those who survive outside the radii. The explosion consequence model is detailed here in Figs. 8 and 9.

The explosion effects model developed at Loughborough [60] suffers from one or two omissions, namely the absence of deaths resulting from casing/packaging fragments and deaths from primary and secondary fires. However, the model estimates well the number of fatalities from a number of historical incidents. Of particular interest is the estimate of fatalities from low yield explosions. The model approximates favourably fatalities from V-2 rocket/bombing raids and other similar sized explosions (0.5 tonne–2 tonne).

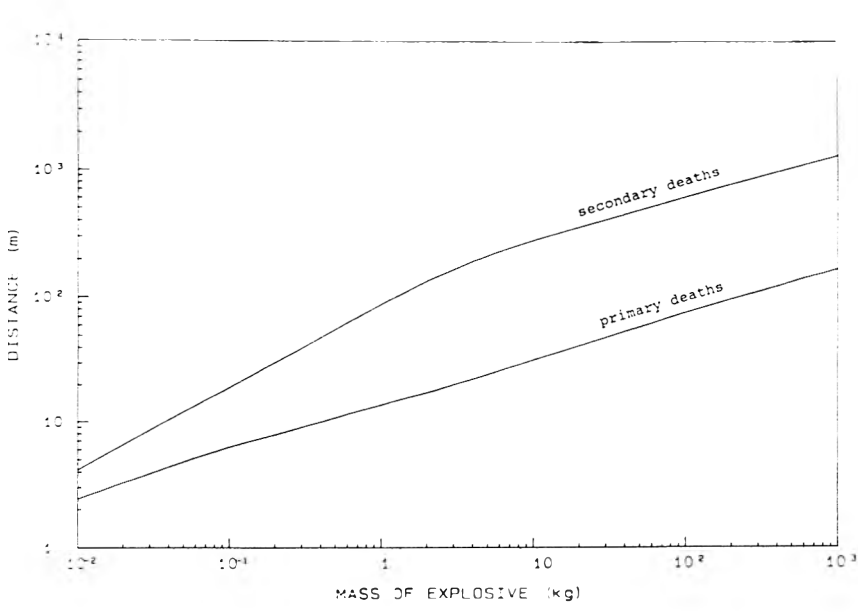

Fig. 8. Primary and secondary causes of death for man: Mass of explosive and distance for 50% mortality (after [59]).

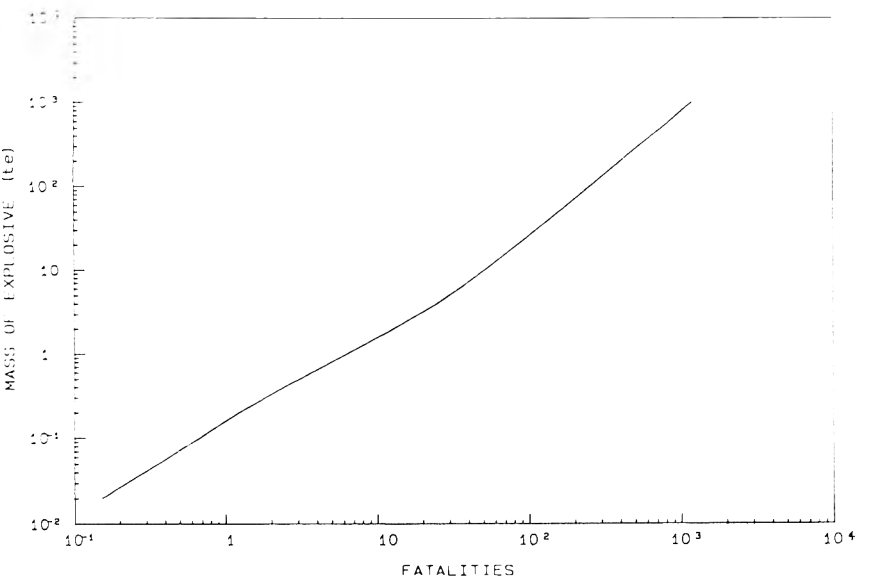

Fig. 9. Model for fatalities resulting from an explosion of a condensed phase explosive in a built-up area (Basis 4000 persons/km^2, 2.5 persons/house [59]).

Regardless of any shortcomings, the author has found no similar "complete" explosion effects models. The model appears to be unique and at present the only one available for the estimation of fatalities from condensed explosions occurring without warning in built-up areas.

Acknowledgements

This paper is based in part on a thesis submitted by the author to the Loughborough University of Technology for the degree of Ph.D., entitled "A Methodology for the Quantitative Risk Assessment of the Road and Rail Transport of Explosives". The thesis took much of its inspiration from a study conducted by the author and Professor F.P. Lees of the Loughborough University of Technology into the hazard of transporting military explosives by road and rail.

The work contained herein relates to those substances and articles designed and manufactured so as to provide an explosion or explosive effect (i.e. largely conventional commercial and military explosives).

References

1 W.E. Baker, P.A. Cox, P.S. Westine, J.J. Kulesz and R.A. Strehlow, Explosion Hazards and Evaluation, Elsevier, Amsterdam, 1983.

2 F.P. Lees, Loss Prevention in the Process Industries, Butterworths, London, 1980.
3 G.F. Kinney, Explosives Shocks in Air, MacMillan, New York, 1962; G.F. Kinney and K.J. Graham, Explosives Shocks in Air, Springer-Verlag, New York, 1985.
4 S. Glasstone and P.J. Dolan, The Effects of Nuclear Weapons, 3rd edn., U.S. Department of Defence and U.S. Department of Energy, 1977.
5 N.F. Scilly and W.G. High, The blast effects of explosions, in: Proc. Fifth Int. Symp. on Loss Prevention and Safety Promotion, Cannes, 1986.
6 C.S. Robinson, Explosions, Their Anatomy and Destructiveness, McGraw-Hill, New York, 1944.
7 D.E. Jarrett, Derivation of the British safety distances, Ann. New York Acad. Sci. 152(1), (1968) 18–35.
8 R. Assheton, The History of Explosions, The Institute of Makers of Explosives, Wilmington, DE, 1930.
9 W.E. Baker, Explosions in Air, University of Texas Press, Austin, TX, 1973.
10 J.H. Turnbull and K. Walter, Explosions in Air and Water, Chemical Systems Group, Royal Military College of Science, Shrivenham, Wiltshire, 1982.
11 W.C. Brasie and D.W. Simpson, Guidelines for estimating damage from chemical explosions. Presented at the Symp. on Loss Prevention in the Process Industries, 63rd Natl. Meeting, St. Louis, MO, 18–21 February, 1968. Reprint 21A
12 D.R. Stull, Fundamentals of Fire and Explosion, AIChE Monograph Ser., 73 (1977) 10.
13 N.A. Eisenberg, et al., Vulnerability Model. A simulation system for assessing damage resulting from marine spills. National Technical Information Service Report AD-A015-245, Springfield, VA, 1975.
14 L.E. Fugelso, L.M. Weiner and T.H. Schiffman, Explosion effects computation aids. General American Transportation Co., Gen. American Research Division, GARD Prog. 1540 AD903279, Niles, IL, 1972.
15 V.J. Clancey, Diagnostic features of explosion damage, in: Proc. Sixth Int. Meeting of Forensic Sciences, Edinburgh, 1972.
16 C.S. White, The scope of blast and shock biology and problem areas in relating physical and biological parameters, Ann. New York Acad. Sci., 152(1) (1968) 89–102.
17 A.E. Hirsch, The tolerance of man to impact, Ann. New York Acad. Sci. 152(1) (1968) 168–171.
18 A.J. Vadala, Effects of gun explosions on the ear and hearing mechanism, Military Surgeon, 66 (1930) 710–822.
19 G.A. Henry, Blast injuries of the ear, Laryngoscope, 55 (1945) 663–672.
20 Reider (1968). (see reference 4, page 595).
21 C.M. Pietersen, Consequences of accidental release of hazardous material, J. Loss Prev. Process Ind., 3 (1990) 136–141.
22 TNO, Department of Industrial Safety, P.O. Box 342, 7300 AH Apeldoorn, The Netherlands.
23 Lovelace Foundation for Medical Education and Research, Albuquerque, NM.
24 J.G. Bowen, et al., Estimate of man's tolerance to the direct effects of air blast. DASA 2113, Lovelace Foundation for Medical Education and Research, Albuquerque, NM, 1968.
25 E.R. Fletcher and I.G. Bowen, Blast-induced translation effects. Ann. New York Acad. Sci. 152(1) (1968) 378–403.
26 F.G. Hirsch, Effects of overpressure on the ear — A review, Ann. New York Acad. Sci. 152(1) (1968) 147–162.
27 W.E. Baker and G.A. Oldham, Estimates of blowdown of quasi-static pressures in vented chambers. Edgewood Arsenal, Contractor Report EM-CR-76029, Report No. 2, 1975.
28 C.J. Clemedson, G. Hellstrom and S. Lingren, The relative tolerance of the head, thorax and abdomen to blunt trauma, Ann. New York Acad. Sci., 152(1), (1968) 187.

29 A. Longinow et al., People survivability in a direct effects environment and related topics. Project No. J6144. AD 764114. IIT Research Institute. May 1973.
30 P.L. Holden and A.B. Reeves. Fragment hazards from failures of pressurised liquefied gas vessels, in: The Assessment and Control of Major Hazards, Institute of Chemical Engineers, 1985. p. 205.
31 T.A. Zaker, Computer program for predicting casualties and damage from accidental explosions. Technical Paper No. 11, Department of Defence Explosives Safety Board, AD-A012847, May 1975.
32 T.A. Zaker. Fragment and debris hazard, Technical Paper No. 12. Department of Defence Explosives Safety Board. AD-A013634, July 1975.
33 W.G. High. Explosions: Occurrence, containment and effects. Loughborough University of Technology. Department of Chemical Engineering, Course on Loss Prevention in the Process Industries. 1976.
34 S.F. Hoerner. Fluid-Dynamic Drag. Published by the author. Midland Park, NJ, 1958.
35 B.G. Cox and G. Saville. High Pressure Safety Code. Imperial College: High Pressure Technology Association, London, 1975.
36 Safety Services Organisation. Procurement Executive, Explosives Training Course. Royal Military College of Science. Shrivenham. Wiltshire, 19–22 June, 1989.
37 J. Sperrazza and W. Kokinakis, Ballistic limits of tissue and clothing. Technical Note No. 1645. U.S. Army Ballistic Research Laboratory, RDT&E Project No. 1PO 256 01A 027. January 1967.
38 J. Sperrazza and W. Kokinakis. Ballistic limits of tissue and clothing. Ann. New York Acad. Sci. 152(1) (1968) 163–167.
39 C.S. White et al., Comparative nuclear effect of biomedical interest. CEX-58.8, Civil Effects Study. U.S. Atomic Energy Commission. January 1961.
40 G.H. Custard and J.R. Thayer. Evaluation of explosive storage safety criteria. Falcon Research and Development Company, Contract DAHC 04-69-C-0095, March 1970.
41 W. Kokinakis. A new methodology for wounding and safety criteria. Proc. of the 16th Explosives Safety Seminar, September 1974, pp. 1209–1226.
42 E.B. Ahlers, Fragment hazard study. Minutes of the 11th Explosives Safety Seminar, Memphis. TN. September 1969.
43 C.A. Geffen. Assessment of the risks of transporting propane by truck and train. Battelle Pacific Northwest Laboratory, Report PNL 3308, Richland, WA, March 1968.
44 A.H. Rausch. N.A. Eisenberg and C.J. Lynch, Continuing development of the vulnerability model — Final report. National Technical Information Service Report AD-AO-04419?. Springfield. VA. 1977.
45 J.A. Rakaczky. The suppression of thermal hazards from explosions of munitions: A literature survey. BRL Interim Memo. Report No. 377, Aberdeen Proving Ground, MD. May 1975.
46 J.B. Gayle and J.W. Bransford. Size and duration of fireballs from propellant explosions. NASA TM X-53314. George C. Marshal Space Flight Center. Huntsville. AL. August 1975.
47 R.W. High. The saturn fireball. Ann. New York Acad. Sci. 152(1) (1968) 441–451.
48 B.E. Bader. A.B. Donaldson and H.C. Hardee. Liquid-propellant rocket abort fire model, J. Spacecraft. 8(12) (1971) 1216–1219.
49 K. Hasegawa and K. Sato, Experimental investigation of the unconfined vapour-cloud explosions of hydrocarbons. Technical Memo. of Fire Research Inst., No. 12, Fire Defence Agency. Japan, 1978.
50 A.F. Roberts. Thermal radiation hazards from releases of LPG from pressurised storage. Fire Saf. J., 4 (1981/1982) 197–212.
51 D.I. Lawson and D.L. Simms. The ignition of wood by radiation. Br. J. Appl. Phys., 3 (1952) 288.
52 Miller and White. (See reference 4, p. 551).

53 K. Buettner, Effects of extreme heat on man, J. Am. Med. Assoc. 144 (1950) 732–738.
54 I. Hymes, The Physiological and Pathological Effects of Thermal Radiation. SRD R 275. Safety and Reliability Directorate, United Kingdom Atomic Energy Authority, Wigshaw Lane, Culcheth, Warrington, September 1983.
55 U.S. Department of the Army, Nuclear Handbook for Medical Service Personnel, TM-8-215. April 1969.
56 C.M. Pietersen, Analysis of the LPG-incident in San Juan Ixhuasapec, Mexico City, 19 November 1984. TNO report. TNO, Department of Industrial Safety, P.O. Box 342, 7300 AH Apeldoorn, The Netherlands, 1985.
57 Risk Analysis of Six Potentially Hazardous Industrial Objects in the Rijnmond Area, A Pilot Study. A report to the Rijnmond Public Authority, D. Reidel, Dordrecht, 1982.
58 A.M. Stoll and L.C. Greene, Relationship between pain and tissue damage due to thermal radiation. J. Appl. Physiol. 14 (1959) 373.
59 K. Buettner, Effects of extreme heat and cold on human skin. II. Surface temperature, pain and heat conductivity in experiments with radiant heat, J. Appl. Physiol., 3 (1951) 703.
60 R.M.J. Withers and F.P. Lees, The assessment of major hazards: The lethal effects of a condensed phase explosion in a built-up area. LUT, MHC/86/3., Department of Chemical Engineering, Loughborough University of Technology, Loughborough, 1986.

Journal of Hazardous Materials, 33 (1993) 35–49
Elsevier Science Publishers B.V., Amsterdam

Hazard evaluation of sulphide dust explosions

Q. Liu[a] and P.D. Katsabanis[b]

[a]*CANMET, Mining Research Laboratories, Experimental Mine, Val D'Or, Quebec J9P 4P8 (Canada)*
[b]*Department of Mining Engineering, Queen's University, Kingston, Ontario K7L 3N6 (Canada)*

(Received January 22, 1992; accepted in revised form June 22, 1992)

Abstract

Experiments were conducted in a 1 m^3 explosion chamber and the explosibility parameters for sulphide dust were determined and compared to other types of dusts. The severity of the explosions, as indicated by the K_{St} value, was scaled by comparing the experimental results from different sizes of explosion vessels. The K_{St} value was found to increase with the volume of the explosion chamber, as expected for systems whose level of turbulence increases with increasing chamber volume. Explosive limits for a typical sulphide dust were obtained by examining the effect of dust concentration on the explosibility parameters. The lower explosive limit was found to be 300 g/m^3 for a sulphide dust with a sulphur content of 29.86% by weight. To simulate the ignition source in underground mines, explosives were used to ignite sulphide dust clouds in the 1 m^3 chamber tests and an ignition criterion was developed for mining explosives that do not contain aluminum. It was found that the minimum ignition energy can be expressed as the product of the heat of explosion and the minimum weight of explosive required for the ignition of the dust.

1. Introduction

Sulphide dust explosions in underground sulphide mines have been reported frequently during the last twenty years. In most cases, dust explosions occur when blasting in massive sulphide ore bodies. The blasting operations generate a considerable amount of dust by crushing the ore immediately around the boreholes and during the fragmentation process of the friable sulphide ores. The exhausting heat and/or hot particles resulting from the detonation of the explosives used for blasting may provide enough energy to ignite the dust cloud and create a primary dust explosion. This might be followed by a secondary dust explosion in which the dust lying on the walls of the opening is dispersed by the pressure wave produced by the primary explosion and ignited

Correspondence to: Dr. Q. Liu, CANMET, Mining Research Laboratories, Experimental Mine, Val D'Or, Quebec J9P 4P8 (Canada). Fax: (819) 736-7251.

0304-3894/93/$06.00

by the flame front. The explosion could propagate long distances as long as the amount of dust to be dispersed is enough to feed the combustion process.

From the chemical point of view, a sulphide dust explosion is a rapid oxidation process of the sulphide minerals. For instance, the dust explosion of pyrite (FeS_2), which has been found to be frequently related with explosion occurrences, can be expressed by the following reaction under confined condition [1]:

$$3\,FeS_2 + 8\,O_2 \rightarrow Fe_3O_4 + 6\,SO_2 + 6.58\ \text{kJ/g of } FeS_2 \quad (1)$$

This typical reaction indicates three characteristics of a sulphide dust explosion:

(1) A large amount of heat is produced.
(2) The number of moles of gas after an explosion is less than the number before.
(3) The gaseous product (SO_2) is extremely toxic.

The first two characteristics implicate that the explosion pressure rise is caused by the temperature rise in the explosion products. The destructive force to underground facilities may be very violent in the region close to the explosion but the overpressure will decay when temperature drops. Furthermore, the generation of SO_2 gas has been one of the major problems in underground operations because the SO_2 gas must be diluted below the regulation level (2 ppm) before miners re-enter the mine.

In this paper the violence of sulphide dust explosions is compared with other dust explosions and scaling of the explosion hazard is discussed. The necessary conditions for a dust explosion are also examined in terms of dust concentration and ignition energy with explosive type of ignition sources.

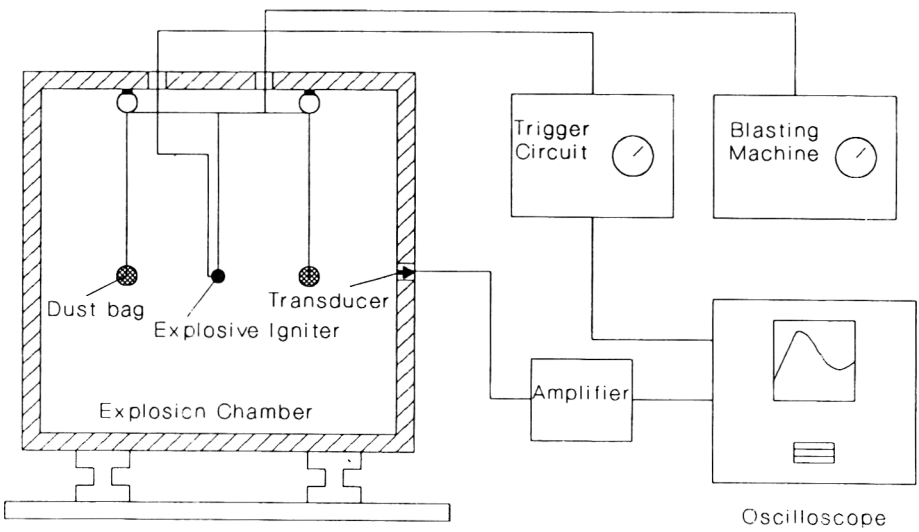

Fig. 1. Explosion monitoring system.

2. Experimental techniques

Experiments on the dust explosibility were conducted in a 1 m^3 explosion chamber. The wall of the cubic chamber is made of 12.7 mm thick steel plates and reinforced by two rows of box-beams at each side in both directions. The door can be tightly closed using 20 bolts. A rubber gasket is placed at the flange of the chamber so that no explosion products are released after the explosion.

Figure 1 illustrates the experimental arrangement. The dust is dispersed using four bags in which seismic detonators detonate instantaneously by means of a high voltage firing machine (Cordin 470). The explosive charge which is used to ignite the dust is placed at the centre of the chamber and fired with a zero delay detonator which gives an actual delay time of about 5–8 ms. By this time the dust cloud has been formed fully as observed using high speed photography. For the recording of the explosion pressure a Kistler pressure transducer (model 603B), mounted at the centre of a side wall of the chamber, is used. This is connected via a low-noise coaxial cable to an amplifier (Kistler dual mode 5004) and a Nicolet oscilloscope (model 4094). The recorded pressure history is corrected for the effect of the explosive igniter.

Two types of sulphide dust were used in the experiments; Type I and Type II. Type I is a typical sulphide dust which was provided by a Canadian sulphide mine. Its composition is 44.9% pyrite, 15.8% sphalerite, 4.8% galena, 1.1% chalcopyrite and 33.4% gangue material by weight. The sulphur content is

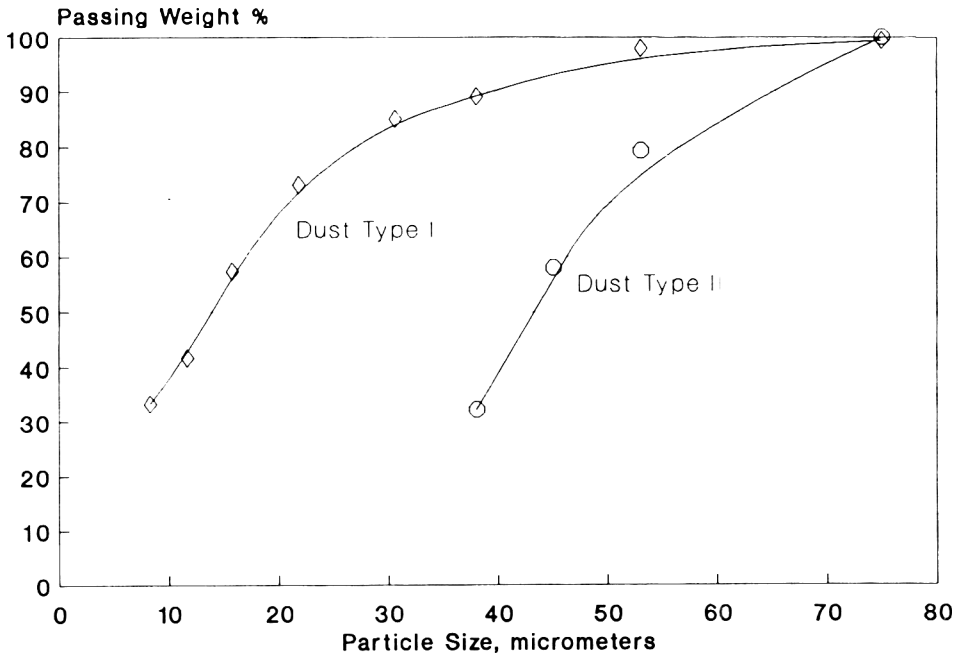

Fig. 2. Particle size distribution of the sulphide dusts used in experiments.

29.86%, the measured density of the dust particles is 3.90 g/cm^3 and the specific surface area is 1.34 m^2/g. The size distribution of the dust sample is shown in Fig. 2 while the overall mean size is 14 μm. Sulphide dust Type II was ground from a pyrite ore sample to < 75 μm (-200 mesh) and had a sulphur content of 47.9% by mass. The size distribution of the dust used in the experiment is also shown in Fig. 2. The density of the particles is 5.04 g/cm^3 and the mean size is 43 μm.

3. Relative explosion severity of sulphide dusts

Figure 3 shows typical recorded pressure histories for three dust explosions: cornstarch, wheat flour and sulphide dust Type I. Cornstarch and wheat flour were used to test the explosion chamber, as well as the recording system. Strong igniters were used to ignite the clouds: 6 g Detasheet (a military explosive consisting of pentaerythrol tetranitrate and a plastic binder) for cornstarch and wheat flour, and 15 g for the sulphide dust. The magnitude of the explosion pressure and the rate of pressure rise can be obtained directly from the recorded traces. The relative explosibility is, however, established through a classification system.

The U.S. Bureau of Mines [2] proposed a methodology for estimating industrial dust explosion hazards in terms of three probabilities: The dispersion of dust, the existence of a flammable dust concentration and the presence of an

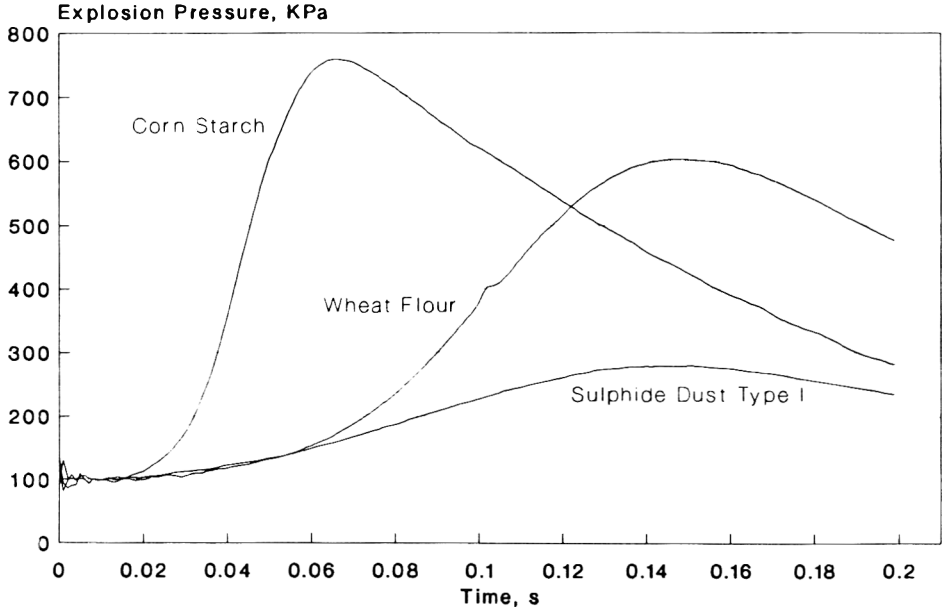

Fig. 3. Pressure–time recording of dust explosions.

effective source of ignition. This method is logical and the assessment must be done systematically in order to quantify the explosion hazard for a particular facility.

Another method which is commonly used [3], uses the K_{St} value which is obtained by the cubic relationship [3]:

$$\left(\frac{dP}{dt}\right)_{max} V^{1/3} = K_{St} \tag{2}$$

where $(dP/dt)_{max}$ is the maximum rate of pressure rise; V is the volume of explosion vessel; and K_{St} is a constant for a particular dust.

This formula indicates a fundamental observation that the maximum rate of pressure rise, which reflects the violence of a dust explosion, decreases with a larger volume of explosion vessel. For a particular dust, the K_{St} value is expected to be a constant. A four-class severity classification system has been established by grouping the K_{St} value in four ranges [3]. According to this system, St-0 class contains non-explosive dusts (K_{St} equal to 0), St-1 class contains dusts exhibiting "weak" explosion characteristics (K_{St} between 0 and 20 MPa m/s), St-2 class contains dusts exhibiting "strong" explosion characteristics (K_{St} between 20 and 30 MPa m/s), and St-3 class includes dusts exhibiting "very strong" explosion characteristics (K_{St} larger than 30 MPa m/s).

It should be noted that dust explosion hazard classification is established for designing surface facilities, e.g. relieving vents, in grain and other processing industries. The magnitude of an explosion hazard in this case is usually more severe than that of sulphide dust in underground mines. However, the rating helps to understand how violent a sulphide dust explosion is, compared to other combustible dusts. The designated parameters also help to compare the severity between different sulphide dusts.

Table 1 compares the explosibility parameters for sulphide dust Type I and Type II, as well as cornstarch and wheat flour. The data for cornstarch and

TABLE 1

Comparison of explosibility parameters obtained from 1 m^3 explosion chamber

Parameters	Cornstarch	Wheat flour	Sulphide dust Type I	Sulphide dust Type II
Dust concentration (g/m^3)	500	500	600–1000	600–1000
P_{max}(kPa)	786	603	230–302	330–370
$(dP/dt)_{max}$(MPa/s)	25.56	7.30	1.2–2.3	3.5–7.0
Time of peak pressure (ms)	66.5	147	130–170	65–93
K_{St} Value (MPa m/s)	25.6	7.3	1.2–2.3	3.5–7.0

wheat flour were directly read from the recordings of Fig. 3. For sulphide dusts Type I and Type II, because a large number of tests has been conducted, the range of typical readings is given for the major parameters. It is obvious that cornstarch and wheat flour give higher explosion pressure and rate of pressure rise than sulphide dusts. According to the dust explosion classification system based on the K_{St} values [3], sulphide dusts fall into the St-1 class. It was found that the K_{St} constant is in the range of 1.2–2.3 MPa m/s for sulphide dust Type I and in the range of 3.5–7.0 MPa m/s for sulphide dust Type II. In both cases the major sulphide mineral is pyrite. However, the concentration of pyrite is larger in sulphide dust Type II.

The major difference between cornstarch and wheat flour dusts is in the particle size. Cornstarch consists of very fine particles (mean size 22 μm) while the enriched wheat flour consists of much coarser particles (mean size 80 μm). The compositions are, however, similar. It is clearly demonstrated that the explosion pressure and the rate of pressure rise increase when the particle size is decreased. This, however, has been well established for a variety of other materials [3,13]. As far as the tested sulphide dusts are concerned, Type II dust shows higher explosibility than Type I dust. Type II dust is, however, coarser than Type I dust. Therefore the difference between the dusts, which is a result of the difference in their chemical composition would be more marked for a finer Type II dust.

From the magnitude of P_{max} and $(dP/dt)_{max}$, it is apparent that a sulphide dust explosion is less violent than the explosion of carbonaceous dusts such as cornstarch and wheat flour. Compared with other combustible dusts in underground mines, sulphide dust is also less hazardous than bituminous coal dust and higher grade oil shale dust, but it is comparable to low grade oil shale and higher volatility (7%) anthracite dusts [4]. However, for sulphide dust explosions, the additional problem is the toxic gas SO_2 that causes production delays in underground mining operations.

4. Scaling of sulphide dust explosions

In many cases when comparing the explosibility results obtained from small vessels with those from large vessels, the K_{St} value, as expressed by eq. (2) is not constant. There is a minimum volume of explosion vessel to produce a constant K_{St} value [3]. In other words, the explosibility results from small vessels may not be representative for the evaluation of the dust explosion hazard. For sulphide dusts, experiments on the explosibility have been conducted by researchers in several countries using different sizes of explosion vessels. It is certainly necessary to compare these results and scale the hazard of sulphide dust explosions. However, only few vessel sizes have been used for sulphide dusts and further, there is a lack of standardization on the methods of dust dispersion and ignition. These factors make it difficult to fully investigate the scaling of sulphide dust explosions.

Table 2 gives the explosion pressure and rate of pressure rise obtained from different explosion vessels. The listed values are the highest from the particular source. The particle sizes of these sulphide dusts are all finer than 75 μm. Since sulphide dust Type I and Type II have been used by several researchers, results are comparable. Bituminous coal dust is also listed for the purpose of comparison.

For sulphide dust Type I, it was found that the peak explosion pressure does not change significantly with the size of the explosion vessel, whereas the maximum rate of pressure rise does. It is generally true that higher $(dP/dt)_{max}$ is produced from smaller vessels. However, the K_{St} value, and subsequently the explosion hazard, is found to be smaller in small vessels. In other words, smaller vessels seem to under-estimate the explosion hazard. This is a clear indication that the K_{St} values obtained from vessels having volume smaller than 20 L, do not represent the real hazard rating for sulphide dusts. A proper interpretation and scaling is required to correlate the data for protective designs in underground facilities.

On a log–log chart, Fig. 4, the K_{St} value is plotted against the surface area to volume ratio of explosion vessels for sulphide dusts Type I and Type II. A smaller vessel has a greater surface area to volume ratio. It is obvious that the K_{St} value increases with the size of explosion vessel. The K_{St} values from a 1 m^3 vessel are the highest in the available experimental results and they

TABLE 2

Effect of vessel size on explosion parameters

Sample	Vessel size	P_{max} (MPa)	$(dP/dt)_{max}$ (MPa m/s)	Igniter	K_{St}	Reference
	1 m^3	0.30	2.3	Detasheet (15 g)	2.3	[1]
Sulphide dust Type I	20 L	0.31	2.4	C.I.[a] (5 kJ)	0.65	[5]
		0.32	4.2	C.I. (10 kJ)	1.14	[5]
		0.30	1.1	C.I.	0.3	[4]
		0.32	0.8	C.I.	0.22	[6]
	8 L	0.36	3.7	Spark	0.74	[7]
Sulphide dust Type II	1 m^3	0.37	4.69	Detasheet (15 g)	4.69	[1]
	20 L	0.40	8.3	C.I. (10 kJ)	2.25	[5]
	8 L	0.56	5.7	N.C.[b] (0.75 g)	1.14	[8]
	1 L	0.04	0.7	Spark	0.07	[2]
Bituminous coal (37% volatile)	1 m^3	0.87	10.5	C.I. (10 kJ)	10.5	[9]
	20 L	0.77	12.1	C.I. (5 kJ)	3.3	[4]
	1 L	0 72	15.9	Spark	1.59	[11]

[a]C.I. = Chemical Igniter.
[b]N.C. = Nitrocellulose.

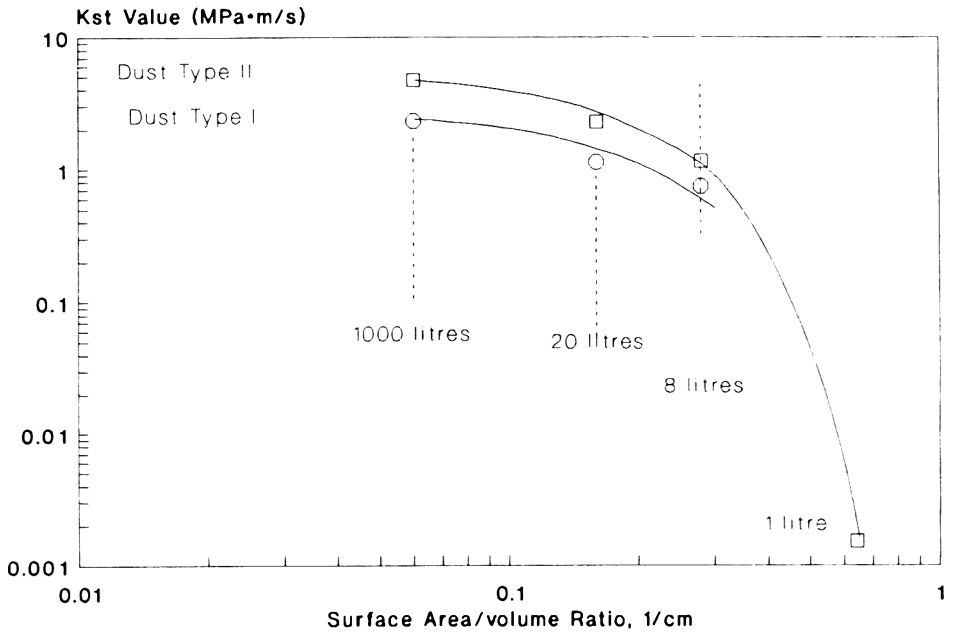

Fig. 4. Scaling of sulphide dust explosions.

seem to be close to a maximum. However, it is not certain whether the 1 m^3 chamber reaches the minimum size to generate constant K_{St} values. Further investigation is required to clarify this point although the application of K_{St} values to dust explosions in mine entries might be debatable because of the effects of turbulence [9,10].

To accurately evaluate the K_{St} value of sulphide dusts the exact same dust sample needs to be tested in different vessel sizes with the same type of ignition source. The igniter must have enough strength to enable the dust cloud to explode in different vessels. Thus the standardization of igniters seems necessary not only for explosion scaling but also for general research in this field.

Electrical sparks should no longer be used because they are not reliable when igniting a sulphide dust cloud [12]. Chemical igniters, such as the Sobbe igniters [13], could be used in small vessels as long as "overdriving" does not occur. According to the results from 20-litre and 10.3 m^3 experiments [12,14], it seems that higher strength igniters are required for larger vessels. With volume larger than 1 m^3, a chemical igniter may not be strong enough. The ignition and reaction of the chemical igniter may take a relatively long time compared to the time of the explosion pressure rise in a sulphide dust explosion. Since the ignition energy is delivered over a time period, not all of the energy in the chemical igniter contributes to the dust ignition. To examine this, 20 g black powder was used to ignite sulphide dust Type I in the 1 m^3 chamber. The explosion pressure was found to be much lower than when the

same dust was ignited by Detasheet. A large portion of non-reacted dust was found in the explosion residual. It is believed that this part of the dust had fallen on the floor before the dust explosion occurred because of the slow combustion rate of the black powder and the slow rate of energy release. It appears that explosive igniters, such as detonators and high explosives, are suitable for the ignition of sulphide dusts in large explosion vessels (e.g. $>1\ m^3$). For this reason and in order to simulate the actual ignition source in underground sulphide mines explosives were used in the present study.

Another important factor is the high specific gravity of sulphide dusts (sulphide dust is about three times heavier than carbonaceous dusts) which makes the suspension time much shorter if the same degree of turbulence is created. Thus the igniter's energy delivery time is required to be shorter meaning that faster burning igniters should be used for the heavy sulphide dusts.

In the hazard rating system (St-class) [3] based on K_{St} values, the combustible dusts encountered in the mining industry fall into the St-1 class. For example, the bituminous coal dust, which is the most reactive and energetic material among mining dusts, has a K_{St} value about 10.0 MPa m/s, while the value is lower for oil shale and sulphide dusts. Since this range, $K_{St} < 10.0$ MPa m/s, falls in the lower portion of the St-1 class, there is no apparent difference between these materials in terms of hazard classification. Furthermore most of the commonly encountered dusts fall into the St-1 class, since Bartknecht's St-0 to St-3 classification [3] covers a wide range of K_{St} values. Very few dust materials reach the St-3 class. To be able to classify the majority of dusts, particularly those encountered in the mining industry, a finer classification seems to be necessary for the K_{St} values ranging from 0 to 20.0 MPa m/s. For instance, the classification could be divided as follows:

Weak: $K_{St} = 0$–5.0 MPa m/s;

Moderate: $K_{St} = 5.0$–10.0 MPa m/s;

Strong: $K_{St} = 10.0$–20.0 MPa m/s.

In this case, most sulphide dusts fall in the weak range, whereas coal dust lies on the border line between moderate and strong. Protective measures can then be designed for each class.

5. The explosion limits

For a dust explosion to occur, the dust concentration must fall into the range between a Lower Explosion Limit (LEL) and an Upper Explosion Limit (UEL). With dust concentrations lower than LEL or higher then UEL, the dust clouds cannot explode with self-sustained flame propagation although part of the dust

(adjacent to the ignition source) might be ignited. The lower explosion limit is of practical importance in the control and prevention of dust explosions.

For sulphide dusts the LEL was found to vary with the strength of the ignition source. Figure 5 shows the result obtained when Detasheet was used to ignite the sulphide dust Type I. It follows that the lower explosion limit for the dust depends on the weight of the explosive charge used. As indicated in the figure, the minimum weight of Detasheet to ignite the dust is 6 g and the lower explosion limit is about 300 g/m^3 for sulphide dust Type I. This limit is expected to vary with the sulphur content of the sulphide dust. In general, a dust with higher sulphur content should have a lower LEL value, and vice versa.

The UEL is of limited practical interest in the case of dust explosions. For sulphide dust Type I, an explosion did not occur for a concentration of 2500 g/m^3 with 15 g Detasheet as the igniter, while an explosion did occur at a concentration of 2000 g/m^3 with the same igniter.

It is worth mentioning that between LEL and UEL, there is an optimum dust concentration below or above which the explosion pressure will decrease. The experimental results are shown in Fig. 6. For sulphide dust Type I the concentration for maximum explosibility was found to be about 1000 g/m^3. This is higher than the stoichiometric concentration. It is worth noting that with reduced dust concentration, both explosion pressure and the rate of pressure rise decrease more rapidly than with increased dust concentration.

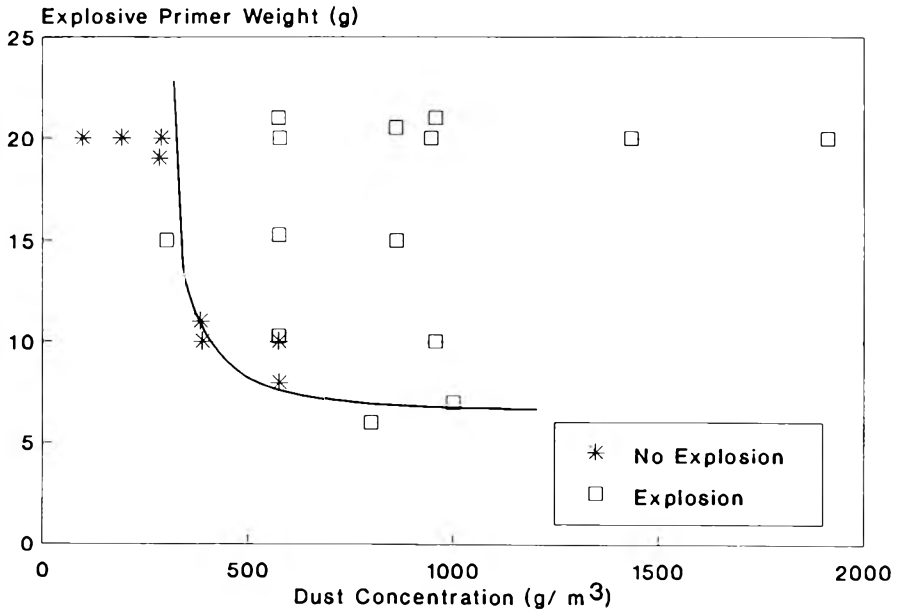

Fig. 5. Lower explosion limit and minimum igniting weight of Detasheet for sulphide dust Type I.

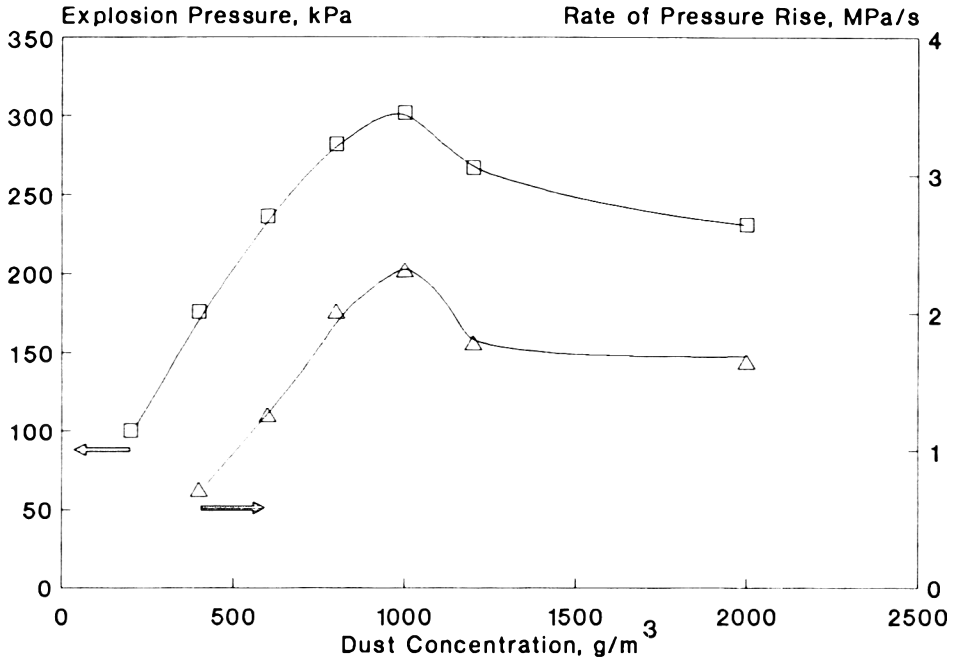

Fig. 6. Effect of dust concentration on peak explosion pressure and maximum rate of pressure rise.

6. Ignition criterion of sulphide dusts by explosives

From the investigation of the key explosives properties which influence the ignition of a sulphide dust cloud, it has been found [15] that the secondary explosion of detonation products is the dominant factor causing dust ignitions when using aluminized explosives or high explosives with very negative oxygen balances. With non-aluminized mining explosives such as ANFO (ammonium nitrate–fuel oil) and emulsion explosives, the temperature of explosion is the key factor in choosing an explosive for underground mine blasting.

A variety of explosives have been used to ignite the sulphide dust Type I at the same dust concentration (1000 g/m^3). The tests involved three ANFO explosives and four emulsions prepared on site to vary the oxygen balance level, as well as one commercial emulsion explosive and two low density emulsion explosives. The minimum weight of these explosives to ignite the sulphide dust cloud is listed in Table 3.

Table 4 provides the theoretical parameters of these explosives. The calculation was carried out by using a computer code, TIGER, which is a thermohydrodynamic computer code to calculate explosives detonation properties [16,17].

TABLE 3

Minimum explosive weight to ignite the sulphide dust cloud

Explosive	Weight (g)
ANFO #1 ($OB^a = 89.4$)	130
ANFO #2 ($OB = -17.1$)	96
ANFO #3 ($OB = -123.6$)	130
Commercial emulsion	130
Emulsion #1 ($OB = 48.4$)	158
Emulsion #2 ($OB = -4.5$)	135
Emulsion #3 ($OB = -27.2$)	130
Emulsion #4 ($OB = -102.8$)	135
Low density emulsion A ($\rho = 1.2$ g/cm^3)	150
Low density emulsion B ($\rho = 0.75$ g/cm^3)	180

[a]OB Oxygen Balance (g O_2/kg explosive).

TABLE 4

Calculated explosive parameters[a]

Explosive	ρ (g/cm^3)	OB	VOD	P_e	T_e	Q_e	E_{ign}
ANFO #1	0.85	89.4	4480	1.87	1968	2.67	348
ANFO #2	0.85	−17.1	4890	2.25	2398	3.64	350
ANFO #3	0.85	−123.6	4980	2.33	2129	3.23	420
Emulsion #1	1.0	48.4	4540	2.14	1618	2.11	334
Emulsion #2	1.0	−4.5	4810	2.45	1868	2.66	359
Emulsion #3	1.0	−27.2	4850	2.48	1810	2.57	335
Emulsion #4	1.0	−102.8	4910	2.53	1714	2.45	331
Commercial emulsion	1.15	−0.7	5510	3.55	1888	2.83	367
Low density emulsion A	1.20	10.8	5443	3.49	1678	2.42	362
Low density emulsion B	0.75	9.9	3407	0.93	1777	2.20	396

[a]Legend: OB–oxygen balance (g of oxygen per kg of explosive); VOD–velocity of detonation (m/s); P_e–explosion state pressure (GPa); T_e–explosion state temperature (K); Q_e–heat of explosion (kJ/g of explosive); and E_{ign}–minimum ignition energy of the sulphide dust cloud, kJ.

The minimum energy of ignition was calculated from the minimum weight of ignition multiplied by the heat of explosion at the thermochemical state.

It can be observed that the ignition can be explained by the explosion state temperatures for the ANFO and emulsion explosives with the exception of the low density emulsion (density equal to 0.75 g/cm^3). To ignite a sulphide dust

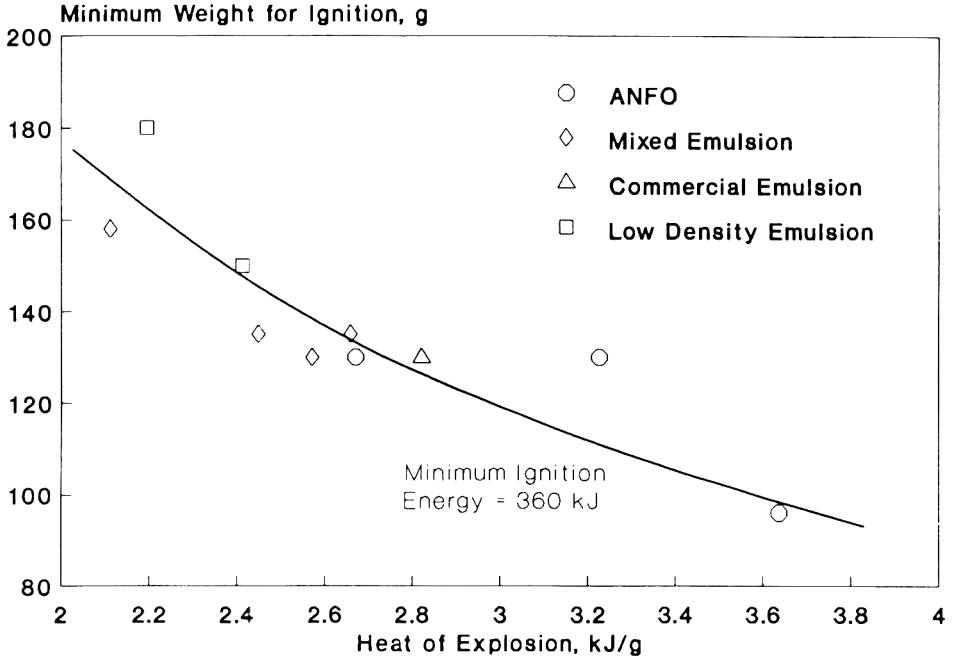

Fig. 7. Minimum ignition energy for sulphide dust Type I ignited by non-aluminized commercial explosives.

cloud, the minimum weight of explosive charge was found to decrease with the increase of explosion temperature. Without the low density emulsion, this trend agreed with the experimental results for the explosives at normal densities. However, the trend was reversed for the case of the low density emulsion explosive. Thus the minimum weight of explosive for a sulphide dust ignition cannot be explained by the explosion temperature alone.

If the minimum ignition weight is plotted versus the heat of explosion, Fig. 7, the general trend agrees well with all the non-aluminized mining explosives tested. In general, less weight is required to ignite a dust cloud with an explosive having a greater heat of explosion. This trend suggests an energy criterion for the ignition of the sulphide dust clouds. The regression line of Fig. 7 can be expressed by the following formula:

$$W_{ign} = \frac{E_{ign}}{Q_e} \tag{3}$$

where W_{ign} is the minimum ignition weight of an explosive, g; Q_e is the heat of explosion at thermo-chemical state, kJ/g; E_{ign} is the minimum ignition energy for a particular dust, e.g. $E_{ign} = 360$ kJ for the sulphide dust Type I. The deviation of the regression is 5.84% for sulphide dust Type I.

7. Conclusions

The severity of sulphide dust explosions was examined using a 1 m^3 explosion chamber and was found to be less violent than carbonaceous dusts such as wheat flour. The K_{St} value ranges from 1.2 to 2.3 MPa m/s for a sulphide dust Type I and from 3.5 to 7.0 MPa m/s for dust Type II. Scaling of the explosion hazard indicates that the K_{St} value increases with the size of explosion container, and 1 m^3 seems to be close to the minimum size which produces constant K_{St} values for sulphide dust explosions.

For sulphide dust Type I, the lower explosion limit was found to be 300 g/m^3 while the upper explosion limit was between 2000 and 2500 g/m^3. The optimum concentration is about 1000 g/m^3 which gives the maximum explosion pressure and rate of pressure rise. With non-aluminized mining explosives as the ignition source, the product of the heat of explosion of the explosive and the minimum weight of explosive for a dust ignition is approximately constant suggesting that it represents a minimum ignition energy criterion.

References

1 Q. Liu, Investigation of the Explosibility of Sulphide Dusts, Ph.D. Thesis, Department of Mining Engineering, Queen's University, Kingston, Ont., Canada, 1991.
2 M. Hertzberg, A Critique of the Dust Explosibility Index: An Alternative for Estimating Explosion Probabilities, U.S. Bureau of Mines, Report of Investigation 9095, Pittsburgh, PA, 1988.
3 W. Bartknecht, Explosions: Course, Prevention and Protection, Springer-Verlag, Berlin, 1981.
4 E.S. Weiss, K.L. Cashdollar and M.J. Sapko, Hazards of Secondary Dust Explosions in Sulfide Ore Mining, U.S. Bureau of Mines, Internal Report No. 4646, Pittsburgh, PA, 1987.
5 K.J. Mintz, Personal communication, 1991.
6 K.L. Cashdollar, M. Hertzberg and R.S. Conti, Explosion hazard of oil shale dusts: Limits, pressures, and ignitability, In: J.H. Gary (Ed.), Proc. 17th Oil Shale Symposium Proceedings, Colarodo School of Mines Press, Golden, CO, 1984.
7 R.J. Enright, Sulfide Dust Explosions in Metalliferous Mines, Proc. Australian, Inst. Min. Metall., No. 289, October, Sydney, NSW, 1984.
8 R.J. Enright, Inhibition of sulfide dust explosions with limestone, Sulphide Dust Explosion, Proc. of a workshop sponsored by Noranda Minerals Inc., GECO Div. at Manitouwadge, Ont., Oct. 1986. CANMET Report SP87-3, page II/(vii.a) 27–44.
9 W. Wiemann, Influence of temperature and pressure on the explosion characteristics of dust/air and dust/air/inert gas mixtures. In: K.L. Cashdollar and M. Hertzberg (Eds.), Industrial Dust Explosions, Proc. Symp. on Industrial Dust Explosions, Pittsburgh, PA, STP 958, ASTM, 1987.
10 P.R. Amyotte, S. Chippett and M.J. Pegg, Effects of turbulence on dust explosions, Prog. Energy Combust. Sci., 14 (1988) 293–310.
11 J. Nagy, H.G. Dorsett and A. Cooper, Explosibility of carbonaceous dusts. U.S. Bureau of Mines, Report of Investigation 6597, Pittsburgh, PA, 1965.
12 K.J. Mintz, The Explosibility of Dusts from Three Sulphide Ore Concentrates, CANMET, Mining Research Laboratories, Division Report MRL 88-54 (TR). Ottawa, Ont., 1988.

13 W. Bartknecht, Dust Explosions, Springer-Verlag, Berlin, 1989.
14 R.K. Kumer and E.W. Bowles, Large-scale Dust Explosion Experiments to Determine the Effect of Scaling on Explosion Parameters, AECL Research, Whiteshell Laboratories, Pinawa, Man., Canada, DSS FILE NO. 14SQ. 23440-8-9070, September 1990.
15 P. Katsabanis and Q. Liu, The ignition of sulphide dust cloud by explosives, Can. Min. Metall. Bull. (1992), in press.
16 M. Cowperthwaite and W.H. Zwisler, Theoretical and Mathematical Formulations for the TIGER Computer Program, Stanford Research Institute, Stanford, CA, 1973.
17 P. Katsabanis, Studies on the Numerical Modelling of Explosive Performance and Sensitivity, Ph.D thesis, Department of Mining Engineering, Queen's University at Kingston, Kingston, Ont., Canada, 1987.

Journal of Hazardous Materials, 33 (1993) 51–62
Elsevier Science Publishers B.V., Amsterdam

Supercritical water oxidation of acetic acid by potassium permanganate

Keng-Chen Chang*, Lixiong Li and Earnest F. Gloyna

Environmental and Water Resources Engineering Program, Chemical Engineering Department, The University of Texas at Austin, Austin, TX 78712 (USA)

(Received February 10, 1992; accepted in revised form May 12, 1992)

Abstract

Supercritical water oxidation (SCWO) of acetic acid by potassium permanganate ($KMnO_4$) was studied. The experiments were performed in a batch reactor at temperatures and pressures, respectively, ranging from 400 °C to 460 °C and from 275 bar to 350 bar. For comparison purposes, other oxidants, such as oxygen, hydrogen peroxide, $Cu-H_2O_2$, $Fe-H_2O_2$ and $MnSO_4-H_2O_2$, were studied. Subcritical tests with potassium permanganate were also conducted at temperatures of 250 °C, 300 °C and 350 °C. The order of acetic acid destruction effectiveness was found to be $KMnO_4 > Cu-H_2O_2 > Fe-H_2O_2 > MnSO_4-H_2O_2 > H_2O_2 > O_2$ at a temperature of 400 °C, density of 0.3 g/ml and reaction time of less than 10 min. The acetic acid destruction efficiency by potassium permanganate was 77% at a temperature of 400 °C, density of 0.3 g/ml and a reaction time of 2.5 min. Under similar conditions, only 40% of acetic acid was destroyed at 250 °C. Potassium permanganate was demonstrated to be an effective oxidant for SCWO of acetic acid.

1. Introduction

Supercritical water oxidation (SCWO) is potentially a means for hazardous waste destruction and sludge volume reduction [1–3]. When aqueous phase oxidation is carried out above the critical point of water (374.15 °C and 221.2 bar), more than 99.99% conversion of complex organic molecules to carbon dioxide and other stable entities, such as acetic acid, can be achieved within minutes [4, 5]. The rate of transformation becomes more rapid as the temperature increases. Unfortunately, at higher temperatures the materials of construction become more costly and reactor designs become more challenging. Therefore, to achieve complete organic conversion and minimize the materials problem, attention must be directed to temperature adjustment, an alternative oxidant and use of catalysts.

* Corresponding author.

0304-3894/93/$06.00

First, lower reaction temperatures ranging from 200 °C to 350 °C have been explored in wet air oxidation (WAO). WAO reportedly achieved about 85% organic conversion with a reaction time of one hour [6–8]. The incomplete oxidation products in the effluent were primarily volatile acids. In particular, acetic acid was found in the effluent from WAO of municipal and biological sludges [9–12] and WAO of phenol [13]. The transformation of acetic acid was studied in SCWO of sludges [14] and other volatile acids [4].

Second, regarding the oxidant source, oxygen and enriched air have been studied in conjunction with SCWO [1, 15, 16]. However, not until recently has hydrogen peroxide been used as the oxidant for SCWO [4, 5, 17, 18]. Although oxygen is highly favorable for use in full-scale SCWO processes, other oxidants may become attractive for specific applications. Further investigations, such as this work, are needed.

Third, catalysts have been used in WAO to

(a) enhance the conversion of complex organic compounds,
(b) shorten reaction time, and
(c) lower required reaction temperature.

Aqueous phase catalytic oxidation of organic wastewaters has been studied extensively [19–21]. More recently, the fundamental, technical, catalytic and economical aspects of WAO processes have been critically reviewed [22].

In the presence of hydrogen peroxide, copper salts were reported to be the most active catalyst [23]. The conversion of acetic acid and ammonia, respectively, increased two and eight-fold when copper(II) nitrate was added [24]. The chemical oxygen demand (COD) reduction of raw municipal wastewaters was more than doubled in a WAO reaction catalyzed by $CuSO_4$ and $Fe_2(SO_4)_3$ in conjunction with H_2O_2 [20]. The presence of catalysts can enhance the overall reaction rate as well as the distribution of by-products. For example, addition of ferric sulfate [$Fe_2(SO_4)_3$] resulted in a higher percentage of volatile acids (formic acid and acetic acid) relative to the total acid formed in the WAO of softwood and hardwood [25].

A recent study of homogeneous catalysts in SCWO showed that manganese(II) chloride, manganese(II) acetate and copper(II) tetrafluoroborate exhibited little effect on the rate of oxidation of *p*-chlorophenol in supercritical water [26]. The disadvantages of homogeneous (water-soluble) catalysts were found to be the toxicity of metal ions and subsequent post-treatment requirements. In this respect, heterogeneous (water-insoluble) catalysts could be superior because it was easier to separate them from the effluent. Heterogeneous catalysts were either metals or metal oxides, usually coated onto porous carriers. In addition, heterogeneous catalysts are generally more active as compared to homogeneous catalysts.

Mn/Ce composite oxide has been shown to exhibit higher activity than homogeneous copper(II) nitrate in the WAO of acetic acid, poly(ethylene glycol), pyridine and ammonia [24]. The rate of oxidation of *p*-chlorophenol in

supercritical water was enhanced more by increasing the surface-to-volume ratio of the reactor (Inconel 600) than by adding copper(II) tetrafluoroborate [26].

Of the precious metals, such as ruthenium, rhodium, palladium, iridium and platinum when supported by cerium(IV) oxide, ruthenium was the most active catalyst in WAO of *n*-propyl alcohol, *n*-butyl alcohol, phenol, acetamide, poly(propylene glycol) and acetic acid [27]. The catalytic activity of copper oxide and manganese oxide immobilized on a γ-Al_2O_3 carrier was studied in the WAO of phenol [19]. Of the most refractory compounds, acetic acid was catalytically oxidized by various metal salts including Co–Bi complex oxides [23] and ferric oxide [28]. Similarly, WAO of ammonia catalyzed by cerium-based composite oxides [29], and WAO of many oxygen and nitrogen-containing organic compounds catalyzed by cobalt(III) oxide [30] have been reported. These studies showed that most heterogeneous catalysts increased the rate of organic conversion.

Heterogeneous catalysts have limited applications. Heterogeneous catalysts can treat only homogeneous waste streams. The catalyst activity might be decreased as a result of contaminated catalyst surface. Therefore, the criteria for selecting a catalyst should include

(1) catalyst recovery and regeneration,
(2) catalyst poisoning,
(3) catalyst toxicity, and
(4) catalyst costs.

Potassium permanganate is a suitable candidate acting both as an effective oxidant and a possible catalyst. Potassium permanganate is a strong, water-soluble oxidant, easy to handle and readily available. Although the toxicity of potassium ion that remains in the effluent may pose a practical concern, calcium permanganate could be used since the reaction product, calcium hydroxide, is non-toxic and has limited solubility in water.

The effect of potassium permanganate on organic compounds has been well documented [31, 32]. Potassium permanganate has been used occasionally in water treatment to remove refractory organic compounds present in a concentration of a few parts per million [33–5]. Yet it should be noted that at room temperatures and atmospheric pressures potassium permanganate does not react with most organic acids [31, 32]. Potassium permanganate decomposes, upon heating, into oxygen and manganese dioxide (MnO_2). The latter has been shown to be catalytically active in WAO [19, 23, 24, 36, 37]. Manganese compounds have been used extensively as oxidizing agents for organic compounds [38]. Since manganese dioxide is water insoluble [39], it can be separated from the effluent by filtration or sedimentation.

Recently, an experimental study on catalytic SCWO was conducted [40]. The purpose of this study was to evaluate potassium permanganate as an SCWO oxidant for achieving high organic conversion at temperatures of about 400 °C. Because of the refractory nature of acetic acid, it was used to test the

effectiveness of potassium permanganate. This paper discusses the results from the experimental study.

2. Experimental procedures

Experiments were conducted in batch reactors made of 0.635 cm outside diameter and 0.0889 cm wall thickness coiled Stainless Steel 316 tubing. The internal volume of the reactor was 20 cm^3. A stoichiometric amount of potassium permanganate (8/3 [permanganate]: 1 [acetic acid] mole ratio) was used, according to eqs. (1) and (2).

$$4KMnO_4 + 2H_2O \rightarrow 4MnO_2(s) + 3O_2(g) + 4KOH \quad (1)$$

$$CH_3COOH + 2O_2 \rightarrow 2CO_2 + 2H_2O \quad (2)$$

In a typical test, an aqueous mixture of acetic acid and potassium permanganate was loaded in the batch reactor. The reactor was then submerged in a fluidized sand bath (Techne Model SBL2) which had been set at a temperature slightly above the test temperature (15 °C for 250 °C tests and 30 °C for 400 °C tests). The test temperature was monitored by a digital display (Gordon Model 5072-X-1-P-X-J-C with a readability of 1 °C). A J-type thermocouple (Omega) was in contact with the reaction fluid. The fluid pressure was monitored using a Viatran transducer (Model 3405BH3DHA20), interfaced with a Viatran digital meter (Model 2002AE). After a preset reaction time, the reactor was quenched in a water bath. A heat-up time of about 0.5 min was observed in all tests.

The test conditions included the following: five densities (0.2, 0.25, 0.3, 0.35 and 0.4 g/ml); five temperatures (250, 300, 350, 400 and 460 °C); and six reaction times (2.5, 4.5, 6.5, 10, 15 and 30 min) including the heat-up period of 0.5 min.

The acetic acid destruction efficiency was based on total organic carbon (TOC) analyses. A correlation study on acetic acid detection using TOC and gas chromatography (GC) was reported [4]. Acetic acid destruction efficiency based on TOC analyses was 5% to 10% lower than that based on GC analyses for the effluent from subcritical tests, and less than 1% for the effluent from supercritical tests. The organic by-product resulting from acetic acid destruction was likely to be formic acid, and formic acid was reportedly less stable than acetic acid even in WAO [12].

A Beckman model 915A TOC analyzer was used. The effluents were filtered using a 0.45 m membrane filter (Fisher Scientific). Following the filtration, the sample was acidified according to a ratio of 0.1 ml phosphoric acid (Fisher Scientific, 85%) to 6 ml sample. The acidified samples were then purged with nitrogen (Zero-grade) for about 10 s to strip away dissolved carbon dioxide. This procedure was verified in a blank test with a known concentration of

acetic acid. Two or three TOC injections were made for each sample, and the variations in results were less than 1%.

3. Results and discussion

The variables that were investigated in this study included density, temperature, reaction time, catalyst, oxidant and pH. Acetic acid concentration in the feed solution was 1000 mg/l for all tests. All tests were conducted with an oxidant loading of 100% stoichiometric demand, unless stated otherwise. The acetic acid destruction was related to TOC reduction. Three to six tests were made at each specified condition. The average deviations in TOC reduction were less than ±6%.

3.1 Temperature and density effects

An increase in temperature from 250 °C (subcritical) to 400 °C (supercritical) nearly doubled the destruction efficiency as shown in Table 1. However, the destruction efficiency levelled off at about 80% between 400 °C and 500 °C. To make sure this limited destruction efficiency was not due to oxidant deficiency, two parallel experiments were conducted using 50% less than and 100% more than stoichiometric requirements of potassium permanganate. A 75% destruction of acetic acid was observed when excess potassium permanganate was present. Conversely, 65% destruction resulted when insufficient potassium permanganate was used. These results suggested that temperature was the controlling factor for the destruction of acetic acid below 400 °C.

As shown in Table 2, the density change from 0.2 g/ml (subcritical) to 0.4 g/ml (supercritical) only moderately affected the destruction efficiencies at both temperatures. Table 2 also contains the results of SCWO of acetic acid by hydrogen peroxide and manganese sulfate (H_2O_2–$MnSO_4$). The destruction efficiencies of acetic acid by H_2O_2–$MnSO_4$ at 400 °C and all five densities were lower as compared to $KMnO_4$ at either 250 °C or 400 °C. The destruction efficiency obtained from H_2O_2–$MnSO_4$ (35%) was even lower than that from H_2O_2 alone (46% given in Table 3). Manganese sulfate might have played a role of scavenging hydroxyl radicals, and hence inhibiting the destruction of acetic acid under the given SCWO conditions.

TABLE 1

Effect of temperature on destruction of acetic acid by potassium permanganate

Temperature (°C)	250	300	350	400	460
Destruction (%)	40	51	66	79	75

Notes: Density = 0.3 g/ml and reaction time = 6.5 min.
Critical temperature of water = 374.15 °C and critical density of water = 0.322 g/ml [41].

TABLE 2

Subcritical and supercritical water oxidation of acetic acid by $KMnO_4$ and H_2O_2 $MnSO_4$ at different densities

Oxidant/ catalyst	Destruction efficiency (%) at density (g/ml) of				
	0.2	0.25	0.3	0.35	0.4
$KMnO_4$ (at 250 C)	24	45	40	44	39
$KMnO_4$ (at 400 C)	71	73	79	81	78
H_2O_2 $MnSO_4$ (at 400 C)	22	23	35	28	30

Notes: Run time = 6.5 min; pressures = 275–300 bar for supercritical (400 C) tests and 45–50 bar for subcritical (250 C) tests. All effluents from $KMnO_4$ tests contained some dark brown particulates. The density values for subcritical (250 C) tests only reflect different feed loadings (i.e. 4, 5, 6, 7 and 8 g of feed solution per 20 ml reactor volume), since water is in a two-phase region at this temperature.

The color of the influent and effluent was a distinguishable feature. For example, the color of the water soluble permanganate ion (MnO_4^-), was violet; the insoluble manganese dioxide (MnO_2) was a brownish-black precipitate; and the water soluble manganese acetate [$(CH_3CO_2)_2Mn$] was pale red [42]. The latter was suspected to be present in the reaction mixture. A distinguishable yellow color was observed in the effluents from most tests at densities less than or equal to 0.30 g/ml (resulting from loadings of 4, 5 and 6 g of the feed solution into 20 ml reactors), while the color of the effluents from most tests at densities greater than 0.30 g/ml (resulting from loadings of 7 and 8 g of feed solution into 20 ml reactors) was clear. These unaccounted colors may have resulted from a mixture of different manganese ions or from reactor corrosion products.

3.2 Reaction time and catalytic effects

The reaction rate experiments were performed at a density of 0.3 g/ml and a temperature of 400 °C. The destruction efficiencies given in Table 3 showed no substantial change over the observed reaction times ranging from 2.5 min to 30 min. The initial oxidation reaction was fast, but then stabilized at about 70% to 80% destruction of acetic acid.

SCWO of acetic acid by hydrogen peroxide [4] and oxygen [43] in continuous-flow reactors was evaluated. As a comparison, it was reported that 44% and 58% acetic acid conversion, respectively, with residence times of 1.8 min and 3.7 min were obtained [4]. These tests were conducted at 400 °C, 276 bar, 10% excess (stoichiometric) hydrogen peroxide, premixed in 2500 mg/l acetic acid feed solution. Wightman [43] observed a 32% acetic acid destruction using oxygen at 403 °C, 421 bar, 525 mg/l acetic acid feed concentration, oxygen pressure of 12 bar (at the feed tank), and a 34 s residence time.

TABLE 3

Destruction of acetic acid by different oxidants/catalysts

Oxidant/ catalyst	Destruction efficiency (%) at time (min) of					
	2.5	4.5	6.5	10	15	30
$KMnO_4$	77	70	79	76	83	—
H_2O_2	—	—	46	—	62	81
H_2O_2–Cu (0.1 g)	—	—	69	84	90	—
H_2O_2–Fe (0.1 g)	—	—	58	68	71	—

Notes: Temperature = 400 °C; and densities = 0.3 g/ml (H_2O_2 and $KMnO_4$) and 0.35 g/ml (H_2O_2–Cu and H_2O_2–Fe).

Table 3 also presents test results on the destruction of acetic acid by hydrogen peroxide, hydrogen peroxide plus copper (powder), and hydrogen peroxide plus iron (powder). At a reaction time of 6.5 min, the conversion rate of acetic acid was significantly influenced by the oxidant and catalyst. The destruction of acetic acid by potassium permanganate was nearly twice as high as that exhibited by hydrogen peroxide, 10% higher than that by hydrogen peroxide plus copper, and 20% higher than that by hydrogen peroxide plus iron. As the reaction time increased to 15 min, the level of acetic acid destruction by hydrogen peroxide plus copper increased 21%. Conversely, the conversion for potassium permanganate was only 4%, for hydrogen peroxide 16%, and for hydrogen peroxide plus iron 13%. The results indicated that potassium permanganate was the most effective for the shorter reaction times (less than 10 min). The fact that potassium permanganate was more effective than hydrogen peroxide in the destruction of acetic acid also suggested that oxidation could possibly be catalyzed by manganese dioxide and/or other manganese species.

The reactor inner surface was also evaluated for its catalytic effect on SCWO of acetic acid. During the course of these experiments, it was noted that the reactor surface exhibited a considerable effect on acetic acid destruction. For example, SCWO experiments were first conducted with five new reactors (Type I). Later, fifteen modified reactors (Type II) were made to reduce the dead volume at the reactor head. To test the performance of the modified reactors, experiments were re-run at 250 °C, and a comparison was made with the previous data. Surprisingly, the destruction efficiencies at all densities (except 0.2 g/ml) were drastically reduced (about 50%). However, when Type II reactors were re-used at the same conditions, the destruction efficiencies became comparable with the previous data derived from Type I reactors. It was assumed that the oxidizing nature of potassium permanganate might have caused structural and compositional changes at the inner surface of the reactor (SS 316). These changes created new surfaces and reactive sites which played

a catalytic role in the oxidation of acetic acid, permitting an increase in destruction efficiency. Such conditions did not exist in a new reactor, the oxidation was not catalyzed and, therefore, the destruction efficiency was relatively low.

Lastly, it was reported that the free permanganic acid (likely to be present at pH 3.2) was highly corrosive [34]. However, metallurgical tests performed by Technical Inspection Services, Inc. (Houston, TX), found little evidence of excessive corrosion or cracking in the SS 316 reactor after an accumulative use of 1 hour with potassium permanganate (the initial concentration = 7022 mg/l) at 400 °C.

3.3 Oxidants

In addition to the potassium permanganate experiments, hydrogen peroxide, oxygen and potassium permanganate plus oxygen were evaluated. In the potassium permanganate tests and hydrogen peroxide tests the oxidant was added in stoichiometric amounts. In the case of oxygen, excess oxidant was applied. The effect of different oxidants in conjunction with and without $KMnO_4$ on acetic acid destruction was studied at selected temperature (400 °C), density (0.30 g/ml) and reaction time (6.5 min). The results given in Table 4 showed that potassium permanganate was more effective than oxygen and hydrogen peroxide. Oxygen resulted in lower destruction levels of acetic acid as compared to hydrogen peroxide, but this difference was probably due to less effective mixing of the oxygen during the heat-up period which was about 30 s. The results implied that potassium permanganate not only provided an oxygen source but also promoted the oxidation. The combination of potassium permanganate and oxygen rendered the highest acetic acid destruction level. Without the presence of an oxidant, acetic acid remained unchanged under all test conditions.

Literature data relating to the oxidation of acetic acid indicated that potassium permanganate was effective with a short residence time (6.5 min) even at subcritical temperatures. For example, at 247 °C, 5000 mg/l acetic acid feed concentration, 10 bar oxygen pressure, and a 6.5 min reaction time, TOC reductions by both $Cu(NO_3)_2$ and Co/Bi (5/1) were less than 5%, and TOC reduction

TABLE 4

Comparison of acetic acid destruction efficiencies for potassium permanganate, hydrogen peroxide, oxygen and potassium permanganate + oxygen

Oxidant	None	Air	O_2	H_2O_2	$KMnO_4$	$KMnO_4 + O_2$
Destruction (%)	0	23	34	46	79	89

Notes: Temperature = 400 °C; density = 0.30 g/ml; run time = 6.5 min; initial oxygen pressure = 4 bar; initial air pressure = 1 bar; and both H_2O_2 and $KMnO_4$ loading = 100% stoichiometric demand.

by Mn/Ce (7/3) was about 40% [24]. Under similar conditions (except for acetic acid feed concentration = 1000 mg/l), potassium permanganate alone destroyed 40% of acetic acid. These results further suggest that oxidation of acetic acid by potassium permanganate involves relatively large rate constants. According to the power law reaction kinetics, large rate constants ensure high oxidation rates even at relatively low reactant concentrations. Based on the results provided in Table 1, the order of destruction effectiveness was found to be $KMnO_4 > Cu\text{–}H_2O_2 > Fe\text{–}H_2O_2 > MnSO_4\text{–}H_2O_2 > H_2O_2 > O_2$ at a temperature of 400 °C, a density of 0.3 g/ml and a reaction time of less than 10 min.

3.4 Effect of pH

The pH of the solution was an important factor in the oxidation of acetic acid. The oxidizing ability or catalytic effect of potassium permanganate was largely controlled by pH at the subcritical water conditions. The pH was reported to affect the decomposition of potassium permanganate [34], which in turn established the oxidation rate. The pH of feed solutions containing 1000 mg/l acetic acid was about 3.2. As given in Table 1, acetic acid destruction of 79% was achieved at 400 °C. When pH of feed solutions was adjusted with sodium phosphate to 7 and 11.5, respectively, the destruction efficiencies were 73% and 86%.

These results were in agreement with the fact that most permanganate oxidations of organic compounds are found to be catalyzed by hydroxyl ions. Furthermore, slightly acidic conditions generally stop permanganate action, while in a strong acidic medium permanganate becomes very oxidative [34].

3.5 Economic analysis

The cost-effectiveness of potassium permanganate, hydrogen peroxide and oxygen has been compared for an overall evaluation of the use of these oxidants in SCWO processes. Current market prices of the three oxidants are listed in Table 5. The effective costs have been calculated based on the cost of

TABLE 5

Cost comparison of potassium permanganate, hydrogen peroxide and oxygen

Oxidant	Cost[a] (S/kg)	Cost ($/kg O_2)	Oxidation efficiency (%)	Effective cost[b] ($/kg O_2)
$KMnO_4$	2.66	17.51	29.6	59.16
H_2O_2 (35% solution)	0.54	3.28	17.3	18.95
O_2 (Industrial grade)	1.12	1.12	1.1	101.82

[a]Prices for $KMnO_4$ and H_2O_2 were based on truck and tank load quantity (*Chemical Marketing Report*, April 20, 1992), and price for oxygen was based on cylinder quantity (Big-Three Industries, Inc.).

[b]Effective cost is defined as Cost/kg O_2 divided by the oxidation efficiency.

the actual amount of oxygen generated over the oxidation efficiency defined as,

$$\text{Oxidation efficiency } (\%) = \Delta\text{TOC(mg/l)/available } O_2 \text{ (mg/l)} \times 100 \quad (3)$$

where the values for ΔTOC have been calculated from the destruction efficiency data given in Table 4 and the values for available O_2 have been calcualted from the oxidant loading in each test.

Equations 1 and 2 were used for evaluating the oxygen equivalency of potassium permanganate. Similarly, a simplified equation for hydrogen peroxide decomposition ($H_2O_2 \rightarrow \frac{1}{2}O_2 + H_2O$) was assumed in the calculation of the cost per unit mass of oxgyen generated. Oxygen appeared to have the lowest bulk cost among these oxidants, but the effective cost for oxygen was the highest. In addition, the use of oxygen required higher capital cost because of the pressure boosting system. If the destruction efficiency of these oxidants is considered, potassium permanganate may become a practical oxidant for SCWO of organic compounds. Because of the effectiveness of potassium permanganate, this potential may become more attractive when the organic concentration is relatively low.

4. Conclusions

At SCWO conditions (400 °C and 0.3 g/ml), the destruction of acetic acid by potassium permanganate was about 80% for a residence time of 2.5 min, while at a subcritical temperature (250 °C) the acetic acid destruction efficiency was only about 40%. In all SCWO tests, the destruction efficiencies with potassium permanganate were higher than those obtained from either oxygen or hydrogen peroxide. This fact also suggests that the oxidation be promoted by manganese dioxide and other manganese species. The order of destruction effectiveness was found to be $KMnO_4 > Cu\text{–}H_2O_2 > Fe\text{–}H_2O_2 > MnSO_4\text{–}H_2O_2 > H_2O_2 > O_2$ at a temperature of 400 °C, a density of 0.3 g/ml and a reaction time of less than 10 min. Potassium permanganate is an effective SCWO oxidant and under certain conditions it may be feasible. This oxidant is particularly applicable when the organic concentration is low.

Acknowledgements

Appreciation for financial and logistical support is extended to the Separations Research Program, The University of Texas at Austin; the Gulf Coast Hazardous Substance Research Center, Beaumont, TX; and the Environmental and Water Resources Program, The University of Texas at Austin.

References

1 M. Modell, G.G. Gaudet, M. Simon, G.T. Hong and K. Biemann, Supercritical water – testing reveals new process holds promise, Solid Wastes Manag., 25(8) (1982) 26–28.
2 H. Freeman, Innovative Thermal Hazardous Organic Waste Treatment Process, Noyes Publications, Park Ridge, NJ, 1985.
3 E.F. Gloyna, L. Li and J. Bravo, Destruction of aqueous hazardous wastes in supercritical water, presented at the 2nd Int. Symposium on High Pressure Chemical Engineering, Erlangen, Germany, September 24–26, 1990.
4 E.G. Wilmanns, L. Li and E.F. Gloyna, Supercritical Water Oxidation of Volatile Acids, presented at AIChE Annual Meeting, Philadelphia, PA, August, 1989.
5 D.-S. Lee, L. Li and E.F. Gloyna, Efficiency of H_2O_2 and O_2 in supercritical water oxidation of 2,4-dichlorophenol and acetic acid, J. Supercrit. Fluids, 3 (1990) 249.
6 E. Hurwitz, W.A. Dundas, Wet oxidation of sewage sludge, J. Water Pollut. Control Fed., 32(9) (1960) 918 929.
7 G.H. Teletzke, Wet air oxidation, Chem. Eng. Prog., 60(1) (1964) 33–38.
8 E. Hurwitz, G.H. Teletzke and W.B. Gitchel, Wet air oxidation of sewage sludge, Water Sewage Works, 112(8) (1965) 298–305.
9 G.H. Teletzke, W.B. Gitchel, D.G. Diddams and C.A. Hoffman, Components of sludge and its wet air oxidation products, J. Water Pollut. Control Fed., 39(6) (1967) 994–1005.
10 Y.C. Wu, O.J. Hao, D.G. Olmstead, K.P. Hsieh and R.J. Scholze, Wet air oxidation of anaerobically digested sludges, J. Water Pollut. Control Fed., 59(1) (1987) 39–46.
11 A.A. Friedman, J.E. Smith, J. DeSantis, T. Ptak and R.C. Ganley, Characteristics of residues from wet air oxidation of anaerobic sludges, J. Water Pollut. Control Fed., 60(11) (1988) 1971–1978.
12 J.N. Foussard, H. Debellefontaine and J.B. Vailhe, Efficient elimination of organic liquid wastes: wet air oxidation, J. Environ. Eng., 115(2) (1989) 367–385.
13 M.K. Conditt and R.E. Sievers, Microanalysis of reaction products in sealed tube wet air oxidations by capillary gas chromatography, Anal. Chem., 56 (1984) 2620–2622.
14 A. Shanableh, C. Tongdhamachart, L. Li and E.F. Gloyna, Supercritical Water Oxidation of Sludges, prepared for presentation at WPCF Annual Meeting, San Francisco, CA, October, 1989.
15 T.B. Thomason and M. Modell, Supercritical water destruction of aqueous wastes, Hazard. Waste, 1(4) (1984) 453 467.
16 C.N. Staszak, K.C. Malinowski and W.R. Killilea, The pilot-scale demonstration of the NODAR oxidation process for the destruction of hazardous organic waste materials, Environ. Prog., 6(1) (1987) 39–43.
17 J.F. Welch and J.D. Siegwarth, Method for the Processing of Organic Compounds, U.S. Patent 4,861,497, August 29, 1989.
18 D.-S., Lee, Supercritical Water Oxidation of Acetamide and Acetic Acid, Ph.D. Dissertation, Civil Engineering Department, The University of Texas at Austin, 1990.
19 A. Sadana and J.R. Katzer, Catalytic oxidation of phenol in aqueous solution over copper oxide, Ind. Eng. Chem. Fundam., 13 (1974) 127–134.
20 A.K. Chowdhury and L.W. Ross, Catalytic wet oxidation of strong waste waters, AIChE Symposium Series, 71(151) (1975) 46–58.
21 J.R. Katzer, H.H. Ficke and A. Sadana, An evaluation of aqueous phase catalytic oxidation, J. Water Pollut. Control Fed., 48(5) (1976) 920–933.
22 W.H. Rulkens, A. Rinzema and F. van Voorneburg, Feasibility Study of Wet Air Oxidation Processes for Treatment of Six Selected Waste Streams, Netherlands Organization for Applied Scientific Research, TNO-Report: 88-398, 1988.
23 S. Imamura, A. Hirano and N. Kawabata, Wet oxidation of acetic acid catalyzed by Co–Bi complex oxides, Ind. Eng. Chem. Prod. Res. Dev., 21(4) (1982) 570–575.

24 S. Imamura, M. Nakamura, N. Kawabata and J. Yoshida, Wet oxidation of poly(ethylene glycol) catalyzed by Manganese-cerium composite oxide, Ind. Eng. Chem. Prod. Res. Dev., 25(1) (1986) 34–37.
25 G.D. McGinnis, W.W. Wilson, S.E. Prince and C.-C. Chem, Conversion of biomass inot chemicals with high-temperature wet oxidation, Ind. Eng. Chem. Prod. Res. Dev., 22(4) (1983) 633–636.
26 H.H. Yang and C.A. Eckert, Homogeneous catalysis in the oxidation of p-chlorophenol in supercritical water, Ind. Eng. Chem. Res., 27(11) (1988) 2009–2014.
27 S. Imamura, I. Fukuda and S. Ishida, Wet oxidation catalyzed by ruthenium supported on cerium(IV) oxides, Ind. Eng. Chem. Res., 27(4) (1988) 721–723.
28 J. Levec and J.M. Smith, Oxidation of acetic acid solutions in a trickle-bed reactor, AIChE J., 22(1) (1976) 159–168.
29 S. Imamura, A. Doi, Wet oxidation of ammonia catalyzed by cerium-based composite oxides, Ind. Eng. Chem. Prod. Res. Dev., 24(1) (1985) 75–80.
30 M.M. Ito, K. Akita and H. Inoue, Wet oxidation of oxygen- and nitrogen-containing organic compounds catalyzed by cobalt(III) oxide, Ind. Eng. Chem. Res., 28(7) (1989) 894–899.
31 R.G. Spicher and R.T. Skrinde, Effects of potassium permanganate on pure organic compounds, J. Am. Water Well Assoc., April (1965) 472–484.
32 D.G. Lee, The Oxidation of Organic Compounds by Permanganate Ion and Hexavalent Chromium, Open Court Publishing Co., La Salle, IL, 1980.
33 A.K. Cherry, Use of Potassium permanganate in water treatment, J. Am. Water Well Assoc., (1962) 417–425.
34 H.S. Posselt and A.H. Reidies, Odor abatement with potassium permanganate solutions, I&EC Prod. Res. Dev., 4(1) (1965) 48–50.
35 E.E. Hackman III, Toxic Organic Chemicals: Destruction and Waste Treatment, Noyes Data Corp., Park Ridge, NJ, 1978.
36 R.B. Wheaton, J.A. Nelson and D.E. Scherpereel, Catalyzed Wet Oxidation Process and Catalyst Useful Therein, U.S. Patent 4,460,628 (1978).
37 H.-J. Ulrich and A.T. Stone, Oxidation of chlorophenols adsorbed to manganese oxide surfaces, Environ. Sci. Technol., 23(4) (1989) 421–428.
38 D. Arndt, Manganese Compounds as Oxidizing Agents in Organic Chemistry, Open Court Publishing Co., La Salle, IL, 1981.
39 D.A. Skoog and D.M. West, Fundamentals of Analytical Chemistry 3rd edn. Holt, Rinehart and Winston, New York, NY, 1976.
40 K.C. Chang, An Evaluation of Catalyst Enhancement to Wet Air Oxidation, M.S. Report, Department of Civil Engineering, The University of Texas at Austin, May, 1990.
41 R.C. Reid, J.M. Prausnitz and B.E. Poling, The Properties of Gases and Liquids, 4th edn, McGraw-Hill, New York, NY, 1987.
42 M. Windholz, S. Budavari, R.F. Blumetti and E.S. Otterbein, The Merck Index, 10th edn., Merck & Co., Inc., Rahway, NJ, 1983.
43 T.J. Wightman, Studies in Supercritical Wet Air Oxidation, M.S. Thesis, University of California at Berkeley, 1981.
44 E. Guccione, Wet combustion of sewage sludge solves disposal problems, Chem. Eng. (1964) 118–120.

Journal of Hazardous Materials, 33 (1993) 63–73
Elsevier Science Publishers B.V., Amsterdam

Catalytic hydrodechlorination of 1,2,3-trichlorobenzene

F. Gioia, V. Famiglietti and F. Murena

Dipartimento di Ingegneria Chimica, Università di Napoli Federico II, Piazzale Tecchio, 80125 Napoli (Italy)

(Received January 3, 1992; accepted in revised form July 3, 1992)

Abstract

Detoxification by catalytic hydrotreatment can be a valid alternative to thermal incineration for the disposal of hazardous organic waste liquids. With this aim, the hydrodechlorination of 1,2,3-trichlorobenzene on a Ni–Mo/γ-Al_2O_3 catalyst has been investigated experimentally and theoretically. The behaviour of this chemical in hydrotreatment is hopefully representative of that of many toxic chlorinated compounds. The experimental reaction runs were conducted in a stirred batch reactor in the presence of hydrogen, at constant pressure ($p_{H_2} = 100$ bar), and using hexadecane as a reaction medium. The temperature, kept constant during each run, was varied in the range $200\,^{\circ}C \leqslant T \leqslant 350\,^{\circ}C$. The experimental results consisting of concentrations of reactant, reaction products and intermediates vs. time, permit the identification of the reaction network and its modification with temperature. The kinetic constants (and their temperature dependence) of the reactions which form the network are also determined.

1. Introduction

The threat posed to the environment by hazardous wastes, means there is an increasing need for research to be carried out on safe methods for their disposal. The present paper focuses on hazardous waste liquids formed mostly by organic chemicals. As discussed by Gioia [1], catalytic hydrogenation could be a possible alternative method for the disposal of such hazardous liquids. In fact, the toxic nature of most organic waste liquids is due primarily to the presence of chemical compounds containing heteroatoms (primarily Cl, N, O and S) in their chemical structure. Catalytic hydroprocessing would, therefore, be an appropriate method for detoxifying these wastes because the heteroatoms are eliminated by hydrogenolysis as HCl, NH_3, H_2O or H_2S (which are easily controlled inorganics), leaving the host compound non-toxic and frequently in a recyclable form.

Correspondence to: Prof. F. Gioia, Dipartimento di Ingegneria Chimica, Università di Napoli Federico II, Piazzale Tecchio, 80125 Napoli (Italy). Fax: (+39) (81) 611-800.

A great deal of research has been devoted to hydroprocessing. However, the most comprehensive results have been produced keeping in mind the upgrading of petroleum fractions and coal-derived liquids. Therefore, attention has been focused mostly on catalytic hydrotreatment of N-, O- and S-containing heterocycles (very refractory compounds). Naturally, the results of these investigations can also be used to design processes aimed at the detoxification of hazardous organic waste liquids containing such heteroatoms [1]. Unfortunately, however, catalytic hydrodehalogenation has not received comparable attention because the presence of chlorine-containing (or, in general, halogen-containing) chemical compounds in petroleum and in coal-derived liquids is a minor problem. Yet the presence of these compounds plays a fundamental role in the toxicity of organic waste liquids.

The problem of hydrodehalogenation has been dealt with in the literature with reference to both thermal and catalytic processes, even though to a limited extent. Louw et al. [2–4] have investigated the thermal hydrodechlorination of a variety of chlorinated compounds, both aliphatic and aromatic. These investigations provide the attainable conversion of chlorinated compounds for a given residence time and a number of temperature values. The experiments, all run in the gas-phase, show that dechlorination takes place to an appreciable extent in the temperature range 700–1000 °C. On the basis of the kinetic results, the authors speculate on the mechanism of elimination of chlorine from the host molecule.

Catalytic hydrodehalogenation, which could be more attractive due to the lower operating temperatures required, has also received some attention in the literature. Hagenmaier et al. [5] have studied the catalytic effect of copper on the decomposition (in the absence of H_2 gas) of some polychlorinated aromatics (octachlorodibenzo-*p*-dioxin (octaCDD), octachlorodibenzofuran (octaCDF), hexachlorobenzene, decachlorobiphenyl) and of some aromatics containing bromine (octabromodibenzo-*p*-dioxin, octabromodibenzofuran)). For many of these compounds the results are qualitative. Some quantitative results, though limited, are provided by Hagenmaier et al. [5] on the dechlorination of octaCDD and octaCDF. However, no information is provided on the reaction network.

Hiroaka et al. [6] have investigated the destruction of polychlorinated dibenzo-*p*-dioxins (PCDDs) in the gas phase. They provide results on the destruction (%) vs. temperature either with or without catalyst (Pt-supported). The temperatures to obtain appreciable destructions range between 700 and 900 °C without a catalyst and between 200 and 400 °C with a catalyst. No information is provided on the reaction network.

Mathé et al. [7] describe the catalytic hydrodehalogenation of a few chlorobenzenes using a Pd-supported catalyst. The reaction intermediates are identified. However, the results must be considered as qualitative inasmuch as the kinetics of the process were not analyzed. On the other hand, the results of Mathé et al. [7] cannot be used to evaluate the kinetic constants of the dechlorination reactions, inasmuch as some of the necessary operating conditions are not provided (e.g. the weight of catalyst).

Because catalytic hydroprocessing of halogenated organics seems to be particularly suited for the destruction of such compounds, an increased effort in fundamental research on this topic would be valuable. The catalytic hydroprocessing of model chlorinated compounds (the most representative ones) should be investigated in detail.

The present paper follows this line of research. The catalytic hydrodechlorination of the model compound 1,2,3-trichlorobenzene has been investigated using a commercial Ni–Mo/γ-Al_2O_3 catalyst. The study has been accomplished in the liquid phase because attention is focused on the detoxification of liquid organic wastes. The results of the present work provide an advancement over those of previous investigators inasmuch as for the first time all reaction products and intermediates have been identified and linked quantitatively in a complex network. Furthermore, the influence of temperature on the kinetic parameters of the reactions entering the network has been determined. The choice of 1,2,3-trichlorobenzene was made on the assumption that its behaviour in hydroprocessing can be considered to be representative of the upper bound of difficulty in hydrodechlorinating organic compounds. In fact, the C_6H_5–Cl bond is the strongest among the most usual organic chlorinated compounds [8].

2. Experimental procedure

The reaction was run in a batch reactor, a 300 ml autoclave with magnetic stirring (Autoclave Engineers), equipped with a sampling line of the liquid mixture and a catalyst loader (a small stainless steel cylindrical vessel) connected to the autoclave by a globe valve.

The main features of the apparatus and of the experimental procedure are as follows. A weighed amount (about 175 ml) of hexadecane (the reaction medium) is loaded into the autoclave and heating is started. At the end of the heating period, the catalyst is put into the loader together with the trichlorobenzene (the reactant) and another known amount of hexadecane (about 25 ml). Then the loader is assembled and connected to the autoclave. When the set temperature is reached the loader is pressurized, and the reactant and catalyst are injected into the autoclave by opening the globe valve. The set temperature of the heating period is about 10 °C higher than the set temperature for the run, in order to take into account the temperature drop due to loading the cool reactant and catalyst. Immediately after injection, the pressure and temperature are precisely adjusted to the desired values. This is taken as the zero time of the reaction run. During the run both pressure and temperature are kept constant.

Liquid phase samples, averaging about 1.5 ml each, were then periodically collected, with the first sample taken just before the injection operation to check for the hexadecane decomposition products. The sampling line was flushed before each sampling (line volume < flush volume $\approx$ 1.5 ml). A porous

seal at the opening of the sampling line inside the autoclave prevented loss of catalyst. Sampling frequency was adapted to the rate of trichlorobenzene disappearance. It decreased with time and increased with increasing temperature. Table 1 lists the materials used.

The samples were analyzed by GC-FID (Perkin Elmer 8500) equipped with a capillary column (crosslinked methyl silicone; 50 m long). The following chemical species were identified in the reaction samples; they are reported in order of increasing elution time: benzene (b; **5**); chlorobenzene (cb; **4**); 1,3-dichlorobenzene (1,3-dcb; **3**); 1,2-dichlorobenzene (1,2-dcb; **2**); 1,2,3-trichlorobenzene (tcb; **1**). Throughout the rest of the paper, compounds will be identified by means of either the short notation or bold face numbers, as reported in parentheses.

The experimental conditions of the reaction runs are reported in Table 2. Run 1, at 200 °C with catalyst, showed no appreciable reaction taking place, i.e. the conversion of tcb after 450 min was only 1.8%. The blank run 2 (without catalyst) at 350 °C was intended to check on the catalytic activity of the reactor walls. The results of this run showed that some reaction indeed took place, but

TABLE 1

Materials

Reaction medium	hexadecane (Aldrich Co.); vapour pressure at 350 °C ≈ 3.24 bar
Reactants	1,2,3-trichlorobenzene, 98% (Aldrich Co.); the initial concentration ranged between 1.91 and 3.13 wt% Hydrogen GC grade, 99.999% (SIO ALPHAGAZ); the total pressure was the same for all runs and equalled 100 bar; the p_{H_2} was then dependent on the hexadecane vapour pressure at the temperature of the run: i.e. $96.76 \leq p_{H_2} \leq 99.9$. We will assume $p_{H_2} \approx 100$ bar
Catalyst	HDS-9A (American Cyanamid); ground and sieved 150–200 mesh. The slurry concentration in the reactor ranged between 0.5 and 0.63 wt%

TABLE 2

Experimental conditions for the runs ($p_{H_2} = 100$ bar)

Run no.	T (°C)	W_R (g)	W_C (g)	W_L (g)	Run time (min)
1	200	3.01	0.794	157.6	450
2	350	5.00	0	159.6	450
3	350	5.01	1.060	167.3	435
4	320	5.00	0.936	159.6	450
5	290	5.05	0.896	167.4	450

its extent could be neglected in the runs with catalyst. This point will be discussed further.

Figure 1 shows the concentrations of the single compounds vs. time for the runs at the highest (350 °C) and lowest (290 °C) temperatures. All other results, i.e. at 320 °C, the blank run at 350 °C and the run at 200 °C, are given in detail in a thesis [9]. The curves in Fig. 1 are model predictions to be discussed later.

3. Kinetic equations and reaction network

Since we are dealing with heterogeneous catalytic reactions, it is natural to assume for the hydrodechlorination reactions a Langmuir–Hinshelwood-type kinetic equation. In the assumption [10, 11] that there are two different types of active site: one for the organic species and the other one for the hydrogen; the rate r'_{ij} of the reaction leading from compound i to product j can be written as:

$$r'_{ij} = k''_{ij} f(p_{H_2}) c_i / (1 + \Sigma K_i c_i) \tag{1}$$

where the functional dependence on the hydrogen partial pressure is left undetermined. In fact, since all reaction runs were accomplished at constant p_{H_2}, the product $k''_{ij} f(p_{H_2})$ is constant during each run. Therefore, eq. (1) can be written as:

$$r'_{ij} = k'_{ij} c_i / (1 + \Sigma K_i c_i) \tag{2}$$

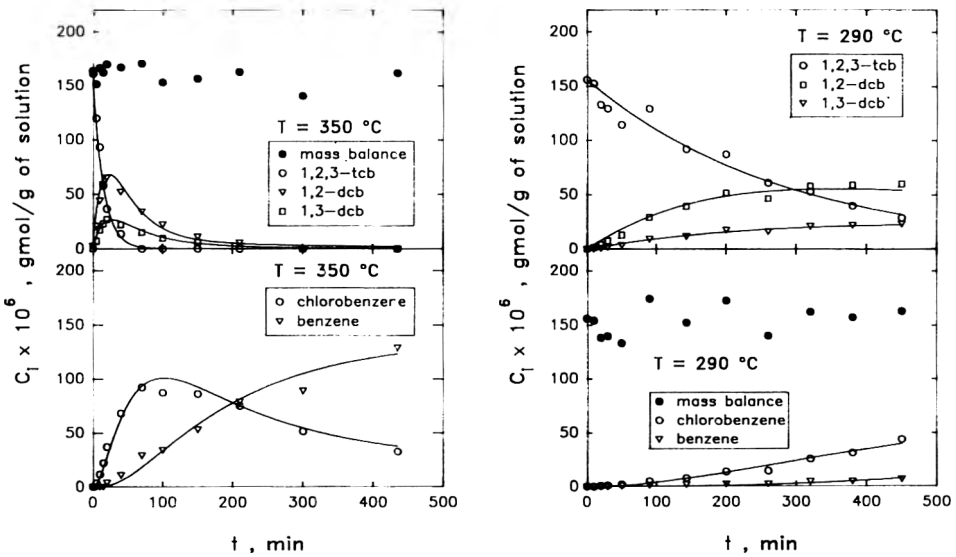

Fig. 1. Concentration of reactant, intermediates and product vs. time for two runs. Operating conditions: left panel $T = 350$ °C, $p_{H_2} = 100$ bar; right panel $T = 290$ °C, $p_{H_2} = 100$ bar. Filled symbols for checking material balance, they represent $\Sigma c_i (i = 1, 2, \ldots, 5)$ vs. time.

After a few attempts it became apparent that the adsorption of organic compounds was not relevant (i.e. $\Sigma K_i c_i \ll 1$). Thus eq. (2) reduces to:

$$r'_{ij} = k'_{ij} c_i \tag{3}$$

where $k'_{ij} = k''_{ij} f(p_{H_2})$ plays the role of a pseudo-first order kinetic constant.

The experimental data and the chemical structure of the compounds involved give clear indications on the direct reactions path. However, they are not sufficient to precisely identify the reaction network. In fact some alternatives remain.

By making use of the regression technique (HJB) proposed by Himmelblau et al. [12], which is a well-known powerful method [13] for analysing kinetic data, it was possible, by a trial and error procedure, to define the global network shown in Fig. 2 and to evaluate the kinetic constants k'_{ij} for all runs.

The procedure is as follows. A plausible network is assumed and the kinetic constants k'_{ij} of eq. (3) are evaluated by the HJB method. Then the set of differential equations describing the network is integrated by using the estimated k'_{ij}, and the resulting theoretical c_i vs. t curves are compared with the experimental c_i vs. t data. The procedure is repeated for other possible networks until that which best fits the data is identified.

The curves shown in Fig. 1 are computer-simulated based on the network of Fig. 2 and on the corresponding kinetic constants k'_{ij} as evaluated by the HJB method.

Inverse reactions have been considered in the statistical analysis of data. However, only the inclusion of the inverse reactions 5→4, 4→3 and 4→2 gave consistent results and improved the fit, but not at all temperatures. This inclusion has a theoretical support. In fact, chlorination reactions are reversible. The relative values of the equilibrium constants calculated on the basis of the data available in the literature [14] are reported in Fig. 3. It must be noted

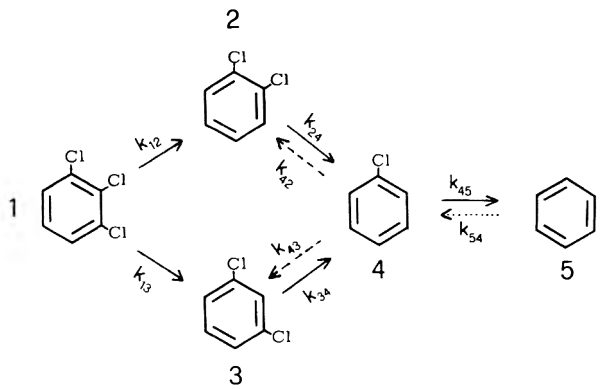

Fig. 2. Reaction network for 1,2,3-trichlorobenzene. Arrows: solid = at all temperatures; dotted = significant at 320 and 350 °C; dashed = significant at 350 °C.

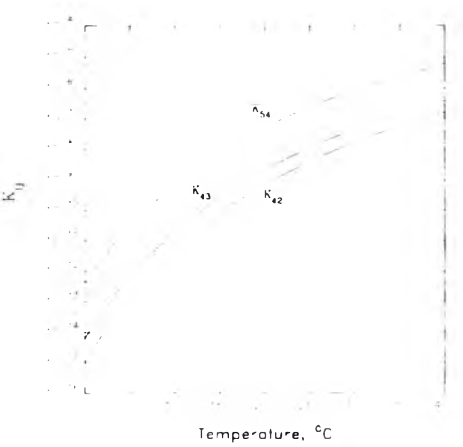

Fig. 3. Equilibrium constant K_{ij} (i and j as in Fig. 2) based on activities. Standard state: ideal gas state.

that inverse reactions, when compared to the direct ones, are favoured at higher temperatures for isothermic reactions. Reaction 5→4 which has a larger equilibrium constant is present at both $T=320$ and $T=350$ °C while reactions 4→2 and 4→3 are present only at $T=350$ °C.

The results of the analysis for the blank run (at 350 °C without catalyst) showed that the k'_{ij}s ranged between 3 and 10% of the corresponding k'_{ij} of the run at 350 °C with catalyst. The only exception was for reaction 4→5 whose constant k'_{45} without catalyst was about 40% of that with catalyst. However, at lower temperatures, due to the presumably lower activation energy of the non-catalyzed reactions, their influence will be even lower. Therefore, we will neglect the influence of the non-catalyzed reactions. Naturally less confidence will be attributed to the values of k'_{45}.

The kinetic constants k'_{ij} were reduced to the weight of catalyst by the relationship:

$$k_{ij}=(W_L/W_C)k'_{ij} \quad \text{[g of solution/g of catalyst} \cdot \text{min]} \tag{4}$$

The k_{ij} values are reported in Table 3. Not too much confidence can be given to k_{54}, which is about one order of magnitude lower than the other constants. The constants of Table 3 have been regressed according to the Arrhenius law. The calculated Arrhenius parameters are included in the last two columns of the table. For an overall picture of the behaviour of the reaction process with temperature, the Arrhenius equations for all constants are reported in Fig. 4. For further details on the kinetic analysis of data see Famiglietti [9].

Inspections of Table 3 and/or Fig. 4 indicate the following trends:

(1) For all temperatures in the investigated range, the dechlorination of chlorobenzene is the slowest step.

TABLE 3

Kinetic constants and Arrhenius parameters

k_{ij}	350 (°C)	320 (°C)	290 (°C)	k^0_{ij} (gsol/gcat · min)	ΔE_{ij} (kJ/mol)
k_{12}	7.53	1.99	0.50	8.24×10^{11}	131
k_{13}	2.70	0.59	0.14	3.54×10^{12}	145
k_{24}	3.92	1.28	0.41	6.01×10^{9}	110
k_{34}	2.77	1.11	0.11	7.39×10^{13}	159
k_{45}	0.85	0.55	0.19	1.38×10^{6}	74
k_{42}	0.15	—	—	—	—
k_{43}	0.18	—	—	—	—
k_{54}	0.03	0.17	—	—	—
k_0	1.15	0.75	0.20	2.02×10^{7}	86

k_0 is the kinetic constant of the overall reaction (5) for $n = 1$.

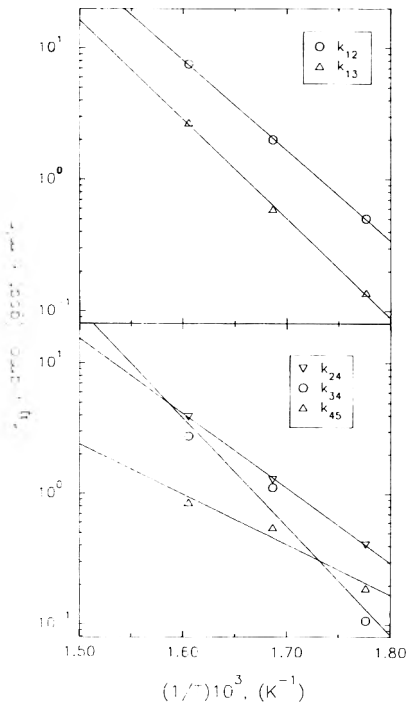

Fig. 4. Arrhenius plots for the k_{ij}s.

(2) The dechlorination path 1→2, 2→4 is preferred with respect to path 1→3, 3→4. However, the gap between the rates of the two paths tends to become smaller at higher temperatures.

These considerations allow us to draw the main conclusion that the more chlorine atoms bonded to the benzenic ring the larger is the rate of removal of a chlorine atom. Whether the chlorine atom to be removed is in the ortho or meta position plays but a minor role on the reaction rate, particularly at higher temperatures.

4. Overall dechlorination reaction

From a practical point of view it may be of interest to synthesize the dechlorination process, represented in detail by the network of Fig. 2, as:

$$\text{organic chlorine} + \tfrac{1}{2}H_2 \rightarrow \text{inorganic chlorine} \tag{5}$$

where for "organic chlorine" we mean the chlorine atom bonded to the benzenic ring, and for inorganic chlorine we mean HCl.

In Fig. 5 the weight percentage of these two forms of chlorine are reported vs. time for the run at 350 °C. The overall reaction has been regressed by the kinetic equation

$$dc_{cl}/dt = -k'_0(c_{cl})^n \tag{6}$$

where c_{cl} is the molar concentration of organic chlorine and k'_0 is the kinetic constant of the overall reaction (5).

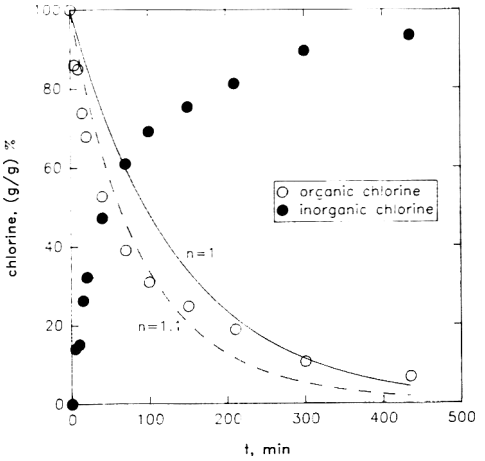

Fig. 5. Overall chlorine conversion. Operating conditions $T = 350$ °C, $p_{H_2} = 100$ bar.

The regression of data indicate that $n=1$ is a good approximation for the overall dechlorination reaction at all temperatures investigated. The corresponding values of the overall kinetic constant k'_0 (for $n=1$) have been reduced to the weight of catalyst and reported in Table 3 as k_0.

5. Conclusions

The investigation has shown that catalytic hydrogenation can be a suitable method for making waste trichlorobenzene inert, producing recyclable chemicals (i.e. benzene). At 350 °C, which is a reasonably low temperature, the conversion of the organic chlorine is more than 90% after 435 min, with only 0.63 wt% of a commercial hydrogenation catalyst.

It is worthwhile remarking that the 1,2,3-trichlorobenzene can be considered as a good model compound for predicting the kinetic behaviour of chlorinated organic compounds in general. The dechlorination rates evaluated for the trichlorobenzene can just as well be applied to other practical cases.

The overall kinetic constant k_0 could be directly and safely adopted for the design of the detoxification process of non-aromatic organic compounds containing chlorine. In fact, C_6H_5–Cl has the strongest C–Cl bond of the most usual chlorinated non-aromatic compounds [8].

For the design of the detoxification process for most toxic aromatic organic compounds with a chlorine bond to the benzene ring (e.g. PCDDs, PCDFs for which direct experimentation would be more difficult due to the high level of hazard connected with their handling), k_0 could still be adopted, but with a safety coefficient.

Notation

c_{cl}	concentration of organic chlorine (mol/g of solution)
c_i	molar concentration of compound i in liquid solution (key as in Fig. 2) (mol/g of solution)
ΔE_{ij}	activation energy of the reaction leading from organic compound i to product j in the reaction network of Fig. 2 (kJ/mol)
K_{ij}	equilibrium constant based on activities (i and j as above)
k'_{ij}	pseudo-first-order kinetic constant (i and j as above) (min^{-1})
k_{ij}	kinetic constant (i and j as above) (g of solution/(g of catalyst · min))
k^0_{ij}	pre-exponential factor (i and j as above) (g of solution/(g of catalyst · min))
k'_0	kinetic constant of the overall reaction (5) ((gsol/mol) $^{n-1}$ min^{-1})
k_0	kinetic constant of the overall reaction (5), $k_0 = k'_0(W_L/W_C)$ ($gsol^n/(mol^{n-1} \cdot gcat \cdot min)$)
n	order of overall reaction (5)
p_{H_2}	hydrogen partial pressure (bar)

R gas law constant (8.314 J/mol · K)
r'_{ij} rate of reaction (i and j as above) (mol/(g of solution · min))
T temperature (K)
W_C catalyst loaded in the reactor (g)
W_L weight of liquid solution in the reactor (g)
W_R weight of 1,2,3-tcb loaded in the reactor (g)

Acknowledgements

This work was financed by research grants from Ministero dell'Università e della Ricerca Scientifica e Tecnologica and from Consiglio Nazionale delle Ricerche.

References

1. F. Gioia, Detoxification of organic waste liquids by catalytic hydrogenation, J. Hazard. Mater., 26 (1991) 243–260.
2. R. Louw, H. Dijks and P. Mulder, Thermal hydro-dechlorination of (poly)chlorinated compounds, Chem. Ind. 19 (1983) 759–760.
3. R. Louw, M.M.G. Senden, P. Mulder and M. Tels, Thermal hydro-dechlorination of chlorinated waste, an alternative to incineration, in: K.J. Thomé-Kozmiensky (Ed.), Recycling International Industrial and Hazardous Waste, E. Freitag, Berlin, 1984, pp. 999–1005.
4. R. Louw, J.A. Manion and P. Mulder, Gas-phase thermal hydrogenolisis of organic chlorine compounds: An alternative to incineration, Resources Conservation. 14 (1987) 365–368.
5. H. Hagenmaier, H. Brunner, R. Haag and M. Kraft, Copper-catalyzed dechlorination/hydrogenation of poly-chlorinated dibenzo-*p*-dioxins, polychlorinated dibenzofurans, and other chlorinated aromatic compounds, Environ. Sci. Technol. 21 (1987) 1085–1088.
6. M. Hiroaka, N. Takeda, S. Okajima, T. Kasakura and Y. Imoto, Catalytic destruction of PCDDS in flue gas, Chemosphere, 19 (1989) 361–366.
7. T. Mathé, A. Tungler and J. Petrò, Active environment protection: Hydrodehalogenation of polychlorinated compounds, in: R. Abbou (Ed.), Hazardous Waste: Detection, Control, Treatment, Elsevier, Amsterdam, 1988, pp. 1615–1619.
8. R.C. Weast, CRC Handbook of Chemistry and Physics, CRC Press, Boca Raton, FL, 1987, p. F-184.
9. V. Famiglietti, Idrodeclorazione catalitica di 1,2,3-triclorobenzene, Chem. Eng. Thesis, University of Naples, 1991.
10. C.N. Satterfield, M. Modell and J.F. Mayer, Interactions between catalytic hydrodesulfurization of thiophene and hydrodenitrogenation of pyridine, AIChE J. 21 (1975) 1100–1107.
11. F. Gioia and V. Lee, Effect of hydrogen pressure on catalytic hydrodenitrogenation of quinoline, Ind. Eng. Chem., Proc. Des. Dev. 25 (1986) 918–925.
12. P.M. Himmelblau, C.R. Jones and K.B. Bischoff, Determination of rate constants for complex kinetic models, Ind. Eng. Chem. Fundam. 6 (1967) 539.
13. L.H. Hosten, A comparative study of short cut procedures for parameter estimation in differential equation, 12th Symp. Comput. Appl. Chem. Eng., 1 (1979) 169–183.
14. D.R. Stull, E.F. Westrum Jr and G.C. Sinke, The Chemical Thermodynamics of Organic Compounds, John Wiley, New York, NY, 1969.

Journal of Hazardous Materials, 33 (1993) 75–99
Elsevier Science Publishers B.V., Amsterdam

Forced, angled plumes

G.F. Lane-Serff[a], P.F. Linden[b] and M. Hillel[b]

[a] *Department of Oceanography, Highfield, Southampton SO9 5NH (UK)*
[b] *Department of Applied Mathematics and Theoretical Physics, Silver Street, Cambridge CB3 9EW (UK)*

(Received November 15, 1991; accepted in revised form July 3, 1992)

Abstract

In this paper a simple mathematical model is used to describe the curved, turbulent plume formed by injecting a constant flux of buoyant fluid into a stationary, unstratified ambient at an angle to the vertical. The main assumptions are the entrainment assumption: the entrainment into the turbulent plume is at a rate proportional to the local mean along-plume velocity, and the Boussinesq approximation: the density difference between the plume and the ambient is relatively small. A unified theory is presented which allows practical predictions to be made of plume trajectories and concentrations without recourse to complex turbulent modelling. It is found that *all* such plumes can be traced back to a virtual origin, and that the *shape* of the plume depends only on the angle of the plume to the vertical at the virtual origin. Various properties of the plume such as mean velocity, radius and density are predicted as functions of distance along the plume. Angled plumes made in laboratory experiments are described and compared with the theoretical predictions. The applications and limitations of the theoretical model are discussed.

1. Introduction

Forced, angled plumes occur in a variety of situations, wherever relatively dense or light fluid is injected at an angle into a large body of fluid. Thus this flow occurs both naturally and due to the action of man; for example in magma chambers, flows into lakes and seas (especially where the outflow is below the surface), sewage outfalls, ventilation systems, accidental leaks of gases and other hazardous materials and vehicle exhausts. In such flows the plume of relatively light (or dense) fluid will be turbulent and ambient fluid will be mixed into the plume by turbulent eddies. This paper describes a simple theoretical model of these forced, angled plumes which shows how all such plumes can be traced back to a virtual origin. Furthermore, the model shows that the shape of the plume depends only on the angle of the plume to the vertical at the virtual origin.

Correspondence to: Dr. P.F. Linden, Department of Applied Mathematics and Theoretical Physics, Silver Street, Cambridge CB3 9EW (UK).

The nature of plumes rising from sources of buoyancy and momentum has been discussed and described by many authors. Morton et al. [1] set out an analysis of a source of buoyancy, and Morton [2, 3] extended this to allow for a source of buoyancy, mass and momentum. Morton only considered the case where momentum is in the vertical direction and of the same sign as the buoyancy forces: the so called "forced plume". Germeles [4] considered the case of momentum at an angle to the vertical but his analysis breaks down for horizontal plumes. Numerical schemes for evaluating forced, angled plumes from a given set of initial conditions have been described by Schatzmann [5] and Hofer and Hutter [6]. This paper sets out a more general, though simple, analysis of maintained, forced, angled plumes in an unstratified and stationary ambient fluid, with the results given in a form of practical use.

In order to describe this process a simple "entrainment assumption" is made, first proposed by Taylor [7]. The analysis in this paper is based on this assumption and the development of it by Morton et al. [1] and Morton [2, 3]. If the flow is fully turbulent (i.e. independent of Reynolds number) then the flow of ambient fluid into the plume may be described in terms of the relative velocity of the plume to the ambient fluid. The entrainment assumption states that the rate of transfer of ambient fluid into the plume, characterised by an inflow speed of ambient fluid perpendicular to the plume axis, is *proportional* to the mean centre-line speed of the plume (see Fig. 1). The (constant) ratio of inflow speed to plume speed will be denoted by α.

It is known that, for a vertical plume, properties such as time-averaged velocity and density difference follow a Gaussian distribution across the plume (see List [8], for a review), but it is adequate to assume a "top-hat" profile for such quantities, i.e. a uniform value across the plume and zero outside the plume. In fact, provided it is assumed that the profiles are similar at all positions along the plume, the analysis is not substantially altered by this assumption [2, 3]. The length-scale over which the density difference profile spreads is known to be larger than that over which the velocity profile spreads. We will use λ to denote the ratio of transverse length scales of density and velocity, and take it to be 1.1 based on the results of the experiments mentioned above.

In vertical plumes in unstratified surroundings the entrainment assumption is equivalent to assuming that the plumes are self-similar [9]. We will take $\alpha = 0.1$ from the results obtained by many experimenters [10–12]. The nature of the entrainment, and thus the value of α, may vary between different parts of the flow depending on the relative importance of buoyancy and momentum, but we will ignore such variations since the dominant effect in this problem is the change in entrainment due to the variations in the plume speed at different points on the plume. Thus we are using a somewhat approximate, representative value of α. We will discuss variations in α in more detail in the concluding section. We will also assume that fluxes due to variations from the mean flow ("turbulent transports") are insignificant compared with the mean fluxes.

We will assume, further, that the density difference between the plume and the ambient fluid is relatively small (the Boussinesq approximation) and that

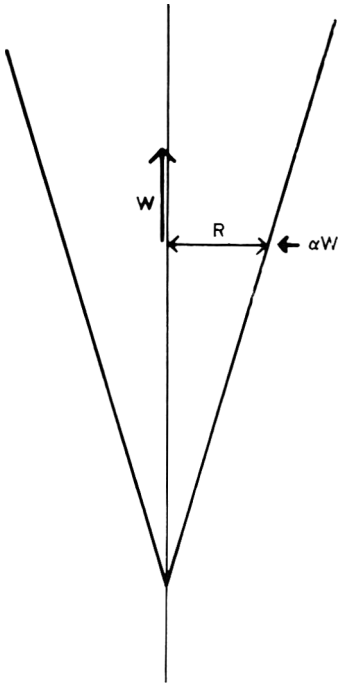

Fig. 1. Idealised view of a vertical plume, with mean centre-line speed W and radius R. The plume entrains ambient fluid characterised by a mean entrainment velocity proportional to the centre-line speed.

the fluid is incompressible. The Boussinesq approximation is not a serious restriction in practice since many of the applications involve relatively small density differences. Also the density difference decreases rapidly away from the source, due to entrainment, and so even when this approximation is not valid near the source it will be valid some distance (usually small) from the source.

The case of forced vertical plumes is re-analysed in Section 2. We develop a new classification and show that vertical plumes fall into three classes depending on the direction of the momentum flux at the virtual origin. The model for angled, forced plumes is given in Section 3 and solutions of the equations for a comprehensive range of source conditions is given in Section 4. These solutions are discussed in Section 5. Experiments on laboratory plumes are described and compared with the model in Sections 6 and 7, and the conclusions of the work are given in Section 8.

2. Vertical forced plumes

We begin with the case of vertical forced plumes in uniform surroundings. Although this has been discussed before (see, for example, Ref. [9], chapter 6)

the results will be presented in a new way which clarifies the division of vertical plumes into three basic categories, namely *buoyant jets*, *mass-sources* and *pure plumes*. This analysis also leads more naturally into the case of plumes directed at other angles, which will be discussed in the later sections. Under the assumptions detailed above, and taking top-hat profiles, the equations of conservation of momentum, mass and buoyancy are, respectively,

$$\begin{aligned} &\mathrm{d}(W^2R^2)/\mathrm{d}Z = g'(\lambda R)^2, \\ &\mathrm{d}(WR^2)/\mathrm{d}Z = 2R\alpha W, \\ &\mathrm{d}(g'WR^2)/\mathrm{d}Z = 0. \end{aligned} \tag{1}$$

Here W is the plume speed, R the plume radius, Z the vertical position and $g' = g\Delta\rho/\rho$ is the reduced gravitational acceleration. We will take g' to be positive and Z to increase along the direction of the buoyancy force, so that Z increases upward for buoyant plumes and downward for negatively buoyant plumes.

It is useful to define

$$\begin{aligned} &F = g'WR^2, \\ &K = WR^2, \\ &P = W^2R^2. \end{aligned} \tag{2}$$

The quantities F, K and P are proportional to the fluxes of buoyancy, mass and momentum, respectively. It can be seen immediately from eq. (1) that the buoyancy flux is conserved along the plume and thus

$$F = F_S, \text{ constant}, \tag{3}$$

and F_S is taken here to be positive.

Equations (1) will be non-dimensionalised by the following transformations (using lower-case to denote non-dimensional quantities):

$$\begin{aligned} &p = P/P_S, \\ &k = (\lambda/(2\alpha)^{1/2})F_S^{1/2}P_S^{-5/4}K, \\ &z = ((2\alpha)^{1/2}\lambda)F_S^{1/2}P_S^{-3/4}Z, \\ &r = (z/Z)R, \end{aligned} \tag{4}$$

where F_S and P_S are the values of F and P at the source (the subscript S will refer to conditions at the source throughout this analysis). Substitution of (4) into (1) and (3) leads to

$$\begin{aligned} &pp' = k, \\ &k' = |p|^{1/2}, \end{aligned} \tag{5a}$$

where the primes indicate differentiation with respect to z (except for g'). The initial conditions are

$$p = 1 \quad \text{and} \quad k = k_S = (\lambda/(2\alpha)^{1/2})F_S^{1/2}P_S^{-5/4}K_S. \tag{5b}$$

Integration of (5a) and applying the initial conditions (5b) gives

$$(\tfrac{4}{5})(|p|^{5/2}-1)=k^2-k_S^2. \tag{6}$$

Curves of p against k are plotted in Fig. 2. At the source $p=1$, and from (1a) it can be seen that the momentum flux increases with distance from the source and this is represented on Fig. 2 by the region $p>1$. In the region $p<1$ the solution has been integrated back to a "virtual origin" where the mass flux, k, and hence the plume radius are both zero. The momentum flux, p, is not, in general, zero at the virtual origin and the sign of p at $k=0$ determines the nature of the plume. From (6) it can be seen that the momentum flux at $k=0$ is positive (negative) when the mass flux k_S at the source is less (greater) than the critical value $k_C=2/\sqrt{5}$.

For small values of the mass flux $k_S<k_C$, the momentum and buoyancy fluxes at the virtual origin are in the same direction, and we will refer to this case as the *buoyant jet*. The virtual origin lies behind the source and the initial spread from the source is large. At large distances from the source the solution (for k tending to infinity) asymptotes to that of a pure plume. A sketch of this case is shown in Fig. 3a.

When $k_S=k_C$, the mass and momentum fluxes at the virtual origin are zero and the flow is that of a *pure plume*. In this case the properties of the plume can be derived directly from (5a) with the initial condition $p=0$ at $k=0$. The solution is well known; for the purposes of this analysis it is sufficient to note that the plume is conical with the half-angle at the vertex being $\tan^{-1}(6\alpha/5)$ as shown in Fig. 3b.

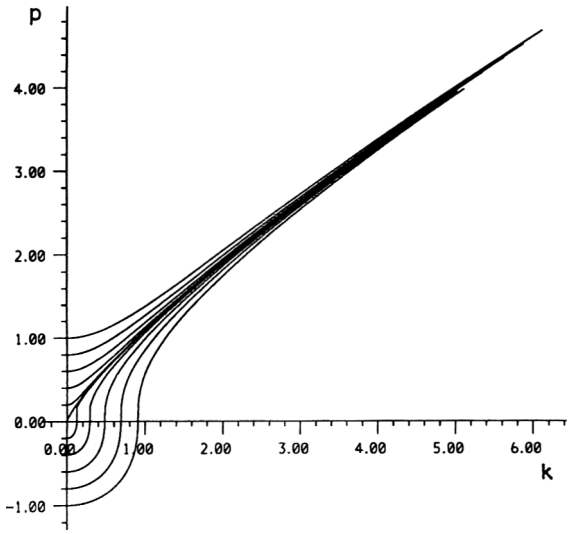

Fig. 2. Momentum and mass fluxes for vertical plumes (non-dimensionalised with respect to the buoyancy and momentum fluxes at the source). The source initial conditions are $p=1$ and $k=k_S$; the solutions have been integrated back to the 'virtual origin' where $k=0$ (and thus the radius equals zero).

For larger values of k_S, so that $k_S > k_C$, $p < 0$ at the virtual origin. In this case the momentum flux at the virtual origin has the opposite sign to the buoyancy flux, and the virtual origin may be in front of the source. At these high values of the source mass flux the plume behaves as though it initially flows backward from the virtual origin, spreading with the same angle as for a jet, its momentum being decelerated by the buoyancy forces until it stops at some point behind the source. It is then accelerated forwards through the source with the required mass and momentum fluxes. This situation is sketched in Fig. 3c and we shall refer to this flow as a *mass source*. It should be emphasised that the

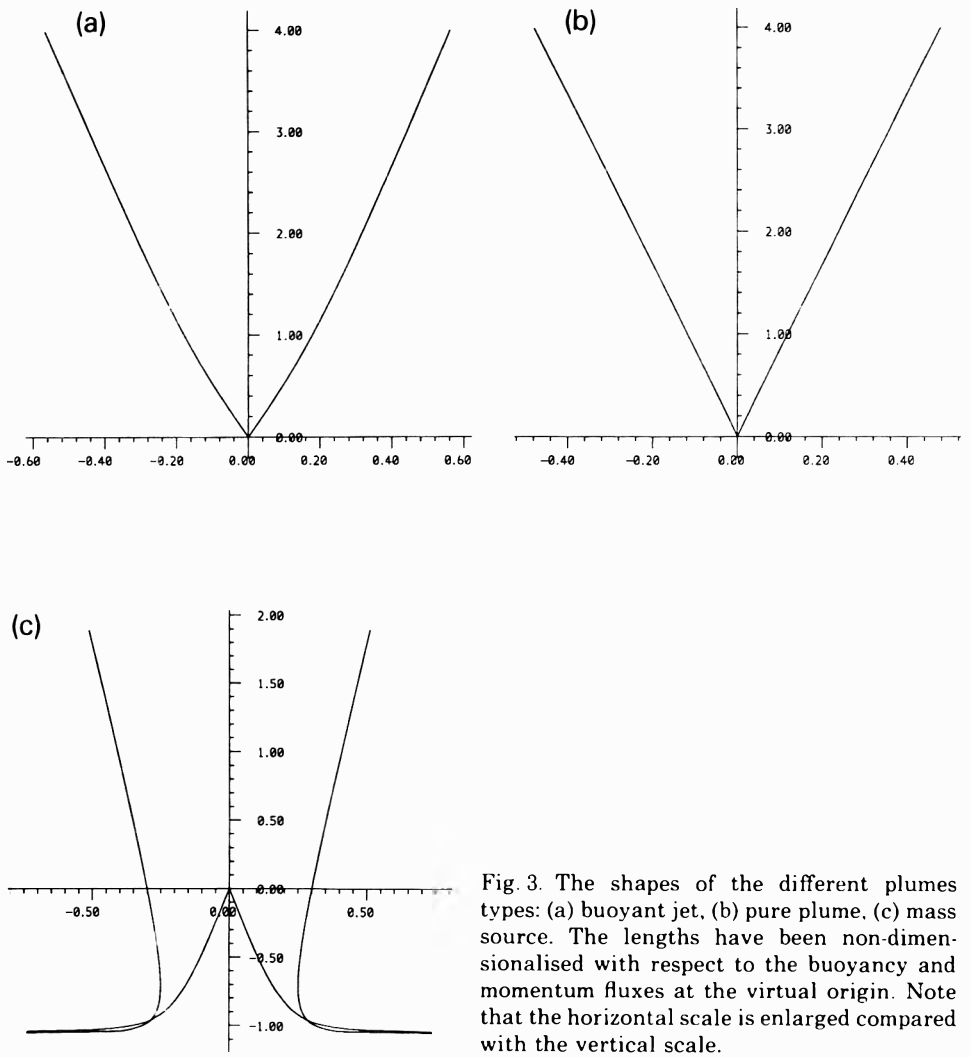

Fig. 3. The shapes of the different plumes types: (a) buoyant jet, (b) pure plume, (c) mass source. The lengths have been non-dimensionalised with respect to the buoyancy and momentum fluxes at the virtual origin. Note that the horizontal scale is enlarged compared with the vertical scale.

region $p<0$ in Fig. 2 is unphysical. We have not considered the case where the momentum and buoyancy fluxes *at the source* have opposite signs. This model does not allow for the plume overlapping itself, nor does it allow for the entrainment of other than ambient fluid. The real source may be anywhere on the upward flowing part of the shape in Fig. 3c, in particular the flow may contract above the source before widening again. Note that the source diameter is never much less than 0.4, in non-dimensional units, and so the plume shape is very close to a buoyant plume only a few diameters from the source. For this reason the mass-source type flow is generally regarded as an unimportant case for vertical plumes, but we include it for completeness and for comparison with downward pointing angled plumes for which the downward flowing part is a physical solution since the plume would then entrain ambient fluid.

It is convenient to non-dimensionalise the equations of motion with respect to the momentum flux at the virtual origin, P_0, rather than that at the source. We will denote this new set of non-dimensional quantities by the subscript 1, i.e.

$$
\begin{aligned}
&p_1 = P/P_0,\\
&k_1 = (\lambda/(2\alpha)^{1/2}) F_S^{1/2} P_0^{-5/4} K,\\
&z_1 = ((2\alpha)^{1/2}\lambda) F_S^{1/2} P_0^{-3/4} Z,\\
&r_1 = (z_1/Z) R, \quad \text{and so } k_{1S} = (\lambda/(2\alpha)^{1/2}) F_S^{1/2} P_0^{-5/4} K_S.
\end{aligned}
\tag{7}
$$

With this non-dimensionalisation the curves in Fig. 2 are reduced to the three curves shown in Fig. 4. Instead of the source conditions being represented by the point where $p=1$ and $k=k_S$ on Fig. 2, they are represented on Fig. 4 by the point where $p_1=p_{1S}=P_S/P_0$ and $k_1=k_{1S}$. This will be on the curve marked "buoyant jet" if $k_S<k_C$: all curves above the pure plume curve are mapped onto the jet-curve. Whereas it will be on the curve marked "mass-source" if $k_S>k_C$: all curves below the pure plume curve are mapped onto the mass-source curve (see Fig. 5). The shape of the plume thus depends only on whether k_S is greater or less than k_C. The size of the plume is determined by the length scale

$$L_v = (1/(2\alpha)^{1/2}\lambda) F_S^{-1/2} P_0^{3/4}, \tag{8}$$

where $P_0 = |1-\frac{5}{4}k_S^2|^{2/5} P_S$ (with k_S defined in eq. 5b).

Note that as k_S approaches k_C, from either direction, the length scale tends to zero, and hence the extent of the region where the plume shape differs significantly from that of the pure plume also tends to zero and the non-dimensional distance of the actual source from the virtual origin tends to infinity. In Fig. 6, p_1 and k_1 are plotted against z_1, and thus the position of the actual source in Fig. 3 can be found as the value of z_1 for which $k_1=k_{1S}$. The part of the mass-source curves where z_1 is decreasing as p_1 and k_1 increase is not physical, it represents a downward flowing plume entraining ambient fluid.

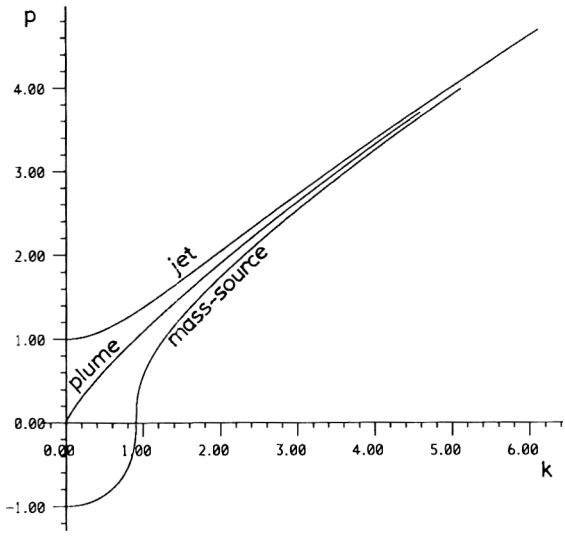

Fig. 4. Momentum and mass fluxes non-dimensionalised with respect to the buoyancy and momentum fluxes at the virtual origin. The family of solutions in Fig. 2 is reduced to just three here.

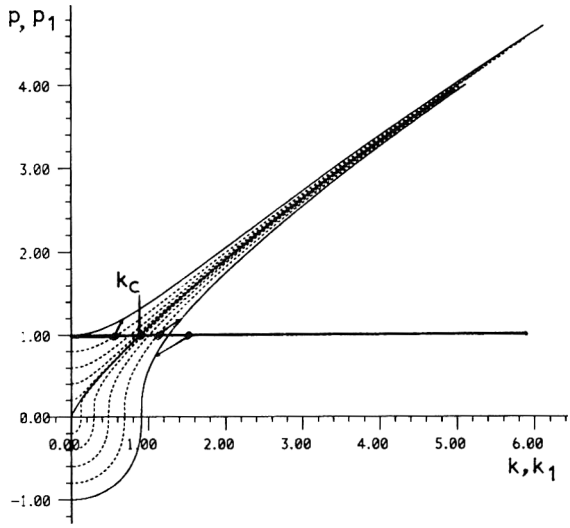

Fig. 5. The non-dimensionalisation from $p=1$, $k=k_S$, to $p_1=p_{1S}$, $k_1=k_{1S}$. All solutions in the 'jet region' are mapped to the buoyant jet curve, whilst those in the 'mass source region' are mapped to the mass source curve.

For the case of a pure plume, the distance Z_V from the source to the virtual origin is related to the source radius, R_S, by

$$R_S=(6\alpha/5)Z_V,$$

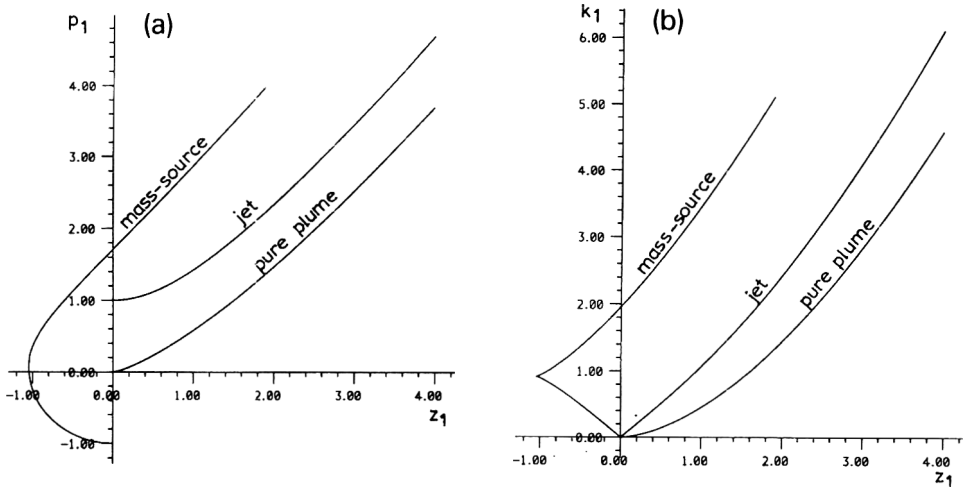

Fig. 6. Momentum and mass fluxes as functions of height for the three plume types. (All quantities non-dimensionalised with respect to the buoyancy and momentum fluxes at the virtual origin.)

since, as mentioned above, the pure plume is straight sided. Consequently R is given by

$$R=(Z+Z_V)R_S/Z_V.$$

Recall that Z is the distance above the actual source, and thus the results familiar from similarity solutions of buoyant axisymmetric plumes are recovered,

$$\begin{aligned} W&=W_S(R_S/R)^{1/3}=W_S(Z_V/(Z+Z_V))^{1/3},\\ \Delta\rho&=\rho g'/g=\Delta\rho_S(R_S/R)^{5/3}=\Delta\rho_S(Z_V/(Z+Z_V))^{5/3}. \end{aligned} \tag{9}$$

For the other plume types such quantities can be calculated from the values of p_1 and k_1 given in Fig. 6,

$$\begin{aligned} \Delta\rho&=\rho g'/g=\Delta\rho_S k_{1S}/k_1,\\ R&=R_S(k_1/k_{1S})(p_{1S}/p_1)^{1/2},\\ W&=W_S(k_{1S}/k_1)(p_1/p_{1S}), \end{aligned} \tag{10}$$

In order to understand the nature of the changing length scales and shapes, consider a source of buoyant fluid with a fixed total flow rate but a variable exit size. This fixes buoyancy and mass fluxes, but if the exit radius is reduced the efflux velocity and thus the momentum flux must increase. Starting with a large exit radius, P_S will be small and k_S will be large. On changing scales to p_1 and k_1 it can be seen that p_{1S} is small and k_{1S} is greater than k_C. The source will have the shape shown in Fig. 3 for a "mass source", with a large length

scale ($L_V = (5^{3/10}/2)(K_S^3/4\lambda^2\alpha^4 F_S)^{1/5}$, from eq. 8) and with the source position close to $z_1 = 0$. In practice the entrainment assumption is likely to be inaccurate near such a source as the plume will not be fully turbulent there. This will result in a more pinched shape than that shown in Fig. 3c.

As the exit radius is reduced so P_S increases. The shape of the plume will remain the same but the length scale L_V will decrease, and so the plume will tend to the straight-sided buoyant plume shape closer to the source. Also z_{1S} will increase, so the actual position of the source will be higher on the mass source shape (Fig. 3c). As the radius is reduced further, k_S approaches k_C, and p_{1S}, k_{1S} and z_{1S} tend to infinity, the length scale L_V tends to zero and the shape will be that of a straight-sided pure plume (Fig. 3b). Reducing the radius still further, k_S becomes less than k_C, and p_{1S}, k_{1S} and z_{1S} are still large and the shape is still close to that of the buoyant plume. Now, however, the plume follows the "buoyant jet" shape (Fig. 3a) with the plume spreading at an angle which decreases with height rather than increases as for the mass source shape (compare Figs. 3a and 3c). As the exit radius is further reduced k_S tends to zero, P_0 tends to P_S, the length scale, L_V, behaves like $P_S^{3/4}$, k_{1S} tends to k_S and z_{1S} tends to zero (to the apex of the jet shape) giving an initial spreading angle of $\tan^{-1}(2\alpha)$.

3. The model for forced, angled plumes

Now consider forced plumes where the initial momentum flux is not purely vertical but is at an angle to the vertical. Again the entrainment assumption is applied by stating that the inflow speed into the plume is proportional to the speed along the centre-line of the plume. Ignoring the curvature of the plume the "top-hat" equations become (for flow in an unstratified medium)

$$\begin{aligned} &\textit{Momentum} \\ &\quad \text{vertical} && \mathrm{d}(WVR^2)/\mathrm{d}S = g'(\lambda R)^2, \\ &\quad \text{horizontal} && \mathrm{d}(UVR^2)/\mathrm{d}S = 0, \\ &\textit{Mass} && \mathrm{d}(VR^2)/\mathrm{d}S = 2R\alpha V, \\ &\textit{Density} && \mathrm{d}(g'VR^2)/\mathrm{d}S = 0. \end{aligned} \tag{11}$$

In this case U and W are the horizontal and vertical components of the centre-line velocity, $V = (U^2 + W^2)^{1/2}$, R is the radius of the plume and S is the distance along the plume centre-line (see Fig. 7). As before $g' = g\Delta\rho/\rho$ is the reduced gravity. The inclination of the plume to the horizontal, θ, is given (for any point on the plume centre-line) by $\tan\theta = W/U$.

It is useful to define

$$F = g'VR^2, \qquad Q = VR^2, \qquad M = V^2R^2, \qquad H = UVR^2, \tag{12}$$

which are proportional to the total buoyancy, mass and momentum fluxes and the horizontal momentum flux, respectively (compare with eq. 2).

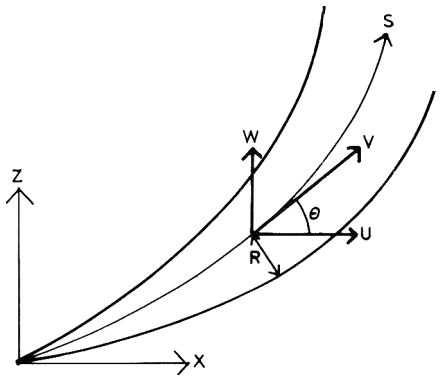

Fig. 7. An idealised view of an angled plume. Compare this with Fig. 1.

From (11) it can immediately be seen that the horizontal momentum flux, H_0, and the buoyancy flux, F_0, are conserved along the plume,

$$F_0 = g' VR^2, \quad \text{constant},$$
$$H_0 = UVR^2, \quad \text{constant}. \tag{13}$$

These conserved quantities are used to define non-dimensional variables (in this case there is no need to integrate back to the virtual origin to find a meaningful scale for the momentum flux, unlike the vertical plume described above)

$$m = M/H_0, \qquad q = (\lambda/(2\alpha)^{1/2}) H_0^{-5/4} F_0^{1/2} Q,$$
$$s = S/L_A, \qquad r = R/L_A, \qquad x = X/L_A, \qquad z = Z/L_A, \tag{14}$$

where the length-scale is given by $L_A = (\lambda\sqrt{\alpha})^{-1} H_0^{3/4} F_0^{-1/2}$. The remaining plume equations (11) then reduce to the pair of equations

$$m((m^2-1)^{1/2})' = q,$$
$$q' = (m)^{1/2}, \tag{15}$$

where the primes now represent differentiation with respect to s, i.e. along the plume axis (except again for g').

This form of the equations breaks down as θ tends to $\pm\pi/2$. In this limit, $m \gg 1$ and the equations become

$$mm' = q,$$
$$q' = (m)^{1/2}, \tag{16}$$

which are the equations for a vertical plume given in eq. (5a) above.

Otherwise, however, by substituting $t \equiv (m^2-1)^{1/2} = \tan\theta$, the equations can be written

$$t' = q/(t^2+1)^{1/2},$$
$$q' = (t^2+1)^{1/4}, \tag{17a}$$

This is the final form of the equations used in this model. The initial conditions are

$$t_S = \tan\theta_S, \qquad q_S = (\lambda/(2\alpha)^{1/2}) F_0^{1/2} H_0^{-5/4} Q_S, \tag{17b}$$

where the dimensionless mass flux is obtained from (14).

4. Solutions for forced, angled plumes

Equations (17a) were integrated numerically, using various initial values of the inclination θ and setting q initially to zero. All plumes can be traced back to a virtual origin where q, the mass flux, is zero. Hereafter the subscript 0 will refer to conditions at the virtual origin, the subscript S to those at the actual source of a plume. (Note that $F_0 = F_S$ and $H_0 = H_S$ since these quantities are conserved throughout the plume.)

The trajectory of the plume centre-line can be determined from

$$x' = \cos\theta \qquad \text{and} \qquad z' = \sin\theta. \tag{18}$$

All other plume properties can be recovered from q and θ:

$$\Delta\rho = \rho g'/g = \Delta\rho_S q_S/q,$$
$$M = H_0/\cos\theta,$$
$$R = R_S(q/q_S)(\cos\theta/\cos\theta_S)^{1/2}, \tag{19}$$
$$V = V_S(q_S/q)(\cos\theta_S/\cos\theta).$$

Figure 8 shows the values of q and θ along plumes for various values of θ_0 at $q=0$. For any given real plume, q_S can be calculated from (17b), which, rearranged, gives

$$q_S = (\lambda/(2\alpha)^{1/2})(g'R/V)^{1/2}(\cos\theta_S)^{-5/4}. \tag{20}$$

The centre-lines of plumes with different angles at the virtual origin are plotted in Fig. 9. The values of plume length s measured from the virtual origin are given on both Fig. 8 and 9 to facilitate identification between them. The position on Fig. 9 is determined by the value of s and virtual origin angle, θ_0, found from Fig. 8. For example: if, for a given real plume, $q_S = 2.5$ and $\theta_S = 10°$ at the source then it can be seen (from Fig. 8) that this is equivalent to a position part way along a plume whose initial conditions were $q=0$ and $\theta = -60°$, at a distance 2.0 (measured along the plume axis) from the source. This is at

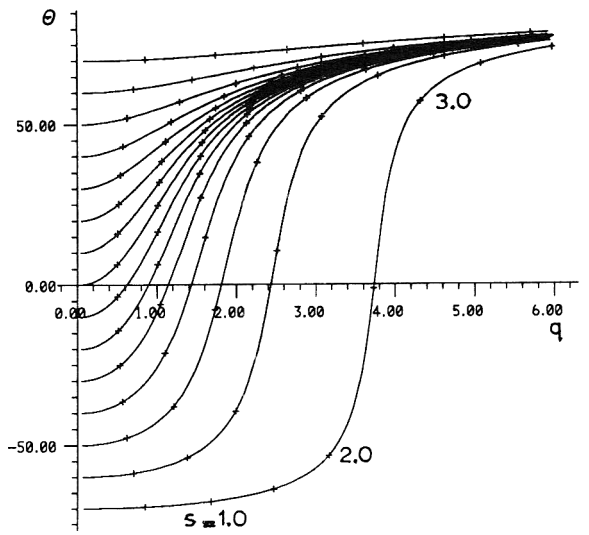

Fig. 8. Non-dimensionalised mass flux as a function of plume angle for various values of the plume angle at the virtual origin. The solutions have been marked at points corresponding to regular intervals measured along the plume centre-line to ease identification between this figure and the next.

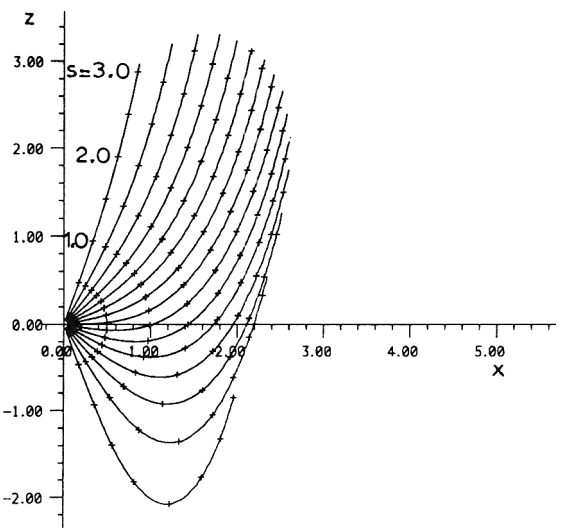

Fig. 9. Shapes of the centre-lines of angled plumes with the same range of initial angles as for Fig. 8. The marks on each solution are at regular intervals measured along the plume centre-line.

$x=1.3$, $z=-1.4$ on Fig. 9, the centre-line of the real plume is then given by following the curve through $(1.3, -1.4)$ for higher values of s. The *shape* of a plume depends only on its angle at its virtual origin, though its overall *size* varies, depending on the length scale defined in (14).

The shape of the boundaries of plumes with various values of θ_0 are shown in Fig. 10, though note the warnings given below in interpreting these figures. It is sometimes useful to know the lowest point reached by a buoyant plume which has a downward component of momentum flux at the source. This can be estimated by dimensional analysis: see, for example, Fischer et al. [11]. A length-scale can be made from the buoyancy flux and the vertical component of the momentum flux, $(M_0 \sin \theta_0)^{3/4} F_0^{-1/2}$, and it has been proposed that this length-scale multiplied by a universal constant will give the lowest point of the plume. Figure 11 shows the relationship between the lowest point, z_M, measured from the virtual origin, and the value of θ_0. Since this distance is measured from the virtual origin this figure is most useful where the actual source is close to the virtual origin, i.e. when q_S is small. Note that in Fig. 11 the lengths are non-dimensionalised with respect to the buoyancy flux and the *total* momentum flux at the virtual origin, rather than the *horizontal* momentum flux, so Fig. 11 gives the relationship between the lowest point and θ_0 for a given total momentum flux at the virtual origin. The total momentum flux at the virtual origin, proportional to M_0, is related to the (constant) horizontal momentum flux and thence the total momentum flux at the source by

$$M_0 \cos \theta_0 = H_0 = H_S = M_S \cos \theta_S. \tag{21}$$

It can be seen that the relationship between z_M and θ_0 given in Fig. 11 is a nearly linear one and it is significantly different from a curve of the form $(\sin \theta_0)^{3/4}$ given by the dimensional analysis described above. Also plotted on Fig. 11 are the results of laboratory experiments, described below. The larger error bars at larger angles to the horizontal are due to features of the flow: large eddies develop and though the boundary (of interest) of the plume is well defined at any instant its position is subject to large fluctuations.

For such plumes it is also useful to know where the plume returns to its original level (its "range") and its concentration there. In general it is necessary to evaluate the behaviour of the plume from its initial conditions using Figs. 8 and 9 and eq. (19). If q_S is small, however, the actual source is close to the virtual origin and θ_S is close to θ_0. Thus the range is (approximately) the value of x where the plume returns to $z = 0$. Again, to make clear the dependence on θ_0, we will non-dimensionalise the mass flux and lengths with respect to the total momentum flux, M_0, so that

$$q_1 = (\lambda/(2\alpha)^{1/2}) M_0^{-5/4} F_0^{1/2} Q, \tag{22}$$

and the new length-scale is given by $L_1 = (\lambda\sqrt{\alpha})^{-1} M_0^{3/4} F_0^{-1/2}$.

Figure 12 shows the range, both to the nearest point on the plume at $z = 0$, denoted by x_{1B}, and the distance to the centre-line at $z = 0$, denoted by x_{1C}, as it depends on θ_0. Figure 13 shows $1/q_1$ at these positions, which is proportional to concentration (see eq. 19), though note that the model assumes a top-hat form of the concentration profile and this needs to be considered when evaluating the value at the near boundary, x_{1B}.

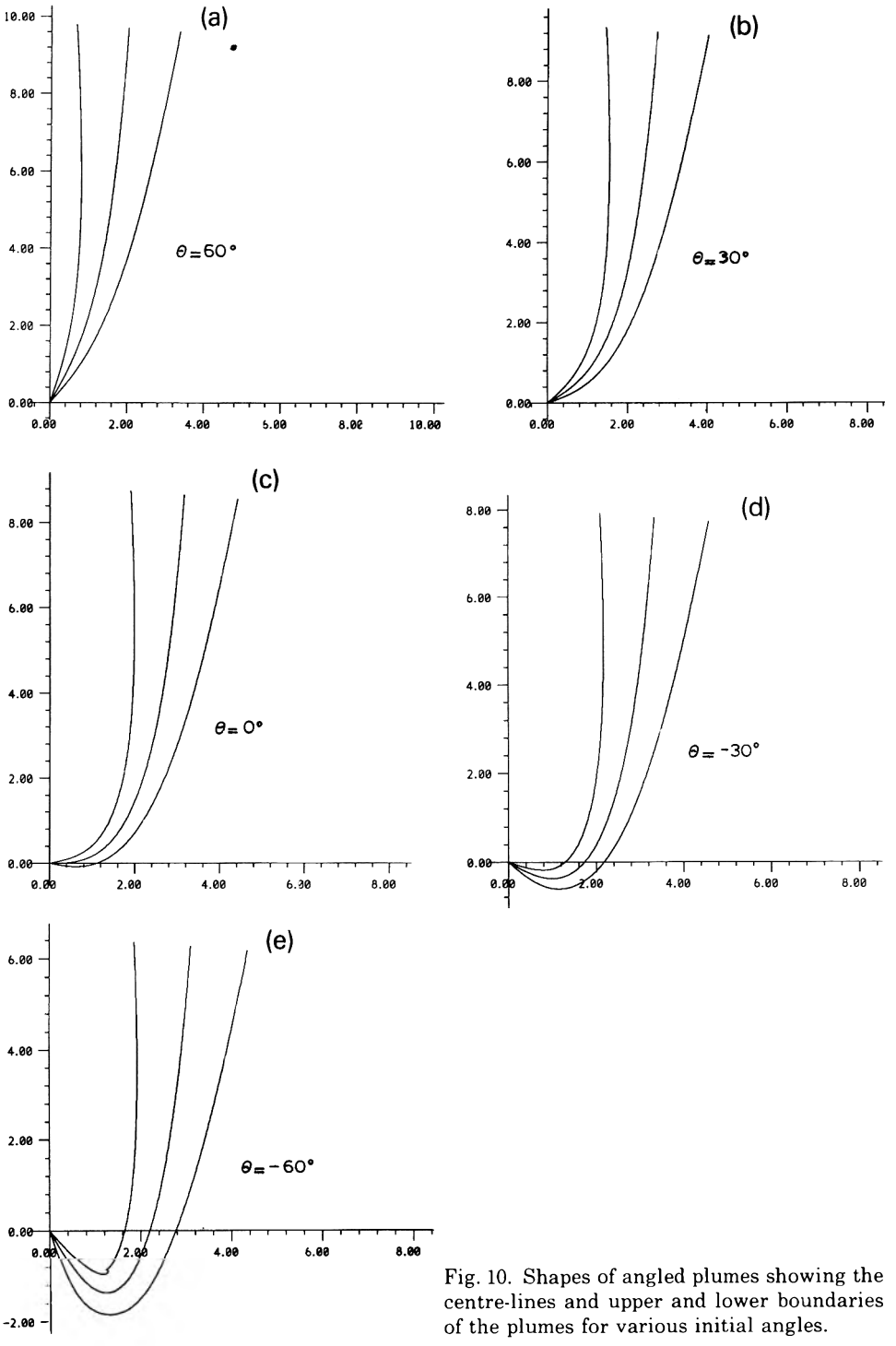

Fig. 10. Shapes of angled plumes showing the centre-lines and upper and lower boundaries of the plumes for various initial angles.

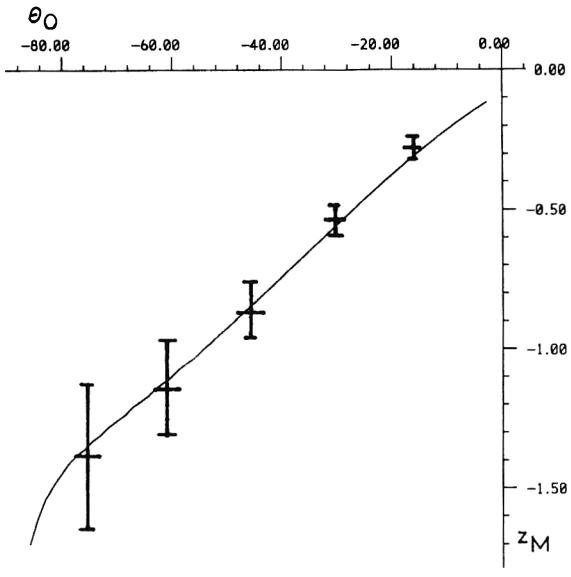

Fig. 11. Theoretical and experimental results showing the maximum depth that the lower boundary of a downward angled plume reaches. The lengths have been non-dimensionalised with respect to the total momentum flux (rather than the horizontal momentum flux) at the virtual origin. The error bars reflect the uncertainties in the maximum depth due to fluctuations of the turbulent plume.

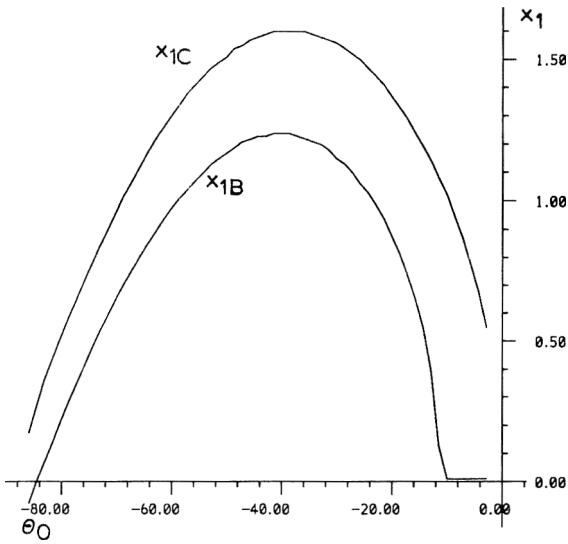

Fig. 12. The distance from the virtual origin to the point on a downward angled plume where it returns to its initial height, with x_{1B} the distance to the upper boundary, and x_{1C} the distance to the centre-line.

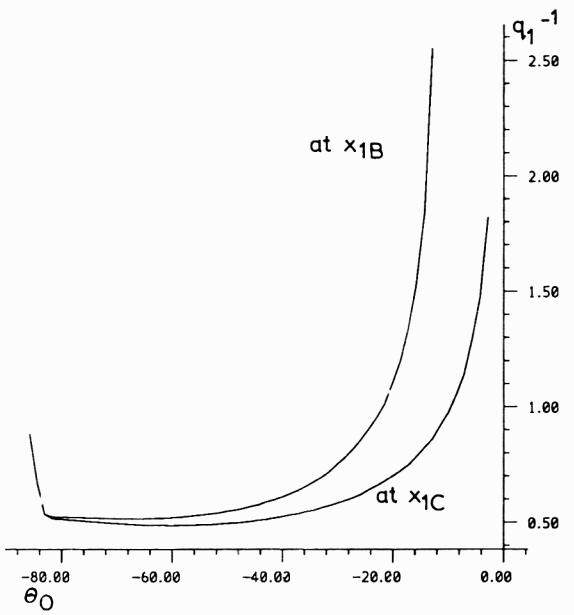

Fig. 13. The value of $1/q_1$ at the point where a downward angled plume returns to its initial height. This is a measure of the concentration at that point (see text).

5. Discussion of the theoretical results

Figure 14 shows the radius and speed of the plume as a function of position along the plume centre-line for $\theta_0 = +45°, 0°, -45°$. The results for $\theta_0 = +45°$ are similar to those for a vertical plume with, initially, a momentum jet behaviour tending to a buoyant plume shape as in Fig. 3, but with the centre-line following a curved trajectory. For $\theta_0 = 0°$ (a horizontal jet) the results are again similar but here the transition from momentum jet, with spreading angle $\tan^{-1}(2\alpha)$, to buoyant plume, with angle $\tan^{-1}(6\alpha/5)$, is somewhat sharper.

For negative θ_0, however, a different phenomenon is apparent. The vertical component of the velocity is initially negative and increases through zero as the plume turns. Thus the total plume speed is decelerated more than in the previous cases and the plume radius increases more than for a momentum jet. The plume is then accelerated (the speed of the plume has a minimum in this case as distinct from the previous cases where the plume speed decreases monotonically) and the plume radius increases more slowly than for the buoyant plume. In fact, for sufficiently steep negative angles the plume radius actually decreases. The shape is similar to the "mass source" in Fig. 3. On physical grounds the momentum jet-like behaviour can only be exhibited where the plume momentum flux has a (positive) component in the direction of

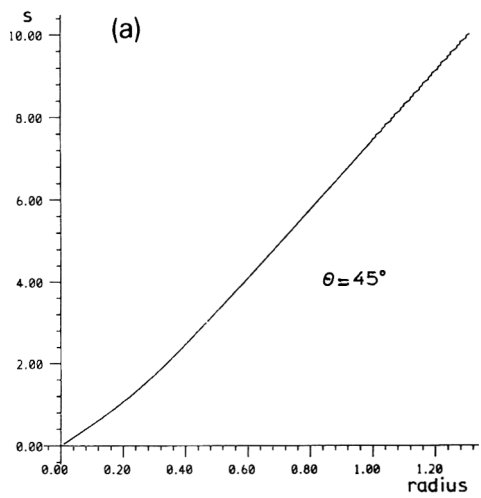
(a)
s
10.00
8.00
6.00
4.00
2.00
0.00
θ=45°
0.00 0.20 0.40 0.60 0.80 1.00 1.20
radius

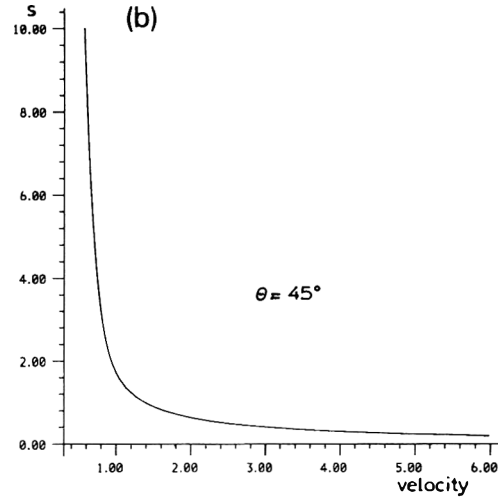
(b)
s
10.00
8.00
6.00
4.00
2.00
0.00
θ= 45°
1.00 2.00 3.00 4.00 5.00 6.00
velocity

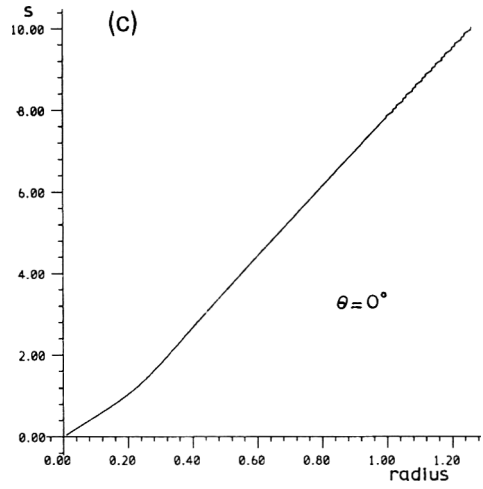
(c)
s
10.00
8.00
6.00
4.00
2.00
0.00
θ=0°
0.00 0.20 0.40 0.60 0.80 1.00 1.20
radius

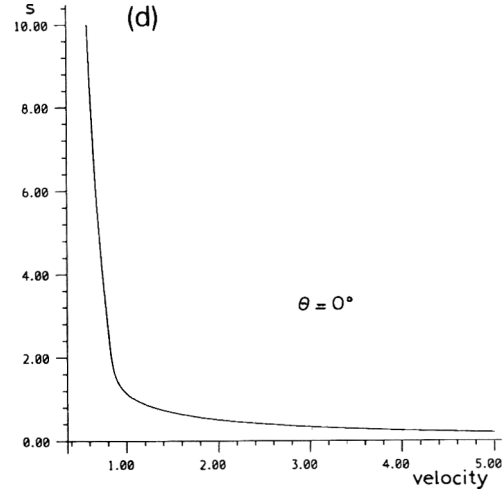
(d)
s
10.00
8.00
6.00
4.00
2.00
0.00
θ = 0°
1.00 2.00 3.00 4.00 5.00
velocity

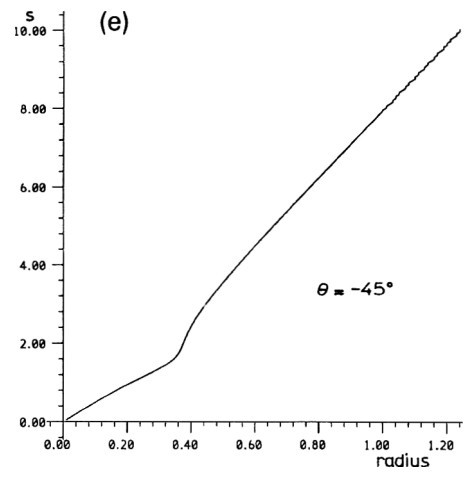
(e)
s
10.00
8.00
6.00
4.00
2.00
0.00
θ = -45°
0.00 0.20 0.40 0.60 0.80 1.00 1.20
radius

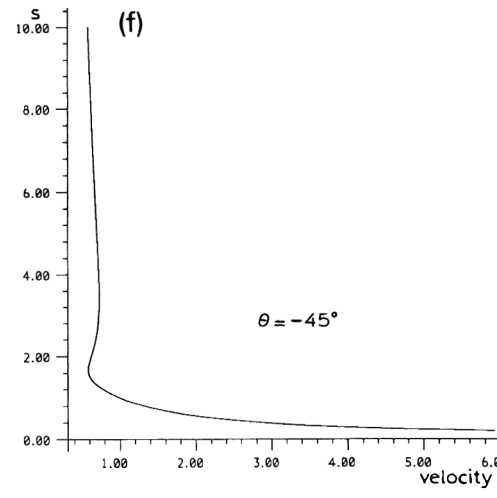
(f)
s
10.00
8.00
6.00
4.00
2.00
0.00
θ = -45°
1.00 2.00 3.00 4.00 5.00 6.00
velocity

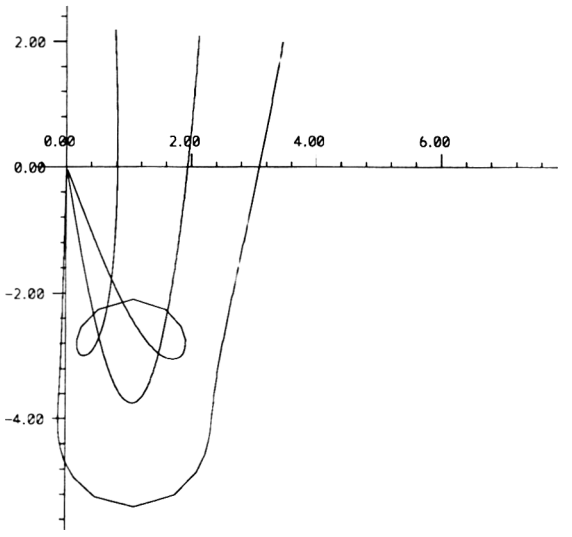

Fig. 15. Shape of plume when the initial angle is $-80°$ showing the upper and lower boundaries and the centre line. Notice that the upward flowing part of the plume overlaps the downward flowing part, thus only that part of the shape beyond the overlap will be realisable in practice.

the initial momentum flux. Thus once the plume turns and begins to rise it is (essentially) equivalent to a source of mass and buoyancy and a relatively small amount of horizontal momentum, placed at (approximately) the position where the plume turns.

Figure 15 shows the predicted plume shape for $\theta_0 = -80°$ and here the theoretical result has the plume overlapping a previous position. It is important to note that the model is invalid in such regions since it does not allow for re-entrainment of plume fluid. Thus for $\theta_0 = -80°$ the model is only valid for $s > 2.5$, where the predicted shape is not overlapped by a previous part of the flow. There is some overlap for θ_0 steeper than approximately $-75°$.

It should also be noted that the top edge of the plume is unstable in that there is light fluid below heavy fluid. Thus some fluid formerly in the plume will be detrained and rise into the region above the plume. Thus the stable, lower edges of the plume shapes shown in Fig. 10 will be sharply defined in practice, whereas the upper, unstable edges will be poorly defined. See, for comparison, the photograph of a real plume in Fig. 16, described below.

Fig. 14. The radius and along-axis speed of angled plumes as a function of distance along the plume centre-line. Notice that there is a minimum in the speed for the initially downward pointing plume.

Fig. 16. Shadowgraph of an angled plume. Here the injected fluid is denser than ambient so the buoyancy forces act downward.

6. Experiments

Forced plumes were produced by pumping salt water through a circular pipe (1.95 mm diameter) into a tank containing fresh water. Note that since the injected fluid is relatively dense, the buoyancy forces on the plume act downwards, rather than upwards as was the case for the theory above. The tank dimensions were 4 m long by 0.3 m wide and it was filled to a depth of about 0.5 m. These dimensions are large compared with typical length scales of the flow and so this configuration approximates an infinite, unstratified environment at rest. The flow rate πQ_0 was monitored with a flow meter and the buoyancy flux πF_0 and the momentum flux πM_0 were determined from

$$F_0 = g' Q_0,$$

$$M_0 = \tfrac{4}{3} Q_0^2 a^{-2}, \tag{23}$$

where a is the pipe radius.

Typical pipe nozzle Reynolds numbers were in the range 1000 to 2500 and the expression for M_0 is obtained assuming laminar Poiseuille flow in the pipe. The

pipe was set at fixed orientations θ_0 to the horizontal and the angles were measured to an accuracy of 0.5°.

The visualisation was carried out using a shadowgraph and estimates of the maximum height were made from still photographs. A conductivity probe was placed at a set of fixed positions in the flow and the salt concentration was measured to obtain information about the structure and mixing in the plume.

7. Experimental results

An example of the flow with $\theta_0 = 60°$ is shown in Fig. 16. Close to the source the plume is symmetrical but a pronounced asymmetry develops downstream. The upper side of the plume remains sharp and well defined while the lower side is diffuse and has no distinct edge even in an instantaneous picture as shown in the shadowgraph. This asymmetry results from the opposite effects of the buoyancy force on the two sides of the plume. On the upper side, buoyancy forces create a stabilizing stratification which tends to inhibit entrainment of the environmental fluid. On the lower side the buoyancy forces produce a convectively unstable configuration and there is enhanced mixing between the plume and the environment. *Detrainment* of plume fluid is observed on the lower side, a feature which is not observed in vertical plumes.

Measurements of the structure of the plume were made for an initial inclination of 45° using a conductivity probe. Figure 17 shows the density contours in a plane normal to the plume axis positioned at the point of maximum plume height. The asymmetry between the upper and lower parts of the plume can be clearly seen. Near the top of the plume there is a strong, stable density gradient. Below the plume axis the dense fluid is mixing much more vigorously with the surrounding fluid as a result of the gravitational instability. Density profiles in a vertical plane containing the plume axis are shown in Fig. 18a.

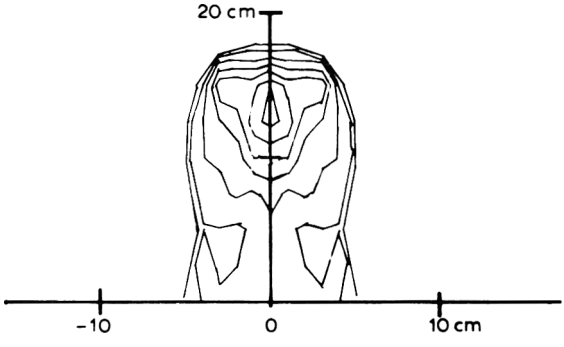

Fig. 17. Experimentally observed, time-averaged, measurements of concentration in a plane perpendicular to the plume axis, at the highest point on the plume. The injected fluid was denser than ambient, and injected at an angle of 45 above the horizontal. Notice the detrainment of fluid from the lower, unstable edge of the plume.

The asymmetry between the upper and lower parts of the plume is seen to increase with distance downstream. The estimated plume axis (line of maximum density excess) is shown in Fig. 18b, as is the theoretically predicted plume axis. The discrepancy is due partly to experimental errors, in particular in measuring the source radius accurately and in measuring the relatively weak concentrations far from the source, and partly due to using a fixed value of α that is certainly too large for the jet part of the flow, and may be too large for the mass-source part of the flow. The mean value of the density difference on the plume centre-line is plotted on Fig. 19, as is the theoretical prediction. Note that the observed density difference is generally larger than the prediction, suggesting less entrainment than predicted (smaller α), which would lead to greater vertical acceleration.

The maximum height to which the upper plume boundary rose, z_M, was measured from photographs, and non-dimensionalised with respect to the length-scale L_1 (see eq. 22). These results are shown on Fig. 11, where each point represents the average over several experiments with different values of the flow rate. The comparison with the theoretical results was discussed in Section 4. Some experiments were performed with the tube set vertically, so

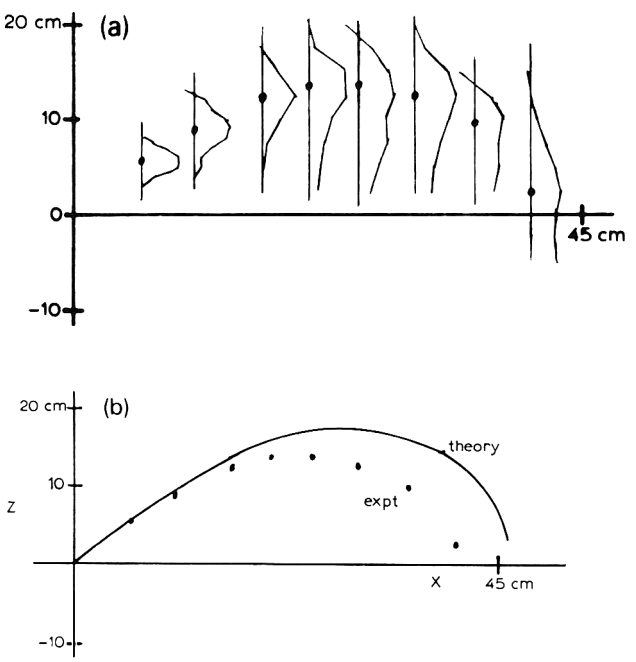

Fig. 18. (a) Vertical, time-averaged concentration profiles measured at various points along the plume centre-line. The injected fluid is denser than the surrounding fluid and was injected at 45°. (b) Position of the plume centre-line estimated from the experimental results shown in (a) (peak in density profile), with the expected centre-line for comparison. (Non-dimensional scales.)

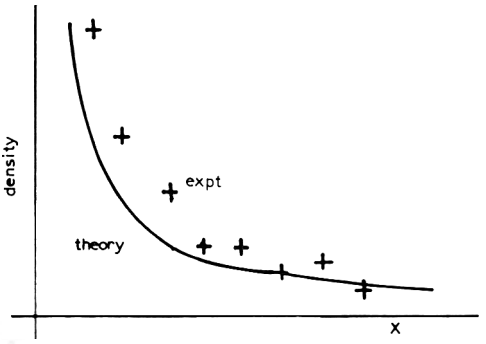

Fig. 19. Density difference between the plume fluid and the ambient fluid from the experiment shown in Figs. 16 to 18 (time-averaged on the plume centre-line), with the theoretical result shown for comparison. (Non-dimensional scales.)

that the rising part of the plume entrains fluid that is falling back down. This height cannot be predicted by the theory above, since it assumes that only ambient fluid is entrained. These experiments gave a value of the maximum height of $z_M(90^\circ) = 0.83 \pm 0.02$, in agreement with the value found by Turner [12]. Note that this is much smaller than the value of approximately 1.8 predicted by the model, which does not include re-entrainment of the plume fluid. Thus the re-entrainment of plume fluid has a substantial effect on the plume.

8. Conclusions

The equations for a forced, angled plume can be simplified by non-dimensionalisation with respect to two conserved quantities, namely the buoyancy flux and the horizontal component of the momentum flux. All such plumes can be traced back to a virtual origin, and the *shape* of the plume depends only on the angle of the plume to the horizontal at this virtual origin. Vertical plumes can be included in this scheme, with virtual origin angle $\pm 90^\circ$. All angled plume shapes can be grouped into three categories, first introduced to describe vertical plumes:

(i) If the momentum flux at the virtual origin is zero then no angle can be defined and we have the special case of the vertical, straight-sided, *pure plume*, half-angle $\tan^{-1}(6\alpha/5)$.

(ii) If the momentum flux at the virtual origin is upward (or horizontal) then the plume spreads initially at a half-angle of $\tan^{-1}(2\alpha)$. We have referred to this category as the *buoyant jet*. The plume centre-line curves towards the vertical and the spreading angle tends (downward) to that of the pure plume. The change from the jet spreading angle to the plume angle occurs more sharply for plumes directed further from the vertical.

(iii) If the momentum flux at the virtual origin is downward then the initial spread is as for a jet. In this case the fluid is decelerated by the buoyancy force and the spreading angle increases. As the plume centre-line curves

upward the fluid is accelerated and the spreading angle decreases, for plumes with virtual origin angle less than approximately $-60°$ the radius actually decreases. As the plume centre-line curves upward the spreading angle tends (upward) to that of the pure plume. This category we have referred to as the *mass-source*. In this case the mean along-plume velocity has a minimum and a maximum (see Fig. 14), whereas the velocity decreases monotonically for cases (i) and (ii). Note also that part of the solution near the virtual origin will be unphysical for sufficiently steep values of θ_0, due to the model not allowing for re-entrainment of plume fluid. In particular, for $\theta_0 = -90°$ the solution is unphysical until the flow is upward.

The overall *size* depends on the length scale L_A defined above. For the vertical plumes it is, however, necessary to trace the solution back to the virtual origin to find a useful scale for the momentum flux, which can be used to define a length-scale, L_V. Because of this last feature we regard vertical plumes as a very special case of the generality of angled plumes. This is in contrast to the usual approach which is to consider plumes with a horizontal component of momentum flux as merely a minor departure from the vertical case, as is, for example, implicit in the dimensional analysis approach to predicting maximum depth of a downward angled buoyant plume, or explicit in the approach used by Germeles [4].

The virtual origin angle, and thus the shape of the plume, can be determined from the source angle and the non-dimensionalised source mass flux. While the variations of the velocities and densities from the mean and the details of the eddies and entrainment is beyond the scope of this approach, we have shown that the theory predicts some of the mean properties and the basic shape of such plumes reasonably accurately. In fact the entrainment assumption describes the flow surprisingly accurately, given that the observed velocity and density distributions are neither symmetric nor self-similar. We conclude that the average entrainment into the plume is described adequately by an average entrainment velocity proportional to the mean velocity in the plume.

In this model we have kept α constant, though there is evidence that the nature of the entrainment, and thus the value of α, varies for different types of plume flow (see, for example, Turner [12]). Altering the value of α alters the local length-scale and the spreading angle of the plume, and the experimental evidence is that this reduces the difference in spreading angle between jet and plume flows predicted by theories such as the one given here. One may regard different spreading angles predicted by our theory as pointing out changes in the nature of the flow, and thus the entrainment, at different points on the plume. It would be possible to recalculate the results with α allowed to vary according to the local nature of the flow. It is important to note that this would not affect the result that the plume shape is entirely determined by the virtual origin angle, since different plumes with the same virtual origin angle would have changes, e.g. from jet to plume behaviour, at equivalent points on the plume.

This model does not allow for stratification in the ambient fluid. In many cases the stratification will not be important until the plume is rising almost vertically, where previous models (e.g. [2, 3]) can be used. Stratification will not be important in the neighbourhood of the source provided that the density changes in the ambient fluid over the length scale of the plume are small compared with the density difference between the plume and the ambient fluid. This criterion requires

$$N \ll F_0/H_0, \tag{24}$$

where the ambient stratification has buoyancy frequency $N=(-g(\partial\rho/\partial z)/\rho)^{1/2}$.

When stratification is important this can be taken into account by modifying equation (11) (the buoyancy flux is no longer constant) so that the right hand side of the density difference equation becomes N^2VR^2. However, this is not entirely satisfactory since under such strong stratification the plume cross-section becomes elliptical, with greater spread in the horizontal direction and reduced spread in the vertical direction because vertical motions are impeded by the stratification. The reader is recommended to see Hofer and Hutter [6] for a more detailed analysis.

Acknowledgements

G.F.L-S was supported by a Research Scholarship from British Gas plc when conducting this work, and M.H. by a grant from the Wolfson Foundation.

References

1 B.R. Morton, G.I. Taylor and J.S. Turner, Turbulent gravitational convection from maintained and instantaneous sources, Proc. R. Soc., 234 (1956) 1–23.
2 B.R. Morton, Forced plumes, J. Fluid Mech., 5 (1959) 151–163.
3 B.R. Morton, The ascent of turbulent, forced plumes in a calm atmosphere, Int. J. Air Water Pollut., 1 (1959) 184–197.
4 A.E. Germeles, Forced plumes and mixing of liquids in tanks, J. Fluid Mech., 71 (1975) 601–623.
5 M. Schatzmann, The integral equations for round buoyant jets in stratified flows, J. Appl. Math. Phys. (ZAMP), 29 (1978) 608–620.
6 K. Hofer and K. Hutter, Turbulent jet diffusion in stratified, quiescent ambients. Part 1: Theory. J. Non-Equil. Thermodyn., 6 (1981) 31–48.
7 G.I. Taylor, Dynamics of a mass of hot gas rising in air, U.S. Atomic Energy Commission MDDC 919. LADC 276, 1945.
8 E. List, Turbulent jets and plumes, Annu. Rev. Fluid Mech., 14 (1982) 189–212.
9 J.S. Turner, Buoyancy effects in fluids, Cambridge University Press, Cambridge, 1973.
10 H. Rouse, C.S. Yih and H.W. Humphreys, Gravitational convection from a boundary source, Tellus, 4 (1952) 201–210.
11 H.B. Fisher, E.J. List, R.C.Y. Koh, J. Imberger and N.H. Brooks, Mixing in Inland and Coastal Waters, Academic Press, New York, 1979.
12 J.S. Turner, Jets and plumes with negative or reversing buoyancy, J. Fluid Mech., 26 (1966) 779–792.

Journal of Hazardous Materials, 33 (1993) 101–122
Elsevier Science Publishers B.V., Amsterdam

A model of the motion of a heavy gas cloud released on a uniform slope

D.M. Webber, S.J. Jones and D. Martin

SRD, AEA Technology, Wigshaw Lane, Culcheth, Warrington WA3 4NE (UK)

(Received November 15, 1991; accepted in revised form July 20, 1992)

Abstract

A model is presented of the motion of a heavy gas cloud down a uniform slope in calm ambient conditions. The model is derived from solutions of the shallow water equations with appropriate boundary conditions. Its predictions are shown to agree adequately with experimental results in calm conditions, and a possible generalisation to allow for the presence of a wind is discussed.

1. Introduction

Integral (or box) models of gas dispersion are now a standard tool for the analysis of flammable and toxic hazards, posed by major industrial plant. Recent developments, including work under the recently completed Major Technological Hazards programme of the Commission of the European Communities, have been aimed at extending the understanding of heavy gas flows to situations where the nature of the terrain, or of structures on it, may have a significant effect on the dispersion.

One such relatively simple situation is that where the ground slopes. Hazardous clouds are very often significantly heavier than air and such sloping terrain is known to have a important effect. Models of the behaviour of a heavy cloud released instantaneously on a slope have recently been presented by Deaves and Hall [1] and by Nikmo and Kukkonen [2].

Each of these models is an intuitively appealing generalisation of the flat ground integral model approach to include the effect of slopes. However, in each case the effect of the slope is only found with a numerically computed solution to a set of differential equations. Whilst this situation is quite usual, it is highly desirable to have a more direct understanding of the nature and effects of the assumptions involved in such models.

Correspondence to: D.M. Webber, SRD, AEA Technology, Wigshaw Lane, Culcheth, Warrington WA3 4NE (UK). Fax: +44-925-254-537.

0304-3894/93/S06.00

The importance of such an understanding cannot be overstated. Credible hazard analysis can only come about using models which are well validated on (of necessity) small scale data, and which incorporate sound physical assumptions (and accurate calculational methods) in extrapolating their predictions to larger scales. In situations where data are relatively sparse, and the possible validation therefore relatively incomplete, the importance of the sound physical assumptions is highlighted still further.

Our objective here, then, is to examine the very simple case of a heavy cloud released instantaneously on to a uniform slope and dispersing isothermally in a way which is known to conserve buoyancy. We shall focus here on the effect of the slope on the overall motion of the cloud, rather than on any effect it may have on dilution rates. In order to do this, we shall start by discarding all other complicating factors. We therefore restrict ourselves *a priori* to the case of zero wind, and idealise to the extent that no mixing is assumed. This, as we shall show, allows considerable progress in understanding the effect of the cloud falling down the slope.

In particular an equation is derived relating the cloud's terminal velocity down the slope (where gravity balances resistance forces) to its density and volume, and to the gradient of the slope. Comparison with data will show that this assumption yields very plausible results.

2. Two-dimensional releases on slopes

2.1 Introduction

Our main purpose is to present results for the case of a three-dimensional cloud released instantaneously. The derivation of this model, however, relies strongly on the two-dimensional results already presented by Jones et al. [3], which we shall therefore review briefly here.

The essential assumption of our approach is that it is reasonable to consider the motion of a cloud on a slope, independently of its mixing with the ambient air. Thus we are attempting to assess how a (fictitious) cloud of fixed density might behave on a slope. Of course, any complete model of gas cloud behaviour must model mixing accurately, and we shall return to a discussion of this below.

The behaviour of a cloud of fixed density is readily accessible via the shallow water equations, which contain the added assumptions that the cloud is of large horizontal extent compared with its depth, and that the slope is not too steep. That is to say, if we designate the fluid depth as H, the horizontal extent Λ, and the gradient of the slope Γ: we require $H \ll \Lambda$ and $\Gamma \ll 1$. Later we shall discuss the regimes $H = O(\Gamma\Lambda)$ and $H \gg O(\Gamma\Lambda)$. Let us note here that these are not incompatible with the formal restrictions imposed by shallow water theory. For our purposes here, when we refer to a "tall" cloud we mean $H \gg O(\Gamma\Lambda)$ rather than one which violates the shallow ($H \ll \Lambda$) assumption.

2.2 The two-dimensional shallow water model

The shallow water equations in one horizontal dimension (implying a two-dimensional flow when the vertical, depth-averaged dimension is counted) are:

$$\frac{\partial(h-a)}{\partial t}+\frac{\partial(u(h-a))}{\partial x}=0 \tag{1}$$

$$\frac{\partial u}{\partial t}+u\frac{\partial u}{\partial x}+g''\frac{\partial h}{\partial x}=0 \tag{2}$$

Here t is time, and x is the horizontal space coordinate. The fields are the horizontal velocity u and the height h of the top of the cloud above a fixed datum (see Fig. 1). The quantity a, is the height of the ground level above the datum, so that $h-a$ is the fluid depth. We are considering a cloud of density ρ spreading in an ambient atmosphere of density ρ_a and g'' is the reduced acceleration due to gravity

$$g''=g(\rho-\rho_a)/\rho \tag{3}$$

In the case studied here, as mixing is not yet incorporated into the model, g'' is constant.

The fact that there will be significant resistance exerted by the ambient air to the cloud spread is embodied in the boundary conditions. This resistance to motion can be incorporated [4–7] in the boundary condition

$$u_f=k_f\sqrt{g'(h-a)_f} \tag{4}$$

where g' is defined, (slightly differently from g'') by

$$g'=g(\rho-\rho_a)/\rho_a \tag{5}$$

and $(h-a)_f$, u_f are the fluid depth and (normal component of) velocity at the edge of the cloud, and k_f is a constant (O(1)) Froude number. (Note that k_f is

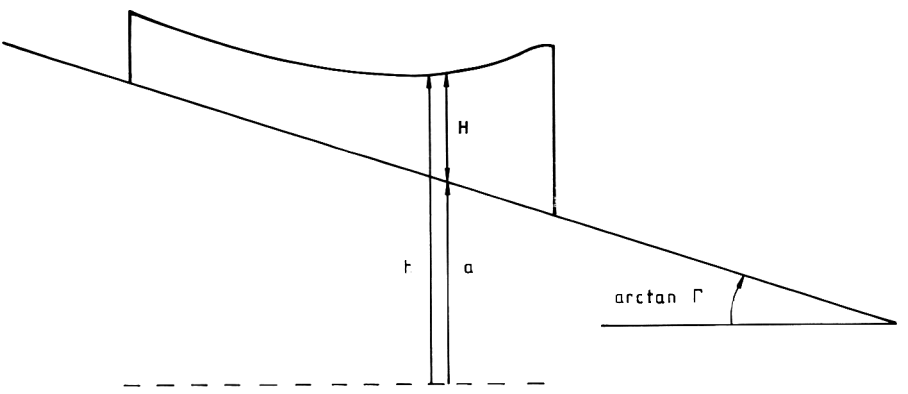

Fig. 1. A gas cloud on a slope; definition of geometric variables.

not identical to the similar quantity used in integral models, which is based on the mean depth rather than the frontal depth; for self similar flow the two Froude constants have a constant ratio.)

The above boundary condition expresses a resistance pressure of the ambient air and we shall adopt it wherever the cloud edge is moving into the ambient fluid.

Where the cloud edge is receding from the ambient fluid we shall adopt the boundary condition

$$h_f = 0 \tag{6}$$

allowing movement of the trailing edge without resistance.

Here we shall consider only a uniform slope, downwards in the direction of increasing x, given by

$$a(x) = -\Gamma x \tag{7}$$

where the slope Γ is constant and positive.

2.3 Analytic solution of the shallow water equations

As we have seen [3], there is a very simple analytic solution of the above problem, representing a wedge of gas moving downhill at its terminal velocity (corresponding to a balance of gravity and resistance forces). The derivation of this is briefly as follows.

Assume there is a "terminal velocity" solution in which the fluid velocity is independent of both time and space. If this is the case, then the first of the two shallow water equations becomes

$$\left(\frac{\partial}{\partial t} + u\frac{\partial}{\partial x}\right)(h-a) = 0 \tag{8}$$

and the solution must have the form

$$(h-a) = H(x-ut) \tag{9}$$

for some function H. At the rear boundary, $x = X_b(t)$, which follows the cloud, the fluid height is zero, so that

$$H(X_b - ut) = 0 \tag{10}$$

and the origin of the coordinate system can now be chosen so that $X_b = ut$. The boundary condition at the front is

$$(h-a)_f = u_f^2/g'k_f^2 \tag{11}$$

and this can now be rewritten as

$$H(X_f - ut) = u_f^2/g'k_f^2 \tag{12}$$

where X_f is the position of the front of the fluid region. The right hand side of this equation is constant, as the velocity is constant (by assmption), and therefore the left hand side of this equation has to be constant. If the extent of the gas cloud is $L = X_f - X_b$ then:

$$H(L) = u^2 / g' k_f^2 \tag{13}$$

and L must therefore be constant. Note also from eq. (11) that a solution with constant u implies constant frontal depth.

The second equation of the two shallow water equations can be written as

$$\frac{\partial u}{\partial t} + u \frac{\partial u}{\partial x} = -g'' \left(\frac{\partial (h-a)}{\partial x} - \Gamma \right) \tag{14}$$

With the velocity u assumed independent of space and time, this equation reduces to

$$\frac{\partial (h-a)}{\partial x} = \Gamma \tag{15}$$

where $\Gamma = -\mathrm{d}a/\mathrm{d}x$ is the gradient of the slope as defined above. With $h-a$ of the above form $H(x-ut)$, then clearly we must have

$$H(x-ut) = \Gamma [x-ut] \tag{16}$$

up to a possible additive constant, (which is simply equivalent to a choice of origin). The front depth $(h-a)_f$ is now just ΓL, and so the front condition gives the terminal velocity

$$u = k_f [\Gamma g' L]^{1/2} \tag{17}$$

It is convenient to define the two-dimensional volume V of the cloud (the volume per unit width or side area). For the above solution this is just

$$V = \tfrac{1}{2} L^2 \Gamma \tag{18}$$

In terms of this, the cloud moves at a speed

$$u = 2^{1/4} k_f \Gamma^{1/4} [g'^2 V]^{1/4} \tag{19}$$

The last factor can be anticipated from dimensional analysis, but this result does show that the heavy gas cloud (of a given volume and density) moves down the slope with a terminal velocity proportional to the fourth root of the gradient of the slope.

2.4 Numerical solution of the shallow water equations

It is worth emphasising that the above analytic solution was originally found after a numerical solution had revealed this very simple asymptotic behaviour at large time. This demonstrates that the solution is indeed a stable one, and is therefore valid within the assumptions. The evolution found for a wedge released from rest is shown in Figures 2(a–d).

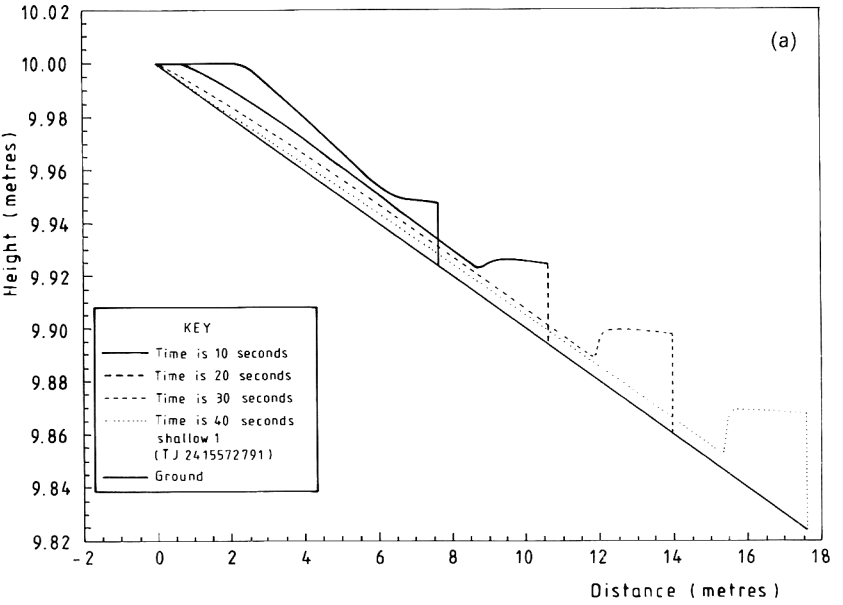

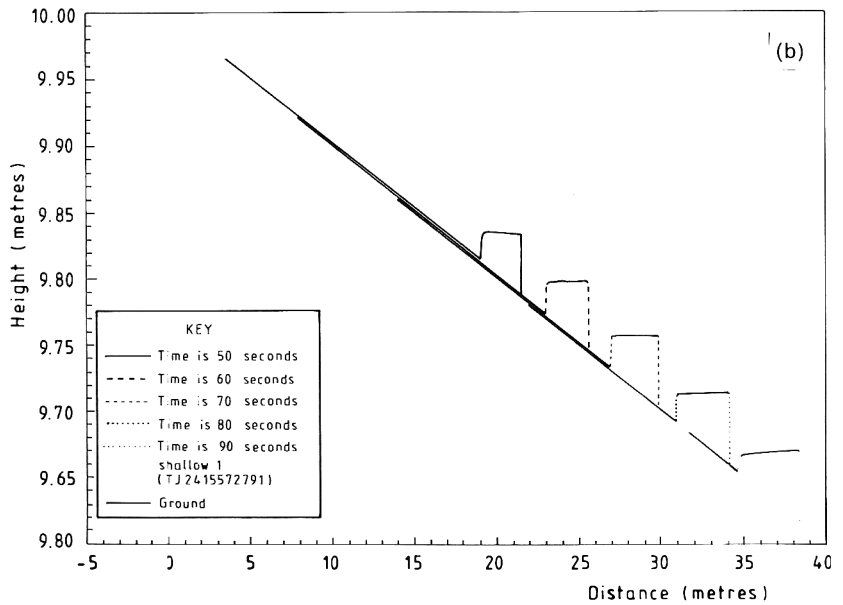

Fig. 2.(a, b). Motion, in two dimensions, of a "wedge" released from rest, showing the development of "head" and "tail" regions separated by a hydraulic jump.

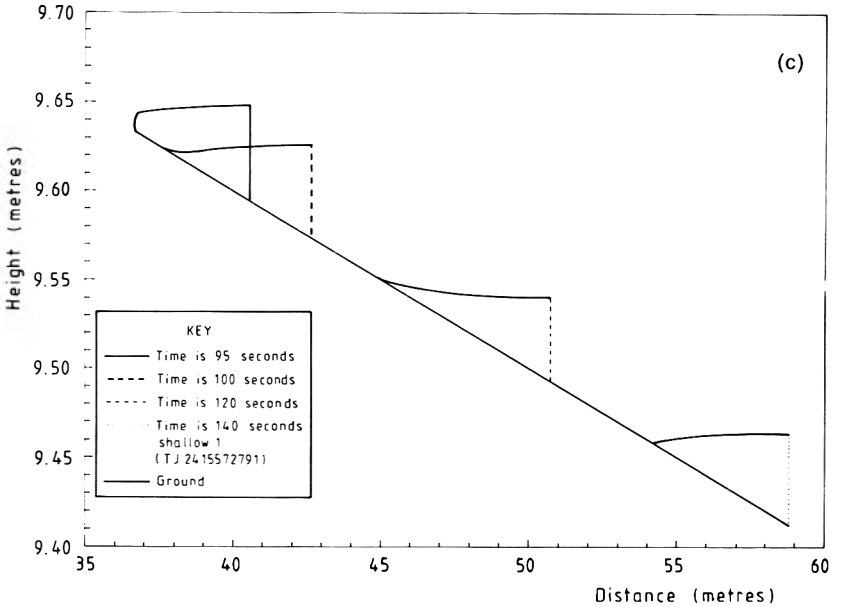

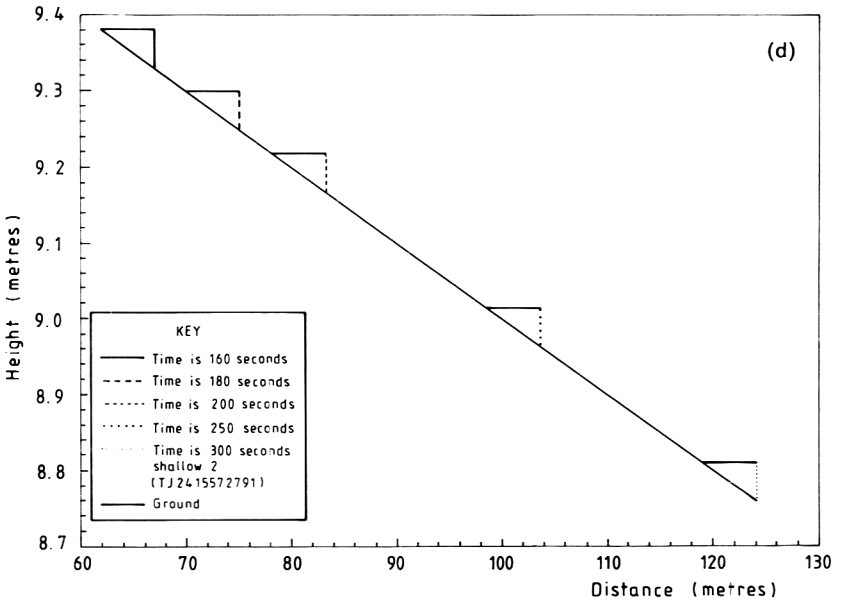

Fig. 2.(c, d). Continued motion, in two dimensions, of a "wedge" released from rest, showing the collapse of the hydraulic jump and the formation of a wedge moving uniformly.

2.5 Comment

The solution of the shallow water equations discussed above is peculiar in that the cloud does not spread. This is a consequence of the boundary conditions, combined with the existence of a slope. The motion of the down slope edge, is just as one would expect for a cloud on flat ground; the collapse of the upslope edge, and the subsequent $H=0$ boundary condition, does not constrain its velocity, allowing it simply to follow the fluid motion. In this way the slumping is turned into a bulk downhill motion. It is thus clear how the assumptions built into the model can yield this result, which we feel is eminently plausible.

3. Three-dimensional releases on slopes

3.1 The shallow water model

The two-dimensional model of Section 2 is interesting but very restrictive. More interesting is the corresponding evolution of a three-dimensional cloud released on the slope. Our numerical scheme for solving shallow water equations cannot yet cope with three dimensions (two horizontal dimensions) but, as we shall now show, there does exist an almost equally simple analytic solution in this case.

Consider first the cross-slope dimension. At first one might imagine that the cloud's behaviour as regards this dimension is unaffected by the slope. However, a cloud which does not spread longitudinally on the slope, but which continues to spread laterally, seems a little outlandish. It would therefore seem pertinent to assume that a solution exists which spreads neither longitudinally nor laterally, but moves down the slope with no change in shape. This is the key to the derivation of the appropriate solution.

3.1.1 Shallow water equations

Following the method adopted for the two dimensional case, we take the shallow water theory in the horizontal plane with coordinates $\boldsymbol{x}$ in the form

$$\frac{\partial(h-a)}{\partial t}+\nabla\cdot(\boldsymbol{u}(h-a)=0 \tag{20}$$

$$\frac{\partial \boldsymbol{u}}{\partial t}+(\boldsymbol{u}\cdot\nabla)\boldsymbol{u}+g''\nabla h=0 \tag{21}$$

with g'' as before, and a uniform slope

$$a(\boldsymbol{x})=\Gamma\boldsymbol{x}\cdot\hat{\boldsymbol{n}} \tag{22}$$

where, in keeping with our earlier two-dimensional formalism, we take

$$\hat{\boldsymbol{n}}=(-1,0) \tag{23}$$

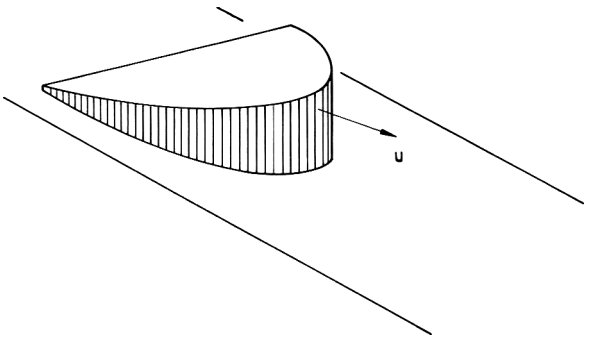

Fig. 3. A three-dimensional cloud moving uniformly, at constant velocity with no change in shape. The shallow water equations with appropriate boundary conditions admit a solution of this form.

in the (x, y) plane. We shall now show that there is a solution for a cloud of constant uniform velocity, flat top, and fixed shape, exactly as in the two-dimensional case. Figure 3 illustrates this situation.

3.1.2 Solution of the equation

In fact it is clear that there is a solution of the equations with

$$\boldsymbol{u} = -u\hat{\boldsymbol{n}} \tag{24}$$

with constant u, and

$$(h-a) = H(\hat{\boldsymbol{n}}\cdot(\boldsymbol{u}t-\boldsymbol{x})) \tag{25}$$

with

$$\nabla H = -\Gamma\hat{\boldsymbol{n}} \tag{26}$$

implying

$$H = \Gamma\hat{\boldsymbol{n}}\cdot(\boldsymbol{u}t-\boldsymbol{x})$$

3.1.3 The boundary condition at the rear

The rear of the cloud again has zero depth and, at any given time t, is a straight line across the slope given by

$$\boldsymbol{x} = \boldsymbol{X}_b(t, y) \tag{27}$$

for y in $[-Y, +Y]$, where

$$\boldsymbol{X}_b(t, y) = \boldsymbol{u}t + (0, y) \tag{28}$$

and Y is the overall half-width of the cloud at the trailing edge.

3.1.4 The boudnary condition at the front

Having thus satisfied the trailing boundary condition, it remains to satisfy the front condition. Let us take the length of the cloud in the direction of the slope to be $L(y)$, as illustrated in the plan view of Fig. 4. This is such that $L(-y)=L(y)$; $L(Y)=0$; and we define $L(0)=\Lambda$. The front condition

$$u_f = k_f \sqrt{g'(h-a)_f} \tag{29}$$

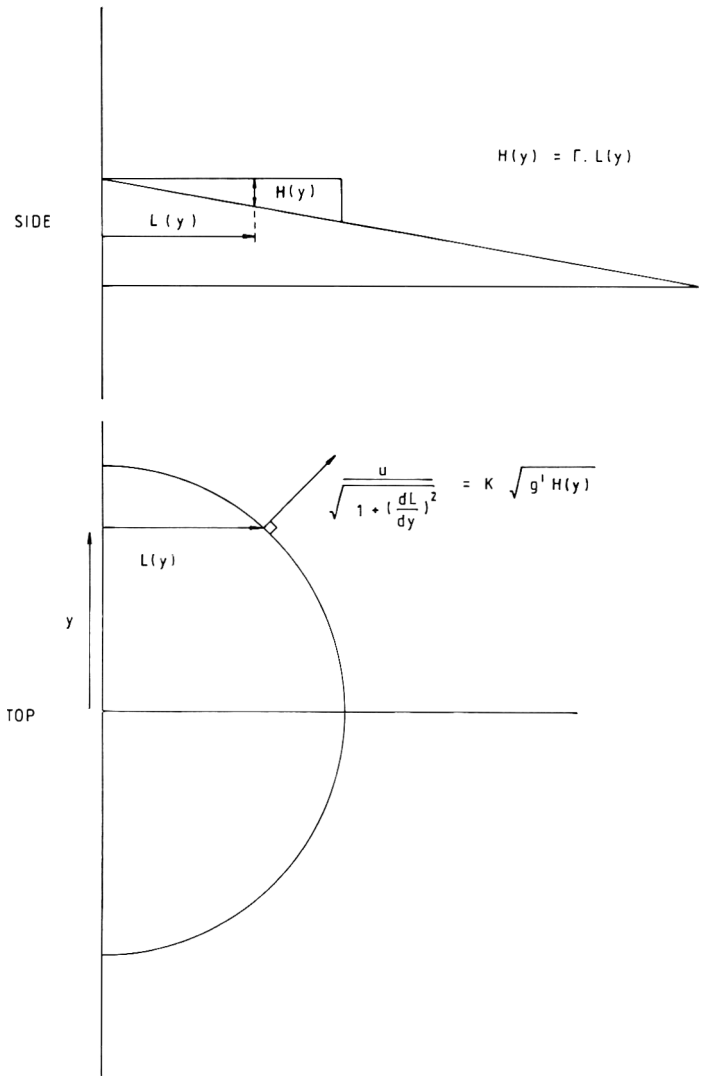

Fig. 4. Determination of the shape of the cloud from the boundary conditions.

is now defined for a front velocity component u_f orthogonal to the edge of the cloud. Therefore

$$u_f(y) = u \Big/ \sqrt{1 + \left(\frac{dL}{dy}\right)^2} \tag{30}$$

at a transverse distance y from the centre line. At this point $(h-a)_f = \Gamma L(y)$, and so, after a little manipulation, the boundary condition gives the equation

$$\frac{dL}{dy} = -\sqrt{\frac{u^2}{k_f^2 g' \Gamma L} - 1} \tag{31}$$

from which we deduce

$$\Lambda = u^2 / k_f^2 g' \Gamma \tag{32}$$

and

$$\frac{d\hat{L}}{d\hat{y}} = -\sqrt{\frac{1-\hat{L}}{\hat{L}}} \tag{33}$$

where

$$\hat{L} = L/\Lambda, \qquad \hat{y} = y/\Lambda \tag{34}$$

The solution of this equation may be written parametrically as

$$\hat{L} = \cos^2 \omega$$

$$\hat{y} = \omega + \cos\omega \sin\omega \tag{35}$$

This shape is illustrated to scale in Fig. 5. This completes the three-dimensional generalisation of the simple free-fall cloud presented for two-dimensions in Section 2.

3.1.5 Properties of the solution

As we have already noted, the velocity u is related to the overall length Λ of the cloud by

$$u = k_f \sqrt{g' \Gamma \Lambda}$$

As before, it is appropriate to relate this to the volume V of the cloud. This is given by

$$V = \int_{-\frac{\pi}{2}\Lambda}^{+\frac{\pi}{2}\Lambda} dy \int_0^{L(y)} dx \cdot [\Gamma x] = \Gamma \Lambda^3 \Omega_6 \tag{36}$$

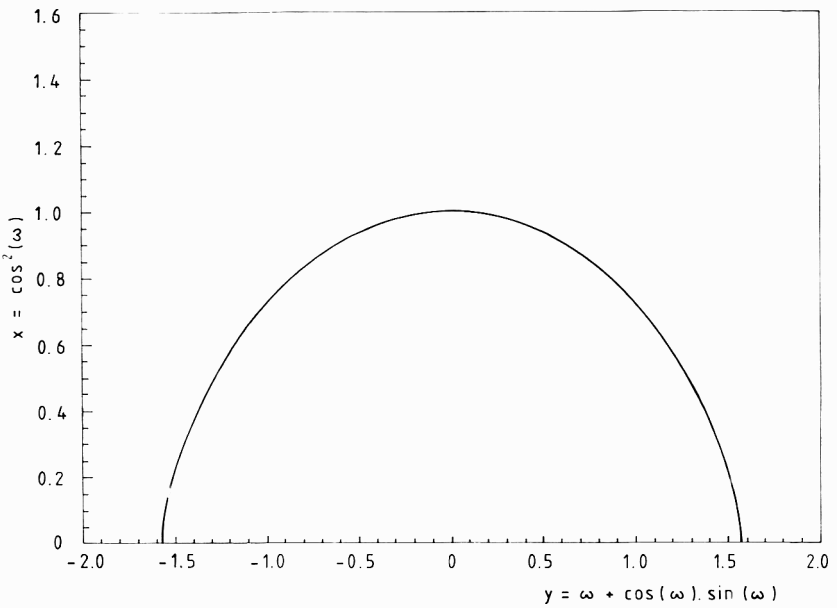

Fig. 5. The scaled plan view of the cloud. The full width (Y) is π times the length (X).

where

$$\Omega_6 = \int_{-\frac{\pi}{2}}^{+\frac{\pi}{2}} d\omega \cos^6 \omega = \frac{5\pi}{16} \tag{37}$$

Our final result for a cloud of given volume and density is that the free-fall velocity on a slope Γ is

$$u = \Omega_6^{-1/6} k_f \Gamma^{1/3} \sqrt{g' V^{1/3}} \tag{38}$$

This is slightly different from the two-dimensional result. The final factor is again as expected from dimensional analysis, but the slope dependence is now a cube root in place of the fourth root wich pertained earlier. It is also interesting to note the prediction that the cloud is π times as wide across the slope as it is long.

Examining the solution, we can again see how a non-spreading cloud can come about. In the longitudinal direction it is exactly as in the two-dimensional case. The edge velocity is at all points normal to the cloud boundary, but is exactly accounted for by the overall motion of the cloud. At the outside rear edge where the normal points across the slope, the depth and the spreading velocity reach zero together, allowing a non-spreading solution.

3.2 Air entrainment

Modelling air entrainment in the context of the shallow water model is a fairly complicated exercise. A very practical course, however, which is in keeping with the philosophy of simple integral models, is to assume an air entrainment model into a cloud which continues to move on the slope in the above self-similar way. (We shall discuss the possibility of introducing an ambient wind later.) This is not inconsistent with the sort of behaviour discussed by Britter et al. [8].

In this case the entrainment is assumed just such that the relationship between down-slope velocity u, volume V, and density (implicit in g') is preserved. This allows a very natural generalisation of integral models on flat ground to the case of a uniform slope.

However, if we set out in that direction, any test which we were to apply to the model would depend both on the entrainment model and on the down-slope free-fall model considered here. It would be far preferable if we could test the ideas presented here, independently of the precise details of any entrainment model. In fact we can do this to some extent as is shown in the next section.

4. Comparison with data

4.1 The experiments of Schatzmann et al. [9]

4.1.1 Introduction

As part of their contribution to the CEC Major Technological Hazards project, Schatzmann et al. [9] used a boundary layer wind tunnel to model an instantaneous release of a dense gas on an inclined plane in conditions of zero ambient flow. This corresponds as closely as possible to the idealisation in our model, and so it is interesting to compare the predictions model with these results. (Steady-continuous releases were also performed, but consideration of these is outside the scope of the model presented here.)

4.1.2 Experimental set-up

In these experiments instantaneous releases were achieved by filling a 450 cm^3 cylinder with a mixture of sulphur hexafluoride (SF_6) and air to the required density and then abruptly retracting the side walls into the wind tunnel floor. Ground level SF_6 concentrations were then measured at eight points down the slope (three on the centre line, five off axis) using artificially aspirated hot-wire anemometers with a sampling rate or either 10 or 12.5 Hz. The concentration time history from each of the sensors is available without additional filtering or averaging.

Each release was repeated five times using identical initial conditions with zero ambient wind. Three different inclines, ranging from 4% to 11.63% (see Fig. 1), were also used. Note that the largest of these, $\Gamma = 0.1163$, is still a shallow slope in the terms discussed earlier.

4.2 Comparison of the model with the data

4.2.1 Model considerations

It is desirable to compare the predictions of the model, independently of any particular entrainment model. As it stands in Section 3 the model relates cloud velocity with slope, density and volume without recourse to any free parameters (apart from k_f which is already effectively determined from the cloud spreading law on flat ground). It is therefore our objective to extract these quantities from the data in order to test the predicted relation:

$$u = \Omega_6^{-1/6} \cdot k_f \Gamma^{-3} \sqrt{g' V^{1/3}} \tag{39}$$

obtained above.

4.2.2 Data reduction

In order to do this, we need to know the cloud volume and the relative density excess as a function of time and space. In order to avoid complications which might arise from cross-slope density variations, we have chosen in this study to use only the data from the three sensors which there placed on the centre line.

For all fifteen instantaneous release onto inclined planes pure SF_6 was used as the working fluid. Assuming only that this is an isothermal flow of an approximately ideal gas, we know that the flow is buoyancy conserving. That is to say that the cloud-averaged mean density excess

$$\Delta' = (\bar{\rho} - \rho_a)/\rho_a \tag{40}$$

is directly proportional to the concentration (contaminant mass per unit volume), and is therefore related to the volume V by

$$\Delta'_0 V_0 = \Delta' V \tag{41}$$

where subscript 0 indicates the initial values.

For the moment let us make the bold assumption that we can use the measured concentrations as representative of the mean values, and return to argue about this later. In this case the concentration measurements give immediate estimates of density and volume via these relationships. From these we calculate our model prediction for the cloud velocity u, and test to see whether it agrees with the observed rate of travel.

Schatzmann et al. [9] present volumetric concentration C as fraction of the initial concentration (C_0) in the cylinder before the release took place. From this we estimate the volume as

$$V/V_0 = (C/C_0)^{-1} \tag{42}$$

and find the required combination of variables

$$g' V^{1/3} = g'_0 V_0 V^{-2/3} \tag{43}$$

TABLE 1

Resultant estimates of cloud velocity of different slope

Sensor position	C/C_0	u (ms^{-1})
4.0% Slope		
(61.3,0.0)	$5.826\ 10^{-2}$	0.080
(122.61,0.0)	$1.624\ 10^{-2}$	0.052
(183.91,0.0)	$0.962\ 10^{-2}$	0.044
8.6% Slope		
(61.3,0.0)	$8.282\ 10^{-2}$	0.361
(122.61,0.0)	$3.188\ 10^{-2}$	0.263
(183.91,0.0)	$1.516\ 10^{-2}$	0.209
11.63% Slope		
(61.3,0.0)	$8.242\ 10^{-2}$	0.399
(122.61,0.0)	$3.540\ 10^{-2}$	0.301
(183.91,0.0)	$1.464\ 10^{-2}$	0.224

wherein $g_0' V_0$ can be calculated from the initial conditions. The resultant estimates of the velocity u are given in Table 1, taking the concentration (C) from the mean of the maximum concentrations measured by each sensor during the five repeats, and taking $k_1 = 1.07$, a mean spreading Froude number which has been seen [10] to optimise fits to Thorney Island (i.e. flat-ground) data.

We cannot measure the cloud advection velocity directly from the experimental data. We can, however, obtain the cloud arrival time at the three sensor locations. By plotting arrival time against distance from the source we do get at least some indication of the cloud velocity, even though there are only three data points for each run. In Figs. 6(a–c) we have plotted arrival times (+) and drawn a smooth curve (dotted line) through the data to guide the eye. Our predicted velocity is shown as a short line with the appropriate gradient (u) at each data point. If our model were exactly correct, and the extraction of the cloud volume and density accurate, then these lines would be tangents to the curve. Given the uncertainties in the data extraction procedure, we regard the results as sufficiently good to support the shallow water model approach.

It is worth noting that the wedge-shaped flow of our model will take some time to set itself up, and we should therefore expect the model to be better in the far field. The near field data must reflect the initial slumping which is not considered in the model we have presented. It is also interesting that the model seems best when applied to the shallowest slope.

5. Discussion and conclusions

5.1 Significance of the results

Our interpretation of the data is of necessity very crude. The assumption that the measurements reflect the average concentration (or more particularly

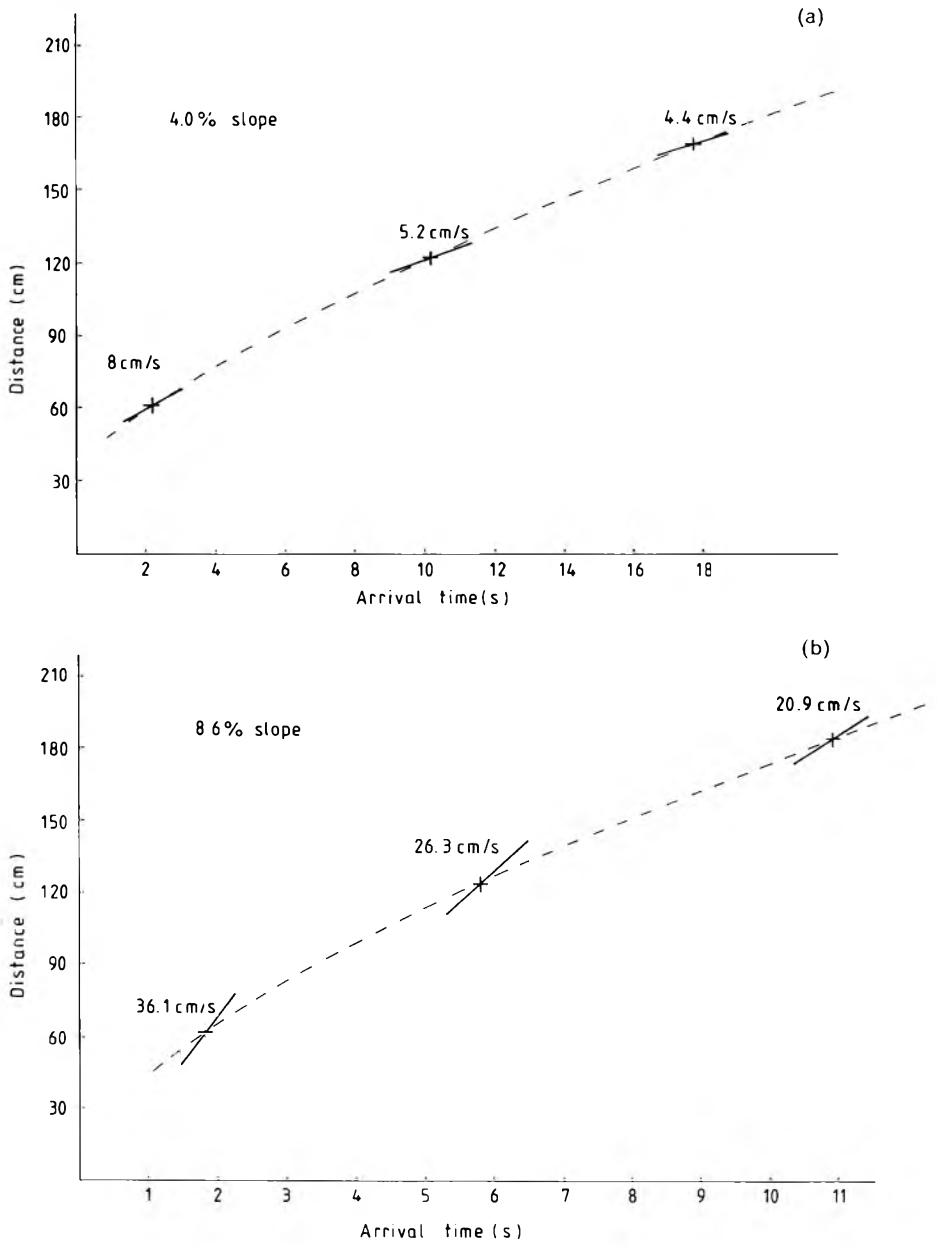

Fig. 6. (a) Centre-line distance travelled versus time for the front of a cloud released at rest on a uniform slope of 0.04. (b) As for (a) but with uniform slope of 0.086. Data are marked (+) and interpolated with a dotted line to guide the eye. The short solid lines indicate the predicted velocity, which if exactly correct, should be tangent to the curve.

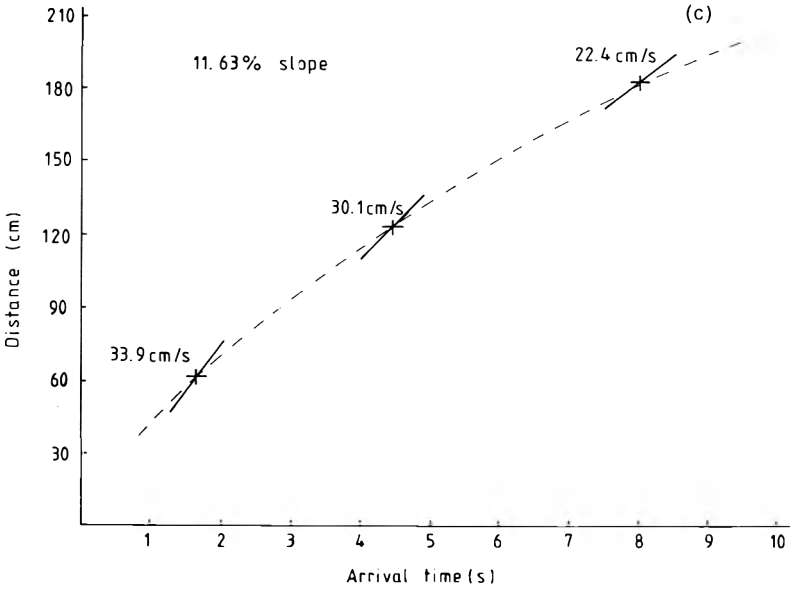

Fig. 6. (c) As for (a) but with uniform slope 0.1163.

the concentration which corresponds to the best choice of density in the shallow water model) looks at first sight to be somewhat cavalier, and to take rather too literally the old box model idea that concentration and density variations are well represented by profiles which are uniform within the cloud and zero outside it.

However, let us now suppose that the profiles are merely self-similar to some reasonable approximation. This is still an assumption of course, but a much weaker one. Self-similarity means that the cloud-average concentration and density are simply constant multiples of the ground-level centre-line value. In particular the combination $\Delta' V$, (where Δ' is now based on the ground-level centre-line density) would still be constant in the self-similar régime. There is still some uncertainty in evaluating this from the initial (non-self-similar state) but this is reduced by the square root in evaluating the velocity.

All in all then, we regard the comparison shown in Figs. 6(a–c) as successful to the degree of accuracy which we can expect of the model. In particular the predicted $\Gamma^{1/3}$ dependence is not unrealistic. It is, however, difficult to test the precise form of this slow dependence on a limited data set. Further data on even shallower slopes might be more revealing in this respect.

It is also worth noting that slopes of practical interest may only be up to 1 in 10 or so ($\Gamma = 0.1$) which are therefore treatable within this framework.

A general insensitivity to the slope is noted by Britter et al. [8]. They however quote a dependence of the cloud velocity on the slope of $\sin\theta/\theta$ compared to our result of $(\tan\theta)^{1/3}$. Our methods are inappropriate to large

slopes, but clearly their expression cannot be valid close to $\theta = 0$, and so a direct comparison is difficult. It is made more difficult by the fact that our result is for a cloud of fixed volume and density, whereas Britter et al. [8] discuss the velocity of entraining clouds. There is scope for further work here.

5.2 Further comments

There are two possible ways of seeking further confirmation of the model, which we can contemplate here.

5.2.1 Development of integral models

One way is to combine the ideas above with a simple computerised model. Entrainment can be introduced in the usual way, although there is clearly some freedom about how exactly to do this. The simplest way of allowing for advection with the wind is to add the slope-generated velocity discussed here to the wind-advection velocity (vectorially). The predictions of such a model could be compared with a wider data-set. Let us emphasise, however, that this approach would be validating a whole combination of different aspects of the model, including entrainment as well as bulk motion, and therefore, whilst having its own benefits, loses some of the advantages of the simple test presented here. A combination of the two approaches is therefore desirable. We intend to pursue this avenue.

5.2.2 Further qualitative predictions of the model

The model presented here has two qualitative aspects which distinguish it from the results of other approaches. In principle these can be tested if appropriate data are obtained.

Firstly, the approach presented here gives rise to a picture of slumping followed by translation for a cloud released from a highish aspect ratio in calm conditions. (By "highish" we mean the régime discussed earlier where the cloud is tall relative to the drop in the slope, but still shallow.) This separation of slumping and translation contrasts with the slumping accompanied by downhill motion found in the models of Deaves and Hall [1] and Nikmo and Kukkonen [2]. In our approach this is a consequence of the boundary conditions: while the uphill edge depth and the downhill edge depth are the same, the uphill boundary will spread in the same way as the downhill one. The material will rearrange itself within the boundaries so that the centre of mass moves downhill, but only when the depth of the cloud is comparable with the drop in the slope over its length will the overall downhill translation become apparent. Ultimately the gravity spreading is predicted to stop, and any cloud growth will be due purely to the relatively slow process of entrainment. This is illustrated in a two-dimensional numerical solution of the shallow water model shown in Figs. 7(a–f). In this illustration the cloud is started off as close as possible to the parabolic-topped, flat-ground similarity solution variously described by Fanneløp and Jacobsen [5], Wheatley and Webber [4], Grundy and

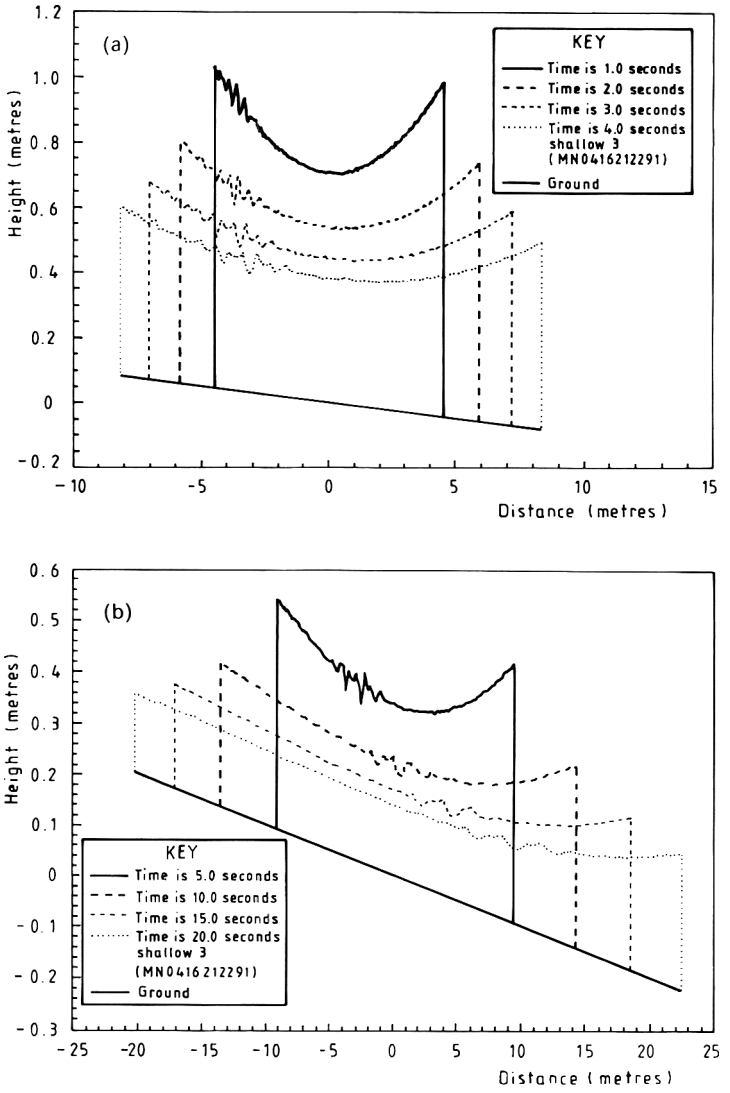

Fig. 7.(a, b). A cloud released from rest on a slope — in two dimensions. The cloud is released spreading in a way which would continue indefinitely in a self-similar way if the ground were flat. Differences from the symmetric self-similar flow begin to appear as the cloud aspect ratio becomes close to the gradient of the slope, but in this regime the cloud is largely unaffected by the slope.

Rottman [6] and Webber and Brighton [7]. This shows the onset of a significant deviation from the self-similar behaviour introduced by the slope, and the transition to the "wedge" behaviour described here.

Secondly, the cloud width predicted by the model is n times its overall length. Whilst exact confirmation of this is unlikely given the oversimplicity of

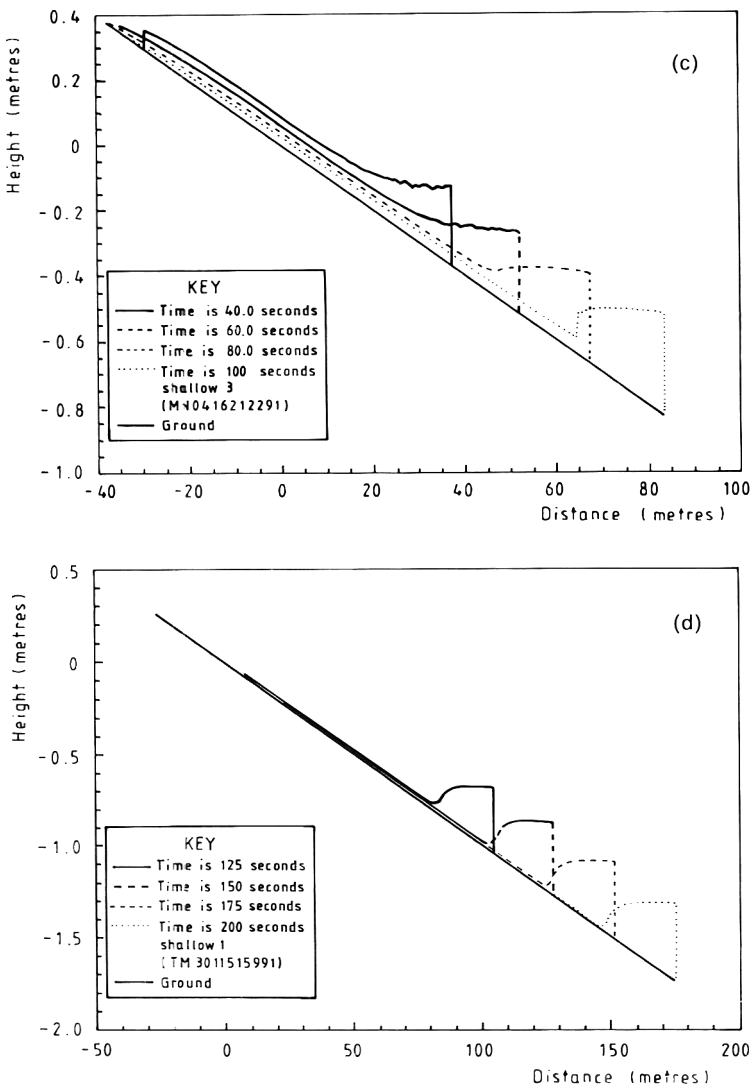

Fig. 7.(c,d). Continuing the flow from Figs. (7a,b) a hydraulic jump appears separating a "head" and a "tail" region. The slope is having a noticeable effect here, but this is a transition to the final regime.

some of our assumptions, any experimental visualisation of this flow which showed a cloud to be wide compared to its length would be an interesting support for this approach — we know *a priori* of no other reason why such a result should appear.

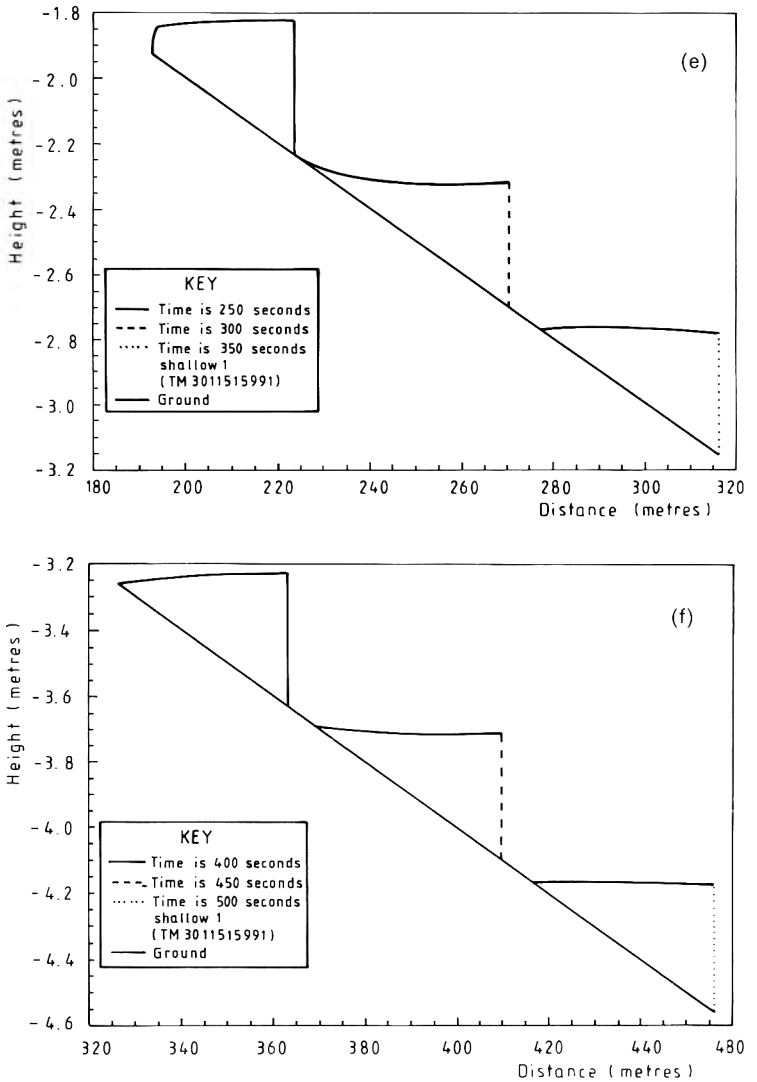

Fig. 7.(e.f). Continuing the flow from Figs. 7(a–d) in the final regime the hydraulic jump collapses and the cloud reaches the wedge shape which is moving down the hill but no longer spreading.

Acknowledgements

Financial support for the work presented here has come from the "STEP" programme of the Commission of the European Communities, from the UK Health and Safety Executive, and the Corporate Research programme of AEA Technology, all of which is gratefully acknowledged. We should also like to

acknowledge useful discussion with Dr. J. Kukkonen and Mr. J. Nikmo on the relative merits of, and problems with, our different approaches to this problem, and thank Mr. A. Mercer for his comments on the manuscript.

References

1 D.M. Deaves and R.C. Hall, The effects of sloping terrain on dense gas dispersion, J. Loss Prev. Process Ind., 3 (1990) 142–145.
2 J. Nikmo and J. Kukkonen "Modelling Heavy Gas Cloud Advection in Complex Terrain" Finnish Meteorological Institute preprint, Helsinki, 1991. (See also: A model for the advection of a heavy gas cloud on a slope, In: Proc. of the Int. Conf. and Workshop on Modeling and Mitigating the Consequences of Accidental Releases of Hazardous Materials, AIChE, New York, 1991 – ISBN 0-8169-0492-8, p. 655.)
3 S.J. Jones, D. Martin, D.M. Webber and T. Wren, The effects of natural and man-made obstacles on heavy gas dispersion — Part II: Dense gas dispersion over complex terrain, SRD Report SRD/CEC/22938/02, Culcheth, Warrington, 1991.
4 C.J. Wheatley and D.M. Webber, Aspects of the dispersion of denser-than-air vapours relevant to gas cloud explosions, Commission of the European Communities Report EUR 9592 En, CEC, Brussels.
5 T.K. Fanneløp and O. Jacobsen, Gravitational spreading of heavy gas clouds Instantaneously released, J. Appl. Math. Phys. (ZAMP), 35 (1984) 559–584.
6 R.E. Grundy and J.W. Rottman. The approach to self-similarity of solutions of the shallow-water equations representing gravity current releases, J. Fluid Mech., 156 (1985) 39–53.
7 D.M. Webber and P.W.M. Brighton, Inviscid similarity solutions for slumping for a cylindrical tank, J. Fluids Eng. 108 (1986) 238.
8 R.E. Britter. R.P. Cleaver and M.G. Cooper, Development of a simple model for the dispersion of denser-than-air vapour clouds over real terrain, British Gas Report MRS E 622, Midlands Research Station, Solihull, 1991.
9 M. Schatzmann, K. Marotzke and J. Donat, Research on continuous and instantaneous heavy gas clouds – Contribution of sub-project EV4T-00210D to the final report of the joint CEC projet. University of Hamburg, Meteorological Institute Report, Hamburg, 1990.
10 P.W.M. Brighton, A.J. Prince and D.M. Webber, Determination of cloud area and path from visual and concentration records, J. Hazardous Mater., 11 (1985) 155–178.

Journal of Hazardous Materials, 33 (1993) 123–141
Elsevier Science Publishers B.V., Amsterdam

Permeation measurements of chemical agent simulants through protective clothing materials[a]

Tarasankar Pal[b], Guy D. Griffin, Gordon H. Miller, Annetta P. Watson, Mary Lou Daugherty and Tuan Vo-Dinh[c]

Health and Safety Research Division, Oak Ridge National Laboratory[d], P.O. Box 2001, MS 6101, Oak Ridge, TN 37831-6101 (USA)

(Received November 26, 1991; accepted in revised form June 1, 1992)

Abstract

Effective procedures associated with storage and disposal of chemical warfare (CW) agents are important for the protection of civilian populations from inadvertent release of these agents. Emergency groups as well as citizens in surrounding communities need to know the relative effectiveness of various chemical protective clothing (CPC) ensembles in the unlikely event of such releases. A method has been developed for studying permeation of chemical warfare agent simulants through CPC materials. The experimental results characterize some commercially available CPC materials. Thirteen different CPC materials having widely differing compositions were chosen to study the permeation of four different liquid CW simulants (dimethyl methyl phosphonate, diisopropyl methyl phosphonate, malathion, and dibutyl sulfide) through these CPC materials at 25 °C. This permeation study involved a newly developed analytical technique employing room temperature fluorescence quenching of an indicator compound, phenanthrene, on filter paper. Various experimental factors such as breakthrough time, rate of permeation and uptake were investigated. On the basis of breakthrough time, the 13 CPC materials could be divided into three groups: most resistant, moderately resistant, and least resistant. Materials in the most resistant category exhibited no permeation by any of the simulants for at least 24 hours. Breakthrough occurred in the least resistant materials in generally less than an hour, and sometimes as soon as a few minutes.

Correspondence to: Dr. T. Vo-Dinh, Health and Safety Research Division, P.O. Box 2001, MS 6101, Oak Ridge National Laboratory, Oak Ridge, TN 37831-6101 (USA).

[a]Reference herein to any specific commercial product, process, or service by trade name, trademark, manufacturer, or otherwise, does not necessarily constitute or imply its endorsement, recommendation, or favoring by the United States Government or any agency thereof. The views and opinions of authors expressed herein do not necessarily state or reflect those of the United States Government or any agency thereof.

[b]Permanent address: Department of Chemistry, Indian Institute of Technology, Kharagpur, 721302, India.

[c]The submitted manuscript has been authored by a contractor of the U.S. Government under contract No. DE-AC05-84OR21400. Accordingly, the U.S. Government retains a nonexclusive, royalty-free license to publish or reproduce the published form of this contribution, or allow others to do so, for U.S. Government purposes.

Introduction

Congress has mandated that the United States shall destroy its stockpile of existing unitary chemical warfare weapons and bulk stocks of chemical agents incorporated into such weapons. This destruction is directed by the Department of Defense Authorization Act of 1986 (PL 99-145) which was subsequently amended to require completion of the disposal process by April, 1997. (The Army and Congress have recently announced that the current projected date of completion is 2004.) Although this action does not eliminate U.S. chemical warfare capability (binary agents are excluded), the amount of material to be disposed of, along with its extreme toxicity, make the task of disposal one which should be approached prudently. Chemical warfare agents to be disposed of are currently stored at eight separate locations in the continental U.S., in a variety of munitions [1, 2], as well as in bulk storage.

The method of choice for disposal of these agents is high-temperature (1130–1400 °C) incineration on-site at each stockpile location [1]. Although the probability is low that a release of chemical warfare agent might occur during the disposal process, the extreme toxicity of these chemicals raises concerns regarding protection of individuals in adjacent communities. Civilians in these communities are unlikely to have ready access to specialized military protective clothing ensembles, nor is it likely that all civilian emergency response groups in these neighboring communities would have such protection available to them.

Many types of chemical protective clothing (CPC) materials have been developed for protection against a wide variety of potentially hazardous situations, including accidental release of hazardous chemicals, via spills, fires, explosions, gaseous releases, etc. The pertinent question is how well would these various protective materials shield humans from exposure to chemical warfare agents. This research group has analyzed the available open-literature information regarding some commercial CPC materials in a previous publication [3]. This report has identified wide data gaps in the characterization of CPC materials for either chemical warfare agents or chemicals with sufficient structural similarity and physical properties to serve as reasonable surrogates (i.e., simulants). The research reported in the current paper is an initial attempt to seek answers to the question posed above as part of the technical assistance support that Oak Ridge National Laboratory is providing the Chemical Stockpile Emergency Preparedness Program (CSEPP).

The goal of this study is to assess the protective capacity of various clothing materials by investigating their permeability and uptake when they are exposed to various undiluted liquid simulants. Use of actual agent entails such a degree of hazard to the experimentalist that only a very few laboratories are certified as surety facilities and permitted to perform warfare agent experiments. Oak Ridge National Laboratory is not a surety facility. Thus it is common practice to employ the use of simulants, which mimic the chemical agents sufficiently well to provide useful data, but do not exhibit the extreme toxicity of live agents.

The question of what testing protocol provides the best indication of chemical resistance for a given protective material is an important one. Visible changes in material properties (e.g., swelling, blistering, etc.) provide only crude indications of the effect of the chemical on the protective material, and permeation of the chemical through the material may occur long before visible outward signs of degradation. This study investigates two important endpoints, viz., breakthrough time, defined as the time required for a detectable amount of chemical to diffuse through the CPC material; and permeation rate, which is a measure of amount of chemical permeating the material as a function of time. Breakthrough time provides an excellent parameter for comparison of the resistance of various CPC materials to a given test chemical, i.e., the longer the breakthrough time, the more resistant the CPC. The permeation rate is of less obvious application, but provides useful information about the physicochemical resistance of the CPC material to the test chemical. This study also investigated the effect of a one-hour immersion of each CPC material in each simulant to determine the uptake of simulant. Other studies have used this approach [4], and it can provide additional useful information regarding resistance of laminated materials to solvation, changes in physical properties of the protective material following contact with the chemical, etc. It is certainly not to be taken as a direct indication of protective material resistance, since total immersion does not at all mimic the intended application of the material (i.e., on normal application, only the resistant surface of the material is exposed to the chemical). Although this information is of interest, it should not receive primary consideration in rating the effectiveness of CPC resistance to chemicals. Of course, all these endpoints are influenced by many other parameters such as thickness of the protective material, concentration of the challenge chemical, temperature, etc. Some permeation studies utilizing chemical solvent or low-molecular weight organic compounds have been reported in the literature, but these do not directly or indirectly relate to the chemical warfare agents [3].

This paper describes the results of permeation studies using a new, simple and sensitive procedure recently developed at Oak Ridge National Laboratory [5] to evaluate the efficacy of CPC materials against CW agent simulants using room temperature luminescence quenching of an indicator compound (phenanthrene) on standard filter paper. The procedure tested thirteen protective clothing materials for permeation resistance to four different simulants. Breakthrough time, uptake of simulants by the materials, and permeation rate were determined at 25 °C.

Materials and methods

Chemicals

Tables 1 and 2 list the principal chemical warfare agents in the unitary stockpile and the compounds used as simulants for each. The two major

TABLE 1

Structural formulas and selected physical properties of chemical warfare agents

Parameter	Agent		
	GB	VX	HD
Chemical name (formula)	Isopropyl methyl phosphonofluoridate ($C_4H_{10}FO_2P$)	*O*-ethyl-*S*-(2-diisopropyl amino-ethyl) methyl phosphonothiolate ($C_{11}H_{26}NO_2PS$)	Bis(2-chloroethyl) sulfide ($C_4H_8Cl_2S$)
Structure	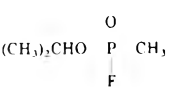	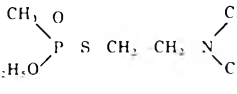	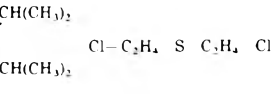
Molecular weight	140.1	267.4	159.1
Physical state (at room temperature)	Liquid	Liquid	Liquid
Boiling point	158 °C	298 °C	215–217 °C
Vapor pressure (25 °C)	2.9 mmHg	7×10^{-4} mmHg	0.11 mmHg

categories of stockpiled chemical warfare agents, nerve agents and blister agents [1] are represented in Table 1 by GB (sarin, a nerve agent), VX (nerve agent) and HD (variously called sulfur mustard, mustard gas, mustard, etc.). The simulant chemicals chosen were recommended by the sponsoring agency (Office of Assistant Secretary of the Army) and research staff of the Chemical Research Development and Engineering Center (CRDEC) at Aberdeen Proving Ground, MD. Tables 1 and 2 also list pertinent physical properties of agents and simulants. The various simulants were obtained from the following sources and used without additional purification: Diisopropyl methyl phosphonate (DIMP) (98% pure) (Johnson Matthey Electronics); dimethyl methyl phosphonate (DMMP) (technical grade) (Alpha Products); malathion (MAL) (96% pure) (K&K Fine Chemicals, Inc.); dibutyl sulfide (DBS) (96% pure) (Aldrich); phenanthrene, the detection chemical for the permeation studies, was obtained from Matheson Coleman and Bell.

CPC Materials

Thirteen different CPC materials were chosen as representative materials from a broad selection of generic classes (e.g., only one material composed of butyl/nylon/butyl laminate, one of Viton®[1] polyester/Viton laminate, even

[1]Viton® fluoroelastomer is a registered trademark of E.I. du Pont de Nemours & Co.

TABLE 2

Structural formulas and selected physical properties of simulants used in this study

Parameter	Simulant			
	DIMP	DMMP	MAL	DBS
Chemical name (formula)	(GB Simulant) Diisopropyl methyl phosphonate ($C_7H_{17}OP$)	(VX simulant) Dimethyl methyl phosphonate ($C_3H_9O_3P$)	(Organophosphorous pesticide) (Dimethoxy-phosphinothioyl) butanedioic acid diethyl ester ($C_{10}H_{19}S_2O_6P$)	HD simulant) ($C_8H_{18}S$)
Structure	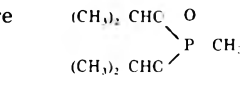	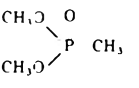	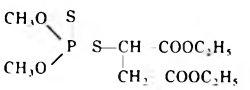	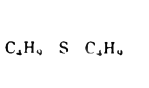
Molecular weight	180	124	330	146
Physical state (at room temperature)	Liquid	Liquid	Liquid	Liquid
Boiling point	66 °C (3 mmHg)	181 °C	156–157 °C	188–189 °C
Vapor pressure	—[a]	—	4×10^{-5} mmHg (30 °C)	—

[a] Not available.

though there could be several CPC materials made by different manufacturers employing the same fabric composition).

Table 3 (see Results Section) lists the various CPC materials tested, their manufacturer and nominal thickness of the various materials. A number of the materials are laminates, and are so indicated in Table 3 by naming the individual laminating layers of the laminate "sandwich" (as butyl/nylon/butyl). In the case of some materials, no information regarding composition or lamination was available, and the material is simply listed. Samples from gloves were taken from the palm of the glove; samples from sheet material were cut from the edge, and samples from protective suits were taken from the suit sleeves. Duct tape was added to the original list of 12 CPC materials due to its extensive use to seal suits to gloves and suits to footwear.

Experimental protocols

A. Breakthrough time studies

A 2.54-cm diameter circle of the CPC material was positioned over the open end of a glass vial (2.54 cm long with a 2 mL volume) containing approximately

1 mL of pure liquid simulant. A 1.0-cm circle of phenanthrene-treated (see Analytical Procedure Section) filter paper (Whatman 41) was centered over the bottle mouth on top of the material, and a second larger piece of filter paper acted to hold the 1.0-cm circle in contact with the material. This arrangement of bottle plus CPC plus indicator paper was mounted in a clamp (Fig. 1) to provide a seal between the CPC and the vial. To initiate a breakthrough measurement, the vial was inverted so that the liquid simulant contacted the outside surface of the CPC sample.

A series of specially designed exposure cells using glass vials [5] were set up and inverted at the same time. After selected intervals, individual vials were returned to the upright position, the clamp was loosened, and the indicator paper was removed and analyzed. Figure 2 schematically shows the principle of the fluorescence quenching technique. The time interval at which individual vials were selected for measurement varied considerably, depending upon the speed with which the simulant penetrated the CPC material. For extremely resistant materials, the sampling interval might be 1 h or more, while for easily permeable materials, sampling intervals of 30 s to 1 min were used. For a particular simulant, the first vial which showed a quenching of the fluorescence of

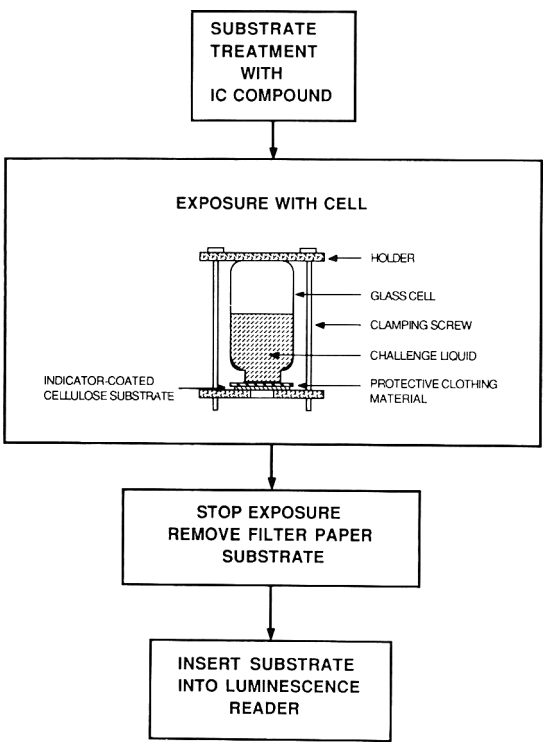

Fig. 1. Experimental apparatus schematic for breakthrough and rate of permeation study and schematic for fluorescence measurements (IC = indicator compound).

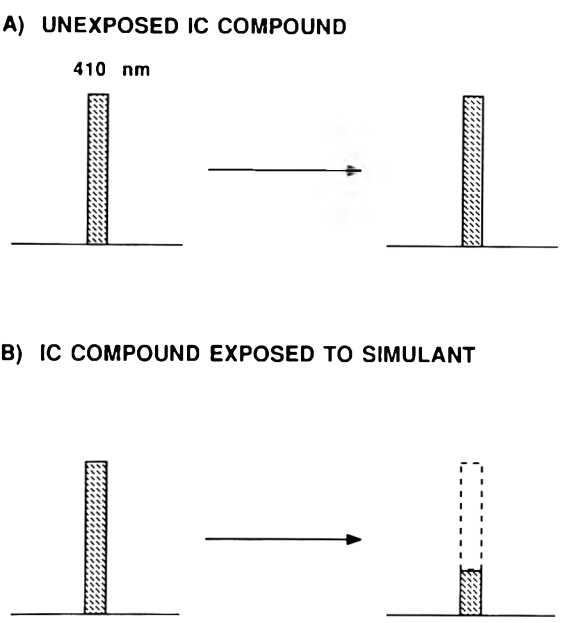

Fig. 2. Principle of the fluorescence quenching technique: (A) Representation of fluorescence emission of phenanthrene (10^{-2} *M*) coated filter paper, excited at 352 nm and having a fluorescence maximum at 410 nm. (IC = indicator compound); (B) Representation of fluorescence intensity decrease of the phenanthrene-coated paper following exposure to simulant.

the indicator paper (see Analytical procedure Section) was taken as the "breakthrough vial." The time at which this vial was sampled was therefore the breakthrough time. Each breakthrough time indicated in Table 3 was the average value of triplicate experiments. In the case of a few CPC materials, there was significant adhesion of the indicator paper to the CPC. In these circumstances, the indicator paper was analyzed on the opposite side from that which contacted the CPC (see Analytical procedure Section). Breakthrough times given in Table 3 as greater than some set time (e.g., > 24 h) correspond to solutions where the indicator paper/CPC sandwich left in contact with the chemical for the indicated period of time provided no measurable evidence of chemical contact during the period of 24 h observation.

B. Permeation rate studies

The basic experimental protocol consisted of measuring breakthrough (if any) of simulants after specific time intervals. The experimental set-up was the same as for the breakthrough time studies described above. A series of replicate exposure cells were all inverted at the specific time intervals following exposure. The indicator papers were removed from these vials and analyzed. A curve was constructed in which the amount of chemical which penetrated

the CPC material was plotted as a function of time after initial breakthrough. Each experiment was carried out in triplicate, and the curve was constructed using average values.

C. Uptake studies

A 0.6-cm diameter circle of the CPC material was placed into 1 mL of the chemical simulant in a closed vial for 1 h [5]. The disc of CPC material was accurately weighed before and after immersion and the weight gain was considered an estimate of simulant uptake. In addition to this measurement, the change in physical characteristics of the CPC material following immersion was noted along with any other observations (e.g., leaching of colored dyes/adhesives from the CPC material).

D. Analytical procedure

The analytical procedure developed for these permeation studies is described in detail in a previous report [5]. Briefly, Whatman No. 41 filter paper (11 cm circles) was treated with 1.25 mL of 1×10^{-2} *M* phenanthrene in ethanol and dried at room temperature. This served as our indicator paper. Following the simulant exposures as described above, the indicator paper circles were removed and directly analyzed for fluorescence. No chemical extraction was necessary for the analysis. This procedure therefore avoids the cumbersome separation techniques that would be required for a gravimetric (classical) analysis.

All fluorescence measurements were made using a Perkin-Elmer Model MPF-43A fluorescence spectrophotometer equipped with a 150-W xenon excitation source. To prepare exposed filter paper samples for measurements, the discs were mounted on a sample holder previously designed for surface emission measurements [6]. The indicator paper in the sample holder was transferred to the spectrofluorometer sample compartment for fluorescence measurement. All four simulants quenched phenanthrene fluorescence, but did so to differing extents (e.g., MAL caused the greatest degree of quenching, for a given concentration compared to equal concentrations of the other 3 simulants). Figure 2 illustrates the effect of MAL on the phenanthrene fluorescence. For a given simulant, the extent of fluorescence quenching on the indicator paper was related to the amount of simulant which had been absorbed by the paper. In this study, calibration curves for each simulant have been established, indicating a direct relationship between simulant concentration and fluorescence quenching. Figures 3 and 4 illustrate examples of calibration curves for DIMP and DBS. Note that there appears to be a linear relationship between the extent of fluorescence quenching and the concentration of simulant when this concentration is expressed logarithmically.

This fluorescence quenching procedure developed in this work was found to exhibit excellent sensitivity for detecting simulants. It is noteworthy that this

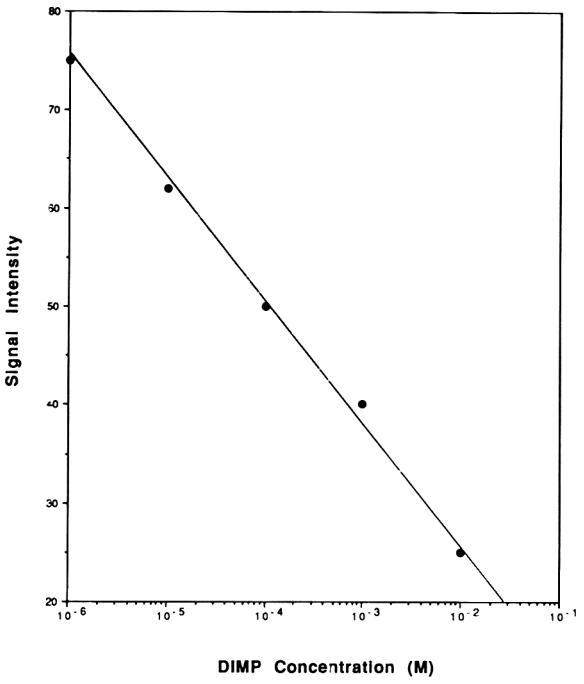

Fig. 3. Calibration curve for DIMP, using the fluorescence quenching of phenanthrene (see Experimental protocols, Section D). Aliquots of 2 μL of DIMP, over the concentration range of 10^{-2} *M* to 10^{-6} *M* (diluted in ethanol) were added to the phenanthrene-treated paper, the paper was dried and the fluorescence was determined.

new quenching technique has been developed because a direct fluorescence measurement method cannot be used; CW agents and simulants are not fluorescent compounds such as polycyclic aromatic species [7]. The limits of detection for MAL, DIMP, DBS, and DMMP were found to be: 10^{-12} *M*, 10^{-6} *M*, 10^{-5} *M* and 10^{-6} *M*, respectively. This level of sensitivity allows one to readily detect very small amounts of simulant permeating the CPC. It should be emphasized that, in addition to phenanthrene, a wide variety of compounds (e.g., pyrene, naphthalene, anthracene, emodin, indole, fluorescein and diphenylamine) were also tested as possible indicator compounds. Only the fluorescence of phenanthrene was found to be uniquely quenched when exposed to any of the four simulants. Phenanthrene is a highly fluorescent compound, and there have been several studies in which investigators have examined the quenching of phenanthrene fluorescence by other chemicals [8, 9]. However, the effect of these particular chemicals on the fluorescence of phenanthrene has not been reported previously.

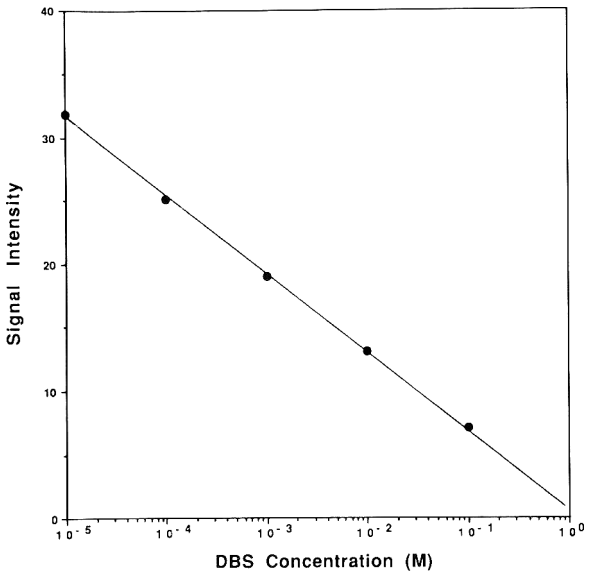

Fig. 4. Calibration curve for DBS, using the fluorescence quenching of phenanthrene (see Materials and methods, Section D). Aliquots of 2 μL of DBS, over the concentration range of 10^{-1} *M* to 10^{-5} *M* (diluted in ethanol) were added to the phenanthrene-treated paper, the paper was dried, and the fluorescence was determined.

Results and discussion

Breakthrough times

The CPC materials tested displayed a variety of responses when tested for breakthrough time with the four chemical simulants (Table 3). Each of the simulants was tested undiluted, i.e., neat. Breakthrough time can serve to reflect relative estimates of protection provided by protective clothing [4, 5]. It is apparent that the CPC materials can be grouped into three categories, depending on the time required for breakthrough. The materials affording the highest degree of protection were CPC materials #9–13. For each of these materials, breakthrough times were in excess of 24 h, i.e., the test was carried out for at least 24 h, after which the test was terminated. In the case of CPC material #12, no breakthrough was detected even after 100 hours of exposure. The composition of the laminated fabric, and its thickness probably both contribute to the observed degree of chemical resistance. It is noteworthy that the thicknesses of materials #9–13 were greater than that of other CPC materials. Thickness alone, however, is not the most important criterion. It appears that laminates containing Teflon®[2] exhibit excellent resistance (see

[2]Teflon® is a registered trademark of E.I. du Pont de Nemours & Co.

TABLE 3

Breakthrough times of simulants through chemical protective clothing (CPC) materials

	CPC Material	Thickness	DIMP[a]	DMMP[a]	MAL[a]	DBS[a]	Supplier
1.	PVC/nylon/PVC (305 PVC/BA)	17 mil	10 min	4 min	3 min	4 min	Fyrepel Products Newark, OH
2.	Neoprene plastic glove	No data	45 min	15 min	10 min	10 min	International Playtex, Inc. Stamford, CT
3.	Tyvek® (Saranex®-coated)	8 mil	30 min	50 min	12 min	90 min	Kappler Safety Group Guntersville, AL
4.	Butyl nitrile glove (Pioneer Gatorhide)	No data	60 min	45 min	50 min	55 min	Pioneer Industrial Products Willard, OH
5.	Barricade® chemical barrier fabric	21 mil	50 min	80 min	90 min	60 min	Kappler Safety Group Guntersville, AL
6.	Tyvek QC, Polyethylene-coated	6 mil	105 min	40 min	30 min	30 min	E.I. du Pont de Nemours & Co., Inc. Wilmington, DE
7.	Viton® polyester/Viton (305 V/BA, 306 V/BA)	9 mil	140 min	140 min	> 100 h	> 100 h	Fyrepel Products Newark, OH
8.	Duct tape	10 mil	210 min	210 min	> 24 h	> 7 h	Armco Company Michigan City, IN
9.	Butyl/nylon/butyl (305 B/BA, 306 B/BA)	16 mil	> 24 h	> 24 h	> 24 h	> 24 h	Fyrepel Products Newark, OH
10.	Butyl/polyester/chloroprene (Chempruf™ II)	19 mil	> 24 h	> 24 h	> 24 h	> 24 h	Mine Safety Appliances Pittsburgh, PA
11.	Thf/Mws/Thf[b] ("First Team"™)	No data	> 24 h	> 24 h	> 24 h	> 24 h	Mine Safety Appliances Pittsburgh, PA
12.	Teflon® Kevlar® Teflon (Force Field™)	17 mil	> 100 h	> 100 h	> 100 h	> 100 h	Fyrepel Products Newark, OH
13.	Teflon/fiberglass/ Teflon	10 mil	> 24 h	> 24 h	> 24 h	> 24 h	Chemical Fabric Corp. Merrimack, NH

[a]DIMP = Diisopropyl methyl phosphonate (GB simulant); DMMP = Dimethyl methyl phosphonate (VX simulant); MAL = Malathion (organophosphorus insecticide and generic nerve agent simulant); and DBS = Dibutyl sulfide (sulfur mustard simulant).
[b]Thermoplastic film/non-woven composite substrate/thermoplastic film.

materials #12–13). There are other laminate compositions, however, which also exhibit excellent resistance (i.e., butyl/nylon/butyl or butyl/polyester/chloroprene).

There is another group of CPC materials (Table 3) which exhibit relatively good resistance to one or more of the chemical simulants (materials #4–7). In general, these materials resisted simulant breakthrough for at least 1 h. Note that the Viton/polyester/Viton (material #7) provided excellent resistance to MAL and DBS. It is also important to note that CPC material #6 (Tyvek®[3], polyethylene coated) did not show strong resistance against MAL and DBS. Note the different behaviors of materials #6 and #3. Even though both are Tyvek, they show differences in resistance to different simulants (see Table 3), perhaps due to differences in the coating material used over the Tyvek.

The last group of CPC materials in (materials #1–3) investigated in this study are those materials which exhibit poor chemical resistance (Table 3). With one exception, breakthrough occurred in less than 1 h. In the case of the PVC/nylon/PVC laminate, breakthrough occurred in a matter of a few minutes. It is also interesting to compare the chemical resistance of the two glove materials tested against this battery of chemicals. The material #2, commonly called Playtex™[4], is widely used for domestic glove material in the kitchen and bath, while the butyl nitrile material is widely used in the chemical industry. Because of the extensive availability of Playtex, this material could be used for very short-term expedient protection. However, in our experimental system, the resistance to permeation of butyl nitrile is superior to that of Playtex. The butyl nitrile material provides a three-fold longer breakthrough time for DMMP, compared to Playtex, and a five-fold longer breakthrough time for MAL and DBS.

Also note that a special duct tape has been tested in the experimental assay. This duct tape is commonly used by hazardous material response teams to provide a seal between the protective suit and gloves, or around ankles to seal the suit to footwear. The experimental assay tested only one of many brands of duct tape, so the data cannot be used to evaluate the relative merits of different brands. The one particular brand tested demonstrated good resistance to the chemical simulants. As can be seen from Table 3, duct tape resists permeation of MAL and DBS for >24 h and >7 h, respectively. For the compounds DIMP and DMMP, duct tape provides greater resistance to breakthrough than CPC materials #1–7. Duct tape was one of the thinner materials tested (10 mil[5] vs. 19 mil maximal thickness for material #10).

Rate of permeation studies

This section briefly discusses data related to the permeation rate, which refers to how rapidly the chemical simulants diffuse through the CPC

[3]Tyvek® spun-bonded olefin is a registered trademark of E.I. du Pont de Nemours & Co.
[4]Playtex™ is a trademark of International Playtex, Inc.
[5]1 mil $= 2.54 \times 10^{-5}$ m.

materials. This rate measurement provides a quite different index of CPC effectiveness against the simulants than breakthrough time. For some CPC materials, as the simulant begins to permeate the material, the resistance to permeation of the material changes. (In fact in certain instances, evidence of dissolution of CPC material constituents was seen, in that simulant solutions became colored, presumably with the material dye.) Therefore, by examining the slope of the rate of permeation curve, one can deduce valuable information about how the simulant affects the permeability of the material. Figure 5 shows an example of a permeation rate curve (DIMP against butyl nitrile) where the slope is initially very shallow, and then after 80 min, the slope increases dramatically. This behavior is in contrast to the curves of Figs. 6–9, where the slope is very steep. Representative curves showing the rate of permeation through various CPC materials by chemical simulants are shown in Figs. 6 through 9. In Figs. 6 and 7, we compare the rate of permeation of DIMP through material #1 (poor resistance) and material #7 (good resistance). In both cases, the steepest portion of the permeation curve shows the time at which maximum change in permeability occurs. Almost all of the permeation curves which we have generated exhibit a breakthrough time characterized by a rapid change in permeability with time. For material #1,

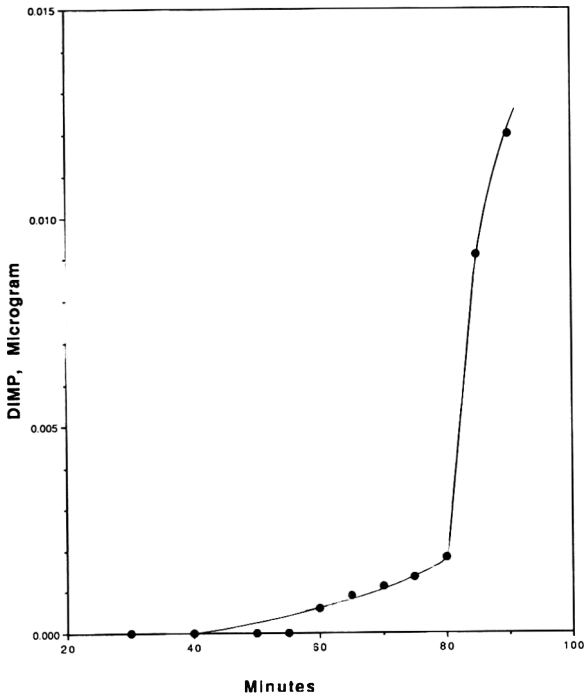

Fig. 5. Rate of permeation of DIMP through butyl nitrile glove material (#4, Table 3) (see Materials and methods for description of procedure).

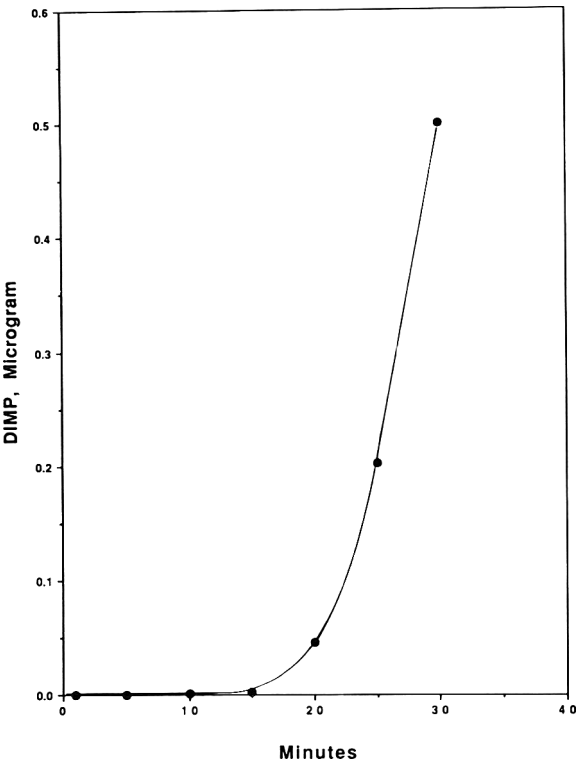

Fig. 6. Rate of permeation of DIMP through PVC material (#1, Table 3).

this change occurs about 15–20 min after initial breakthrough. For the resistant material (#7), the maximal permeability change occurs 20–30 min after initial breakthrough. This difference in time of maximal permeability change is probably consistent with the greater resistance to simulant permeation demonstrated by material #7. It is noteworthy that the permeation curves appear to level off after a steep increase. This effect could be due to saturation process of the detection system (i.e., the indicator-coated substrate became saturated with the simulations and could not absorb rapidly enough more simulant penetrating through the materials). Figures 8 and 9 exhibit some representative results of permeation rates of MAL through the two glove materials (#2 and #4) tested. In the case of the neoprene glove material, the maximal rate of change was measured after 20 min. These data may be of interest to workers who handle pesticides, as it demonstrates differences in permeability rates among two common commercial glove materials. This study has produced a large number of permeation curves for all combinations of simulant/CPC material. Although general conclusions from this wealth of data cannot readily be made, important and useful information can be derived from this study. The experimental results indicate that the breakthrough time could

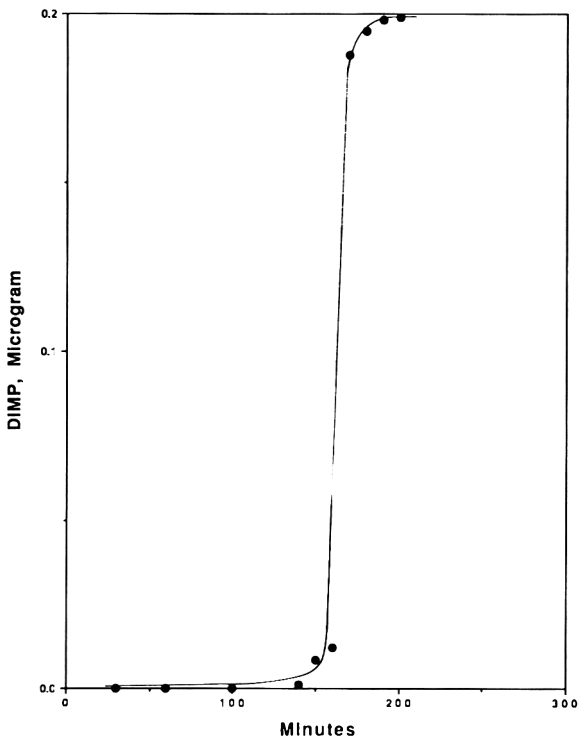

Fig. 7. Rate of permeation of DIMP through Viton laminate (#7, Table 3).

be used as a parameter for relative comparisons of CPC protection. Because most of the rate of permeation measurements show a rapid permeation of the simulant within a relatively short time of initial breakthrough, comparisons based on this parameter provide only qualitative differentiation regarding the effectiveness of the CPC materials tested.

Uptake studies

Table 4 presents the results of uptake studies, where a swatch of CPC material was immersed in undiluted simulant. Although certain immersion studies might take days to show detectable effects, our studies were limited to 1 h. The results from the uptake studies may have some relevance to the chemical protection afforded by the materials tested. However, it is noteworthy that, in the uptake studies, chemical impinges on the inside of the material as well as the outside, while in actual use, only the outside is intended to receive chemical exposure. Even more significantly, the process of cutting a small swatch of material to be immersed in a simulant solution for the uptake study results in exposed edges, which would be expected to exhibit little or no resistance to chemical permeation. Therefore, the uptake data can provide only qualitative information on physical changes of the materials immersed in

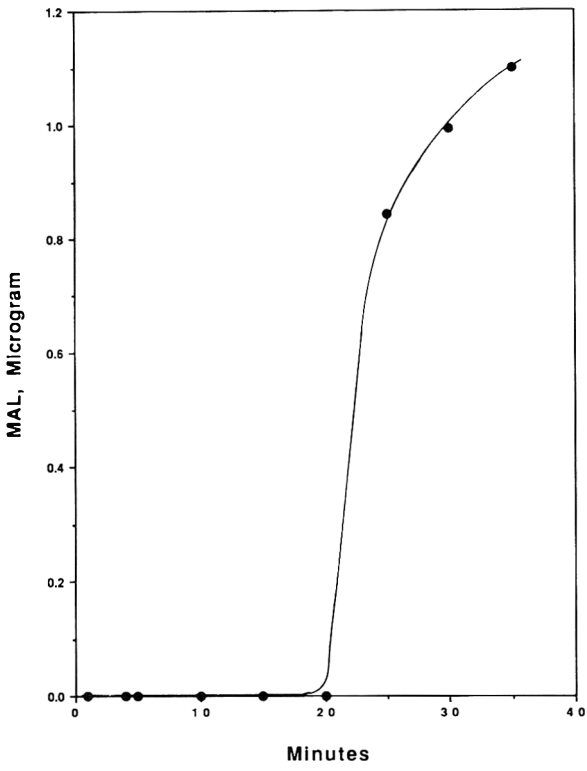

Fig. 8. Rate of permeation of malathion through neoprene glove material (#2, Table 3).

TABLE 4

Uptake of liquid simulant by CPC materials: 1 h study[a]

CPC material	Liquid (g/cm^2)			
	DIMP	DMMP	MAL	DBS
1. PVC/nylon/PVC	—[b]	0.00686	0.00410	0.00166
2. Neoprene plastic glove	0.01329	0.00413	0.00349[c]	0.09487
3. Tyvek®, Saranex®-coated	0.00486	0.00541	0.00592	0.00614
4. Nitrile glove	0.10028	0.00682	0.3163	0.00483
5. Barricade®	0.00404	0.00436	0.00737	0.00449
6. Tyvek QC	0.00426	0.00754	0.00491	0.00511
7. Viton®/polyester/Viton	0.04897[d]	0.0110	0.00128	0.00038
8. Duct tape	—[e]	—[f]	—[e]	—[e]
9. Butyl/nylon/butyl	0.00167	0.00153	0.00201	0.03036
10. Butyl/polyester/chloroprene	0.00859	0.00351	0.02033	0.02033
11. Thermoplastic film	0.01012	0.00914	0.00798	0.00798
12. Teflon®/Kevlar®/Teflon	0.01598	0.01398	0.00994	0.00994
13. Teflon/fiberglass/Teflon	0.00127	0.00209	0.00118	0.00118

[a]0.86625 cm^2 of CPC material used.
[b]Disintegrated.
[c]CPC material expanded in two dimensions.
[d]Embrittlement and shrinkage.
[e]Adhesive dissolved; weight decreased.
[f]No significant change.

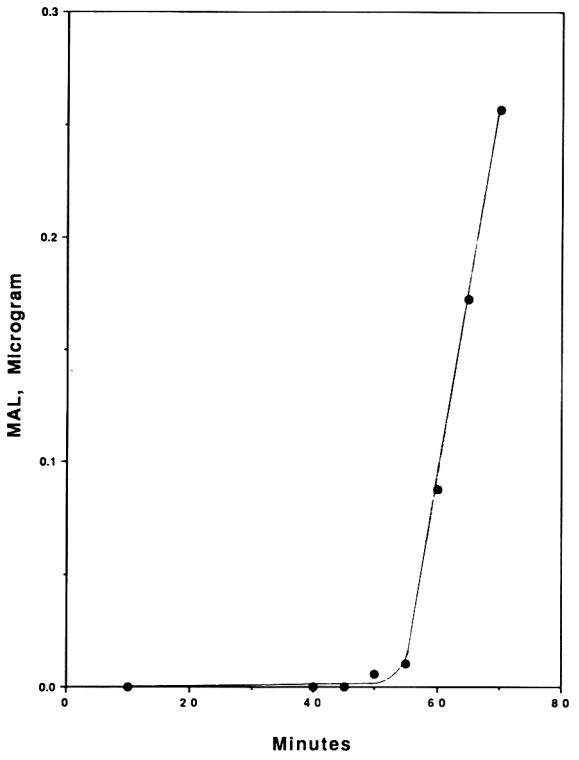

Fig. 9. Rate of permeation of malathion through butyl nitrile glove material (#4, Table 3).

simulant solutions. Among these changes we note the following. Material #1 disintegrated in DIMP, i.e., was reduced to a powder. Material #2 (Playtex glove) swelled in DBS without apparent disintegration. This effect was not seen with the other glove material (#4). Material #7 showed embrittlement and shrinkage in DIMP. Duct tape was found to undergo a weight loss upon immersion in DIMP, MAL and DBS, presumably due to dissolution of the adhesive. It is worth mentioning the importance of these uptake studies since they provide useful qualitative indications regarding physicochemical stability on the various materials.

Conclusions

The experimental results of this work have produced many important conclusions on permeation properties of a wide variety of protective materials. The data indicate that some commercially available CPC materials provide excellent protection against permeation by the chemical warfare agent simulants evaluated. The most useful comparisons of the relative effectiveness

of the various materials are provided in Table 3. Materials #9–13, (viz., butyl/nylon/butyl, butyl/polyester/chloroprene, thermoplastic film, Teflon/Kevlar®[6]/Teflon, and Teflon/fiberglass/Teflon) all exhibited good resistance to permeation of the simulants (i.e., breakthrough times >24 h). All these materials are laminates and two of these utilize Teflon as a laminating material. The effectiveness of the other CPC materials tested against permeation by the simulants varied considerably, but no other material demonstrated the consistency of resistance toward all four simulants as demonstrated by materials #9–13. Duct tape exhibits reasonable resistance to permeation by the four simulants, although its resistance to DIMP (210 min) and DMMP (210 min) was not as good as its resistance to MAL (>24 h) and DBS (>7 h). Due to its wide availability, duct tape appears to be a useful expedient material to provide at least a temporary seal against permeation by the agents.

It should be emphasized that all these results were obtained during simulant challenge and should be confirmed with the unitary agents themselves. Although the authors expect that the agents will behave similarly to the simulants, this might not be true for a particular CW agent/CPC material combination. It is noteworthy that both permeation and penetration (of simulant through the pores of the materials) combined to account for the flow of liquid penetrating through the polymer. The results of this study do not distinguish between penetration and permeation but provide an overall parameter that can be related to the protective characteristics of the materials tested.

Finally, this work deals with an important application of a new analytical technique for permeation study of chemical agents and simulations through protective materials. The analytical technique, which is based on spectral modification of fluorescence, demonstrates high sensitivity, reproducible results, and simplicity. These features make it an attractive choice for future permeation studies of field monitors for protective garments.

Acknowledgements

This report was sponsored by the U.S. Department of the Army, Office of the Assistant Secretary, Installations (Logistics and Environment), under Interagency Agreement DOE No. 1769-1354-A1 and FEMA, Office of Natural and Technological Hazards, Federal Emergency Management Agency under Interagency Agreement No. 1457-B106-A1. All authors are employed by Martin Marietta Energy Systems, Inc. at Oak Ridge National Laboratory, operated for the U.S. Department of Energy under contract DE-AC05-84OR21400. The authors thank the following individuals for generously providing material samples: Ms. Joy Wagner, Fyrepel/Lakeland Ind.; Ms. Linda Muir, Chemical

[6]Kevlar® aramid fiber is a registered trademark of E.I. du Pont de Nemours & Co.

Fabrics Corp.; Mr. Larry Gallagher, E.I. du Pont de Nemours & Co.; Mr. Gary Pryor, Safety Equipment Distributing Co.; Mr. Jim Frazee, Mine Safety Appliances.

References

1 S.A. Carnes, Disposing of chemical weapons: a desired end in search of an acceptable means, Environ. Prof., 11 (1989) 279–290.
2 S.A. Carnes, and A.P. Watson, Disposing of the U.S. chemical weapon stockpile: an approaching reality, J. Am. Med. Assoc., 262 (1989) 653–659.
3 M.L. Daugherty, A.P. Watson and T. Vo-Dinh, Currently available permeability and breakthrough data characterizing organophosphates and warfare agent simulants in civilian protective clothing materials, J. Hazardous Mater. 30 (1992) 243–267.
4 N. Vahdat, Permeation of polymeric materials by toluene, Am. Ind. Hyg. Assoc. J., 48 (1987) 155–159.
5 T. Vo-Dinh and T. Pal, Development of a fluorescence quenching technique to detect permeation of chemical agent simulants through protective clothing materials, Appl. Spectrosc., 46 (1992) 677–681.
6 T. Vo-Dinh, Room Temperature Phosphorimetry for Chemical Analysis, Wiley, New York, 1984.
7 T. Vo-Dinh, (Ed.), Chemical Analysis of Polycyclic Aromatic Compounds, Wiley, New York, 1989.
8 D.R. Haynes, K.R. Helwig, N.J. Tro and S.M. George, Fluorescence quenching of the phenanthrene excimer on aluminium oxide, J. Chem. Phys., 93 (1990) 2836–2847.
9 J. Karpiuk and Z.R. Grabowski, Mechanism and kinetics of fluorescence quenching of aromatic hydrocarbons by a stable nitroxyl radical, Chem. Phys. Lett., 160 (1989) 451–456.

Journal of Hazardous Materials, 33 (1993) 143–154
Elsevier Science Publishers B.V., Amsterdam

Book Reviews

Landfill, by Stuart Finley, Inc., 3428 Mansfield Rd, Falls Church, VA 22041, 16 mm sound color movie, 12 min, available on loan or purchase, $175.

Solid waste (once known as household refuse) has become a serious problem in many areas. Properly engineered, operated and supervised landfills can be important parts of the environment as well as presenting little real contamination or threat to residential health. The purpose of a sanitary landfill is to protect the environment; no air pollution is created; water pollution through leaching or eroding can be controlled and monitored. The I-95 Landfill in Northern Virginia, which serves as the landfill for the million people who reside in the District of Columbia is shown in detail. No chemical control is noted; that is covered by other films and tapes. The film is an excellent introduction to the how and why of proper landfill practices especially for residents who live nearby.

HOWARD H. FAWCETT

Hazardous Waste Options, produced for the U.S. Environmental Protection Agency by Stuart Finley, Inc., 3428 Mansfield Rd, Falls Church, VA 22041, 1981, 22 min, 1/2 inch VCR tape or 16 mm movie, available from Finley.

Although produced several years ago, this production, either as film or video tape, contains the fundamentals of disposal methods and procedures in use today. Its purpose is to dispel tensions about hazardous waste problems and programs by explaining modern hazardous waste technology in a direct manner. Photographed at the facilities of nine major hazardous waste service companies, the narration discusses recycling and recovery, hazardous waste treatment and disposal, and recovery of valuable materials. Landfilling (with proper safeguards), high temperature incineration for both liquids and solids, deep well injection, ground water monitoring, and testing are noted. This film is timely and appropriate for general citizens' groups, as well as for training industrial personnel who handle and dispose of hazardous wastes.

HOWARD H. FAWCETT

Propane, Butane, Propylene, by Emergency Film Group, Plymouth, MA, Hazardous Chemical Series No. 9, 29 min, $395.00.

This well done, beautifully photographed video is designed for emergency response groups, especially fire departments. The tape jacket notes that the following topics are covered:

- Why allowing a fire to burn may be the best tactic
- Water flow rates for cooling tanks exposed to fire
- Boiling liquid expanding vapor explosions
- Monitoring instruments for LPG (liquified petroleum gases) emergencies
- Fire safety analysis for LPG emergencies
- Requirements for safe storage areas
- Controlling vapors with water fog
- ASME and DOT container types
- How vapors behave

The film begins with an introduction to drilling for gas and oil, and a description of how liquified petroleum gas is derived and used. The gases, as noted, have wide use but can be very dangerous as a result of their flammability and explosion potentials.

Propane is discussed first. Propane has a wide variety of uses in the home, for vehicle fuel and as an industrial raw material. The second chemical discussed in the video is butane. It is used as a propellant, refrigerant, chemical feedstock and fuel. Propylene, the third chemical illustrated in the video, is a man-made gas used mainly in the industrial chemical industry.

Propane is odorless and colorless, but sulfur-containing organic chemicals are added as odorants. The LEL and UEL of the gas are approximately 2% and 10%, respectively. Burning temperatures exceed 3500°F. LPG is normally stored as a liquid under pressure. Once released, it expands rapidly to a ratio of 270:1 and through moisture condensation may cause a white water fog. Being heavier than air, the gas may hug the ground. All three gases in the liquid state will float on water and boil.

All three gases have an NFPA flammability rating of 4, the highest level, and a BLEVE can occur with fire-exposed containers. The NFPA health classification of all three gases is 1, indicating a material that is an irritant but having only mild residual injury. All three compounds, however, are asphyxiants as a result of their excluding oxygen.

The NPEA reactivity rating for propane and butane is 0, indicating materials that are normally stable and nonreactive with water. The NFPA rating for propylene is 1, indicating a normally stable material which may become unstable at higher temperature. Propylene also reacts violently with nitric acid and other oxidizers.

Storage areas and safety considerations thereof are described on the video. NFPA or API standards should be followed where inside storage is severely limited. The fire protection needs of large storage facilities are described.

Areas in which these gases are stored, the video notes, should be fenced. Proper safety equipment is described and unloading and loading operations are shown — it is noted that the escape of small amounts of gas cannot be avoided, so all sources of ignition must be avoided.

The video shows a devastating fire in Buffalo, New York, which resulted from a 500 gallon propane tank illegally being used as a storage tank in a building. While being moved, the tank fell and sheared off the valve. The resulting fire and explosion, and the fire ball ended in the destruction of 18 buildings and damage to 55 other buildings as well as the deaths of seven people, five of them the first-arriving fire-fighters. Twenty-five other fire-fighters were injured.

Fortunately, most incidents involving these gases are not so catastrophic. Typical spills only involve small amounts of these gases — generally during transfer operations as a result of overfilling or accidents involving LPG-fueled vehicles.

Having described the problem, the video goes on to describe the safe response techniques for fire fighters — upwind, observation from a distance, use of turnout gear, identification of the hazardous chemicals, and size and shape of storage containers, i.e. DOT portable cylinders and large shipping containers (trucks, railcars).

DOT numbers for these flammable gases (red DOT placed) are:

- LPG - 1075
- propane - 1978
- butane - 1011
- propylene - 1077

Shipping papers should generally show "liquified petroleum gases" for all of the chemicals.

In response situations, odor, it is noted, cannot be relied upon for detection of the gas as the odorant may have been adsorbed by the soil or may have deadened the respondents' sensory organs. Gas meters should be used to measure gas concentrations; respondents should not rely upon the nose.

The emergency response procedures for LPG-exposed victims are given. The importance of prevention of source ignition (including responding vehicles) is noted. How to disperse a cloud using water fog is described. How to stop leaks is described with the admonition to do it carefully. Response to flame-involved containers is discussed — with the potential of a BLEVE emphasized. Fire resulting from leaks, it is said, should not be extinguished unless the leak can be stopped. A controlled burn may be preferable. Signs of BLEVE — bulge in the tank, increased noise, increased volume of fire — are noted. As a final note, decontamination procedures are described.

Although not a fire-fighter, this reviewer does teach a course on hazardous chemical spills. My review of the video leads me to believe that very little of

importance was missed. The material was well written and well photographed. It is an excellent training aid.

GARY F. BENNETT

International Directory of Emergency Response Centres, OECD Environment Monograph No. 43, UNEP-1F/PAC Technical Report Series No. 8, United Nations Environment Programme, 1991, 77 pp., Free.

Listed are all the agencies, both governmental and private. This provides assistance and/or information for chemical spill response. Beginning with Brazil and ending with the United States, data are given for:

- telephone number
- telefax/telex
- address
- type of institution
- length of service
- name of contact
- fee
- information provided
- other services

GARY F. BENNETT

Environmental Chemistry, by Nigel J. Bunce, Wuerz Publishing Ltd, 895 McMillan Ave., Winnipeg MB R3M 0T2, Canada, 1991, ISBN 0-920063-46-2 (pbk), 340 pp. $33.00; plus answer guide, ISBN 0-920063-38-1, 343 pp., $US17.00 (shipping rate $5 per order).

This is an unusually well organized and written book, nicely illustrated with photographs and diagrams, by Professor Bunce of the Chemistry Department of the University of Guelph. Intended as a introductory textbook for chemistry and biology students, it assumes the reader has studied chemistry and biology, as well as being reasonably fluent in mathematics.

The present status of studies in environmental chemistry are discussed in detail, with updated references and opinions which reflect a understanding not always seen in books of this nature. Starting with the earth's atmosphere, the text progresses on to stratospheric ozone, tropospheric chemistry, indoor air quality and remedial measures to improve it, natural waters, acid rain, drinking water, sewage and waste disposal, chlorinated organic compounds, and environmental metals. Each chapter and section includes questions (that are answered in the answer guide) and 500 references to current literature, as well as presenting background history where appropriate.

The cover photograph of the thirteenth century statue in Salisbury Cathedral, England, and the blue haze scene which illustrates the role of terpene aerosol pollution in the Great Smoky Mountains of Tennessee should convince even the cynical that such problems are real and significant. The book should have wide appeal, especially in schools and colleges which are supplementing chemistry, biology and mathematics courses with "real world" issues. It deserves wide circulation.

HOWARD H. FAWCETT

Fate of Pesticides and Chemicals in the Environment. by J.L. Schnoor (Ed.), John Wiley and Sons, New York, NY 10158, 1992, ISBN 0-471-50232-4, 430 pp. plus index, $140.

This book is the product of an international symposium held in Iowa City in November 1987, as a result of a bilateral scientific agreement between the USA and the former USSR. Over 60 authors from academic institutions, industry and government agencies, both research and regulatory, are represented.

A substantial book, it has many equations and mathematical treatments of the various transformation processes undergone by chemicals in the environment. The introductory chapters emphasize the magnitude of the effect civilization, with its chemical pollutants and pesticides, has had on the environment. Pesticides and other chemicals may be changed via photolysis, oxidation, hydrolysis, volatilization, absorption, desorption and bioaccumulation. Several chapters consider the problem of the Great Lakes and the major pollutants, such as dioxins, PCBs, hexachlorobenzene, polycyclic aromatic hydrocarbons and heavy metals found in the lakes, and give equations and data for mass balance calculations.

Even fog acts as a medium aiding in the dissipation of pesticides into the environment. Transformation of xenobiotics is often mediated by free radicals in natural waters and sunlight-induced oxidation and reduction reactions. Several chapters deal with the transformation of halogenated aliphatics in natural systems, the biorestoration of sites contaminated by such compounds, and the potential for use of this technique in treating waste sites. Other chapters discuss computer systems for modeling pesticide runoff and the transformation processes, with extensive mathematical treatment of all the steps. The final chapter delves into the future of pesticide management and strategies.

Overall, this appears to be a useful and essential book for anyone involved or interested in pesticide management.

ELIZABETH K. WEISBURGER

Sulfuric Acid and Hydrochloric Acid, by Emergency Film Group, Plymouth, MA, Hazchem Series No. 1, Video Tape, 26 min, $395.00

Designed by a firm whose business is emergency response training, this video tape describes, for these two acids (according to the descriptive material accompanying the tape):

- How to identify corrosive acids
- Hazards
- Where they are found
- Reactivity problems
- Why water may be dangerous
- Proper protective clothing
- Stemming the flow of product
- Neutralization operations
- Emergency medical treatment
- Decontamination
- Environmental concerns

The film begins with a view of several types of emergencies and the need for safe, effective response — creating, as I note, "the need to know" or "the desire to learn". Clearly, these chemicals are important products of the chemical industry with 1991 U.S. production levels being:

H_2SO_4: 89 billion pounds
HCl: 5 billion pounds

Next the film graphically illustrates the destructive properties of sulfuric acid by showing its effect on chicken skin — the effects are obvious, the skin is destroyed. Then its uses are described — and they are many. Consequently, it is transported by all modes — truck, barge and rail.

Hydrochloric acid is then described. Its major differences from sulfuric acid are that it is volatile and it attacks all metals except precious metals. It, too, has numerous uses.

Both acids are toxic; both acids can be fatal. Using the NFPA guide, one finds the following ratings:

	H_2SO_4	HCl
Health	3	3
Flammability	0	0
Reactivity	2	0
Special	—	—

HCl is stable, but in contact with metals it can form an explosive hydrogen atmosphere. H_2SO_4 can generate heat in contact with many chemicals — sodium hydroxide, for example, but even water contact generates heat. Both the liquid and vapor of these acids are corrosive. Severe skin burns can result from exposure.

Shipping information, including a description of the containers, is given as DOT numbers (all are corrosives) as follows:

Type of acid	*DOT shipping number*
Sulfuric acid	1830
Spent sulfuric acid	1832
Battery acid	2796
Hydrochloric acid	1789

Proper storage, marking, protection from water, oxidation and other reactive chemicals are described. Diking and leak detection are shown, and proper personal protective clothing for working with these chemicals is also described. Illustrated next are the proper procedures for loading/loading.

But accidents may still occur, even though all proper precautions are taken. The problem is illustrated graphically by pictures from a spill/gas evolution resulting from reacting mixtures of waste acids in California. Evacuation, response and damage are shown.

The response procedures for a major spill are then shown:

- Evacuation
- Identification
- Control – the need for acid resistant clothing (Level A protection)
- Decontamination
- Search and rescue
- Discharge control
- Diking
- Vapor control
- Adsorption (fly ash, for example)
- Disposal of adsorbent
- Neutralization: soda acid, soda bicarbonate

Neither material burns, but they could contaminate firewater runoff. Removal of acid containers from fire exposure is best. Small fires can be controlled with CO_2, but if water is required (for a large fire) it should be applied from a distance.

Decontamination after the incident is described for protective clothing. (After exposure to acids, leather is useless, the video notes.) Victim symptoms and treatment are shown. You are advised to wash quickly and thoroughly. Oxygen may be used.

Next comes monitoring methods — by vapor tube, pH meter and pH paper. Waste disposal, with its legal reporting requirements is noted.

My reaction to the video is very favorable. All the necessary information is there and it is well described. This film is well worth using in training.

GARY. F. BENNETT

Handbook of Pollution Control Processes, by R. Noyes, Noyes Data Corporation, Park Ridge, NJ, 1992, 758 pp., $127.00.

According to the preface, "this handbook presents a thorough overview of state-of-the-art technology for pollution control processes". It indeed does that, covering virtually all treatment control technologies for air, water and solid, and hazardous waste, as well as the cleanup procedure for hazardous waste sites.

Because the topic areas are so broad, the treatment of each subject was terribly brief, so brief, I might have titled the book "Encyclopedia of Pollution Control Processes", to indicate the limited amount of material on each topic. Another limitation was the very short bibliography found at the end of each chapter. This area could have been usefully expanded by an order of magnitude.

In common with most of this publisher's books, there is a comprehensive table of contents. In addition, the author has added (much to my liking) an index.

In reviewing the book, I checked several sections of possible interest to me and in two found material that contained useful and new (for me) information. In total, my assessment of the book was very high.

Let me end with a list of the chapter titles:

1. Regulatory overview
2. Inorganic air emissions
3. Volatile organic compound emissions
4. Municipal solid waste incineration
5. Hazardous waste incineration
6. Indoor air quality control
7. Dust collection
8. Industrial liquid waste streams
9. Metal and cyanide bearing waste streams
10. Radioactive waste management
11. Medical waste handling and disposal
12. Hazardous chemical spill cleanup
13. Remediation of hazardous waste sites
14. Hazardous waste landfills
15. *In situ* treatment of hazardous waste sites
16. Groundwater remediation
17. Drinking water treatment
18. Publicly owned treatment works
19. Municipal solid waste landfills
20. Barriers to new technologies
21. Costs

GARY F. BENNETT

Energy Policy in the Greenhouse, by F. Krause, W. Bach and J. Koomey, A Report of the International Project for sustainable Energy Paths (IPSEP), Wiley, Interscience. New York, NY, 1992, ISBN-0-471-55663-7 (pbk), 328 pp. $29.95.

Recent events, including the collapse of world oil prices, the acid rain damage, Chernobyl and other disasters, have increased interest in the global

warming and greenhouse effects first largely ignored, but now becoming serious questions demanding constructive energy policies on an international basis. It begins with a definition and explanation for "greenhouse effect"; this is the trapping of infrared radiation by several gases and vapors, including naturally occurring water vapor, CO_2, clouds, ozone, methane and other gases which contribute 90% to the effect, and several trace gases, including nitrous oxide and the chlorofluorocarbons, CO, NO_x and SO_2, along with aerosol emissions, plus several gases whose effect is less well known, that contribute the remaining 10%. At a global average surface temperature of 288 K or 15 °C, the longwave outgoing radiation from the surface of the earth is 390 W/m^2 compared to 236 W/m^2 from the top layer of the atmosphere. This reduction in the longwave emission is a measure of the greenhouse effect.

The degree of climatic change the world is likely to experience depends on future atmospheric greenhouse gas concentrations, and the climate sensitivity assumed in mathematical models used for calculating warming. Even a 1–1.5 °C global average warming would represent a climate not experienced since the Holocene period at the beginning of which water would evaporate more giving an atmosphere of higher humidity and that is wetter overall.

Global warming would have serious effects on agricultural production, due to the delicate balance of temperatures, soil conditions and rainfall patterns. Weeds and plant pests also are encouraged by warmer temperatures, especially in developing countries. Global warming would also have an effect on the ability of forests and species to thrive and reproduce. Coastal settlements of several degrees could within the next 50 to 100 years be threatened by a sea level rise of 0.5 to 1.5 meters. Coastal settlements, in which half of humanity lives, would be threatened. In the USA alone, an estimated 12 million people would become homeless, and salinity would move upstream. Freshwater supplies would be threatened due to decreased stream flows and increased pressure on groundwater supplies. Electricity consumption would increase.

It is recognized that past greenhouse emissions make their full impact felt only with significant delay, and that continually growing emissions cannot be eliminated instantaneously, due to the inertia of social and economic systems. Serious attempts to estimate the effect both past and present emissions will have on the climate in, say, 50 to 100 years, are presented. Once concentration ceilings are suggested, the issue becomes what policy fields should be explored in order to implement the suggestions on a global basis, by way of emission reduction targets and enforcement. Obviously a global compact on climate stabilization and sustainable development would be essential.

This volume contains a most complete group of references, tables and graphs which permit the reader to understand the seriousness and timeliness of the subject. It should certainly be required reading for anyone who is concerned about the fate of our world, and is highly recommended.

HOWARD H. FAWCETT

Regulated Chemicals Directory, compiled by ChemADVISOR, published by Chapman and Hall, 29 West 35th St., New York, NY 10001-2291, 1992, ISBN 0-412-03481-6, 1409 pp., looseleaf in binder, revised on a quarterly basis, $375 (includes three quarterly updates). Also available in electronic form.

This directory is equivalent to the Beilstein reference, in that it contains essential references with cross references to 8000 chemicals found in many separate regulatory listings. It appears at a time when many producers, distributors and academic institutions are checking on the completeness and validity of Material Safety Data Sheets. The volume begins with CAS Registry Numbers as the primary means of storing and sorting information. It recognizes the need for general categories in the data base, including hazardous waste streams and isomers or other crystalline forms. Cross-reference indexes of chemical names and synonyms follow. It is noted that a substance with a unique CAS number may be regulated under several chemical names by different agencies. The major section of the directory is the Regulatory Summary Section, with the summaries giving the essential data under the most frequently used regulatory synonym. All the Federal and International lists are summarized for the particular chemical, as are state laws where appropriate.

This directory should be available in every industrial office involved with regulatory affairs, in the library of every academic school where chemistry is taught, and in the health, safety and environmental management of companies who use or produce chemicals. It is truly a major step in the attempts to remove doubts as to whether a material is or is not regulated, and by whom, and when. We recommend this directory highly.

HOWARD H. FAWCETT

Global Warning – Global Warming, by M.A. Benarde, Wiley-Interscience, New York, NY, 1992, ISBN 0-471-51323-7, 317 pp., $29.95

This volume furnishes data on both sides of the current global warming issue, reviewing both the political and scientific aspects. Climate change is the rule, not the exception, for the earth's tilt or inclination, the eccentricity of its orbit around the sun, and the precession due to its wobble have periodicities of 41,000, 100,000 and 23,000 years, respectively. Thus the earth's climate has shifted from glacial to interglacial periods at least 10 times during the past one million years.

The presence of life on earth is linked to the atmosphere which allows solar radiation to warm the planet but prevents reflection of all radiation back into space, a concept referred to as a "greenhouse effect" in 1827 by J.B. Fourier. What is worrisome is the marked increase in levels of carbon dioxide, nitrogen

oxide and methane, while the levels of ozone, especially over Antarctica, are decreasing, presumably due to the action of chlorofluorocarbons.

However, besides the increases due to human activities, there are natural factors which influence climate, from volcanoes to termites (termites release methane). Models for climate change are discussed thoroughly, but the author concludes "perhaps at this time forecasting ought to be looked upon as an exercise for gaining experience rather than as a tool for decision making". There is an extensive chapter on the potential dislocations which would occur if climate changed and the sea rose somewhat, as well as a chapter on energy efficiency which illustrates how the use of fossil fuel could be lessened, thus delaying to some extent the problem of global warming. The author concludes that people can do something about global warning, but it is time to act and not wait until it is too late.

ELIZABETH K. WEISBURGER

Hormones and Vitamins in Cancer Treatment, by A. Lupulescu, CRC Press, Boca Raton, FL, 1990, ISBN 0-8493-5973-2, 287 pp., $159.95.

This volume will appeal to specialists in cancer treatment or to those doing research on prevention of cancer by dietary means. The topics covered include: rationale for hormone and vitamin therapy; hormones and their use in therapy; hormone antagonists and agonists; hormone-like substances such as growth factors, interferons, interleukins and prostaglandins in clinical applications; vitamin therapy; chemoprevention of cancer by hormones and vitamins; the advantages and disadvantages of hormonal and vitamin therapy; while the concluding chapter discusses the interaction among diet, hormones, vitamins and cancer. All of the chapters are almost exhaustively referenced. For anyone contemplating research in any one of the areas covered, this book would be an excellent resource.

ELIZABETH K. WEISBURGER

Risk Factors for Cancer in the Workplace, by J. Siemiatycki (Ed.), CRC Press, Boca Raton, FL, 1991, ISBN 0-8493-5-18-2, 325 pp., $99.50

This volume results from interviews with 3730 male cancer patients, between 35 and 70 years of age, resident in the Montreal metropolitan area. Diagnoses were confirmed histologically. The patients were then evaluated for probable exposure to 183 substances or groups of substances and further stratified into 98 occupational and 77 industry groups, subdivided according to 11 cancer sites or types of tumors. With all these subdivisions, the actual number of cases exposed to any one substance often became so small that one questions the significance of the purported association. Furthermore, actual exposure levels

were not obtained; based on the interviews, patients were grouped into those with "substantial exposure" and "any exposure". Many tables are given with the calculated odds ratios and confidence intervals for the associations, using $p = 0.10$ for the level of significance. In the final analysis, often the numbers of cases in a specific category were rather small, and most epidemiologists use $p = 0.01$ or less as a measure of real significance. Thus this book may provide some leads and serve as a reference source, but its actual value in identifying workplace hazards is somewhat limited, apart from those which are already known.

ELIZABETH K. WEISBURGER

Journal of Hazardous Materials, 33 (1993) 155–157
Elsevier Science Publishers B.V., Amsterdam

Announcements

The International Symposium on Hazardous Waste Management in Economically Developing Countries, June 24–26, 1993, Istanbul, Turkey

Scope

The Turkish National Committee on Solid Wastes being aware that solid waste in general but in particular hazardous waste management has become an important problem for the economically developing countries, has decided to organize jointly with the International Solid Wastes and Public Cleansing Association (ISWA) this Symposium.

Themes

The themes to be covered in this Symposium are:

- Hazardous Waste Generated in Developing Countries
- Simple Technology for Hazardous Waste Management and Disposal
- Collection and Transportation of Hazardous Waste
- Sanitary Landfilling and Hazardous Wastes
- Advancements in Appropriate Incineration Technology for Developing Countries
- Advantages and Disadvantages of use of Cement Kilns for the Disposal of Hazardous Wastes
- Limits in the use of Cementation in the Disposal of Hazardous Wastes
- Management of Special Wastes (Batteries, Hospital Wastes, Treatment Plant Sludges etc.)
- Advantages and Disadvantages of Co-disposal
- Environmental Ethics, Economy and Legislation Related to Hazardous Wastes
- Health Problems Caused by the Improper Management of Hazardous Wastes
- Hazardous Waste Minimization Methodology
- Case Studies

Contact

All correspondence should be addressed to: The Turkish National Committee on Solid Wastes Attn: Prof. Dr. Kriton Curi
Boğaziçi University
80815 Bebek, Istanbul–Turkey
Telephone: 90-1-263 15 00
90-1-263 15 40-1439
Telefax: 90-1-265 84 88
90-1-265 84 88 or 90-1-257 35 68
Electronic Mail CURI @TR BOUN bitnet

Symposium on Hazardous Waste Treatment, August 29–September 3, 1993, Prague, Czechoslovakia

Aims and scope

The Symposium on Hazardous Waste Treatment is a special event of CHISA '93 the 11th International Congress of Chemical Engineering, Chemical Equipment Design and Automation organized by the Czech Chamber of the Czechoslovak Society of Chemical Engineering.

The aim of the symposium is to inform scientific and research workers dealing with the problems of high technology for the environment, managers and firms engaged in purchasing and transferring technologies for the environment, leaders and experts of the state department that decides on state ecological policy, and also experts in the field responsible for the problems of local environments affected by industrial production of modern *high technologies for the liquidation of toxic and hazardous waste* from the chemical, biochemical, foodstuffs and other branches of the processing industry.

In view of the decisive and irreplaceable contribution made by chemical engineering to the creation of new high technologies for the liquidation of toxic components, this Symposium is being held as a special event of the CHISA '93. It is proposed to present brief information in the form of both lectures and posters. There should also be a mini-exhibition of the technologies offered.

The Symposium will be aimed especially at:

- Theoretical principles of membrane (filtration) processes of the selective separation of toxic components from liquid and gas phases

- Sorption selective separation of toxic and hazardous components from liquid and gas phases
- Principles of processes of thermal decomposition of toxic components
- Processes of the extraction of toxic components from liquid and solid phases including industrial and sewage sludge
- Bioreactors for environmental biotechnology
- Application of chemical-engineering procedures in the detoxification of soils *in situ*.
- Presentation of successful existing high technologies
- Case histories
- Exchange of information in the sphere of the supply and demand of environmental technologies.

Call for papers

Detailed instructions and submission dates for abstracts, full papers and posters can be obtained from:

F. Kaštánek
Scientific Secretary CHISA '93
P.O. Box 857
C.S.-11121 Praha 1
Czechoslovakia

Fax: 422-342-073
Telex: 121339 ucav
E-mail: CHISA@CSEARN

SUBMISSION OF PAPERS

Submission of a manuscript implies that it is not under consideration for publication elsewhere and further that, with the exception of review papers, original work not previously published is being presented.

Papers should be submitted to Dr. G.F. Bennett, Department of Chemical Engineering, University of Toledo, 2801 W. Bancroft Street, Toledo, OH 43606, U.S.A. or Dr. R.E. Britter, Department of Engineering, University of Cambridge, Cambridge CB2 1PZ, Great Britain. Authors in the Far East should submit papers to Dr. T. Yoshida, Chemical Engineering Laboratory, Department of Mechanical Engineering, Faculty of Engineering, Hosei University, 7-2 Kajino-cho 3-chome, Koganei-shi, Tokyo 184, Japan.

MANUSCRIPT PREPARATION

Three copies of the manuscript should be submitted in double-spaced typing on pages of uniform size with a wide margin on the left. The top copy should bear the name and the full postal address of the person to whom the proofs are to be sent. A summary of 100–200 words is required.

References should be numbered consecutively throughout the text and collected together in a reference list at the end of the paper. Journal titles should be abbreviated. The abbreviated title should be followed by the volume number, year (in parentheses), and page number.

ILLUSTRATIONS

Line drawings should be in a form suitable for reproduction, drawn in Indian ink on drawing paper. They should preferably all require the same degree of reduction, and should be submitted on paper of the same size as, or smaller than, the main text, to prevent damage in transit. Photographs should be submitted as clear black-and-white prints on glossy paper. Each illustration must be clearly numbered. Colour illustrations can be reproduced at the author's expense.

Legends to the illustrations must be submitted in a separate list.

All tables and illustrations should be numbered consecutively and separately throughout the paper.

LANGUAGE

The principal language of the journal is English, but papers in French and German will be published.

PROOFS

Authors will receive page proofs which they are requested to correct and return as soon as possible. No new material may be inserted in the text at the time of proofreading.

REPRINTS

A total of 50 reprints of each paper will be supplied free of charge to the principal author. Additional copies can be ordered at prices shown on the reprint order form which accompanies the proofs.

A pamphlet containing detailed instructions on the preparation of manuscripts for JOURNAL OF HAZARDOUS MATERIALS may be obtained from the publishers.

0304-3894/93/$06.00

PRINTED IN THE NETHERLANDS

VOL. 33, NO. 1 JANUARY 1993

JOURNAL OF HAZARDOUS MATERIALS

CONTENTS

SUBSCRIPTION INFORMATION

1993 Subscription price: Dfl. 1400.00 plus Dfl. 132.00 (p.p.h.) = Dfl. 1532.00 (approx. US $850.00). This covers volumes 32–35. The Dutch guilder price is definitive. The U.S. dollar price is subject to exchange-rate fluctuations and is given only as a guide. Subscription orders can be entered only by calendar year (Jan.–Dec.) and should be sent to: Elsevier Science Publishers B.V., Journals Department, P.O. Box 211, 1000 AE Amsterdam, The Netherlands, Tel. (020) 5803642, Telex 18582 ESPA NL, Fax (020) 5803598, or to your usual subscription agent. Claims for missing issues will be honoured, free of charge, within six months after publication date of the issue. All back volumes are available. Our p.p.h. (postage, package and handling) charge includes surface delivery of all issues, except to the following countries where air delivery via S.A.L. (Surface Air Lifted) mail is ensured: Argentina, Austral a, Brazil, Canada, Hong Kong, India, Israel, Japan, Malaysia, Mexico, New Zealand, Pakistan, P.R. China, Singapore, South Africa, South Korea, Taiwan, Thailand, and the U.S.A. For Japan, air delivery by S.A.L. requires 25% additional charge; for all other countries airmail and S.A.L. charges are available upon request. Customers in the U.S.A. and Canada wishing information on this and other Elsevier journals, please contact Journal Information Center, Elsevier Science Publishing Co., Inc., 655 Avenue of the Americas, New York, NY 10010, Tel. (212) 633-3750, Fax (212) 633-3764.

0304-3894(199301)33:1;1-U